Calibration of Large Rogowski coils

by

Stephanus Lucas Combrink

Thesis presented in partial fulfilment of the requirements for the degree Master of Engineering (Research) in the Faculty of Engineering at Stellenbosch University

Supervisor: Dr. P.G Wiid

March 2016

Acknowledgements

I would like to thank and express gratitude towards the following people:

My saviour, Jesus Christ. Love, strength and joy, I receive it in abundance.

TESP and the SA SKA Research Chair in Engineering Electromagnetics for funding the project.

Dr. Wiid. Academic and life insight passed on through weekly meetings, trips to the SKA and some jokes over Gelato.

My family for support. I know it is not easy listening to things you don't understand.

My friends that also did their masters and other projects. We did this.

A truly skilled man, Mr. Wessel Croukamp. Thank you for construction help even through the busiest of times

Anneke Bester for her insight and help with measurements.

Room E212 occupants. Past and present collogues, skripsie students. Hardie Pienaar, Antheun Botha, Nardus Mathyssen, Stanly Kuja, Joely Andriambeloson, Temwani Phiri, Sam Dodson, Mouritz de Beer, Joshua Blom. We laughed together, we laughed some more, you made the journey great.

Braam Otto and Paul van der Merwe for help concerning measurement campaigns. SKA trips would have been very different if you were not there.

Declaration

By submitting this thesis electronically, I declare that the entirety of the work contained therein is my own, original work, that I am the sole author thereof (save to the extent explicitly otherwise stated), that reproduction and publication thereof by Stellenbosch University will not infringe any third party rights and that I have not previously in its entirety or in part submitted it for obtaining any qualification

Date: March 2016

Abstract

Calibration of Large Rogowski coils

S.L Combrink

Department of Electrical and Electronic Engineering,
University of Stellenbosch,
Private Bag X1, Matieland 7602, South Africa.

Thesis: MIng(EE)

February 2016

The Square Kilometre Array aims to be the world's largest radio telescope. South Africa will host the mid to high frequency division of the SKA and the core site will be populated with 64 offset Gregorian radio telescopes for the first phase. To achieve a resolution 50 times higher than the Hubble Space Telescope, radio frequency interference (RFI) must be kept as low as possible. Past and present studies are committed to keep the introduced and already present RFI as low as possible.

Our study stems from a previous study on RFI originating from lightning (induced) currents. The study examined KAT-7, the precursor to MeerKAT, extensively and from it valuable recommendations were made. This study also gave rise to the creation of a Rogowski coil (RC) for current measurements. The RC is physically large to be able to fit around antenna struts. However, calibration was not considered for that study. Since current measurements on antenna struts are still of interest, it gives rise to our investigation into the calibration of the large RC for accurate measurements.

The study begins by analysing a frequency domain (FD) method commonly used by current probe manufacturers. Good agreement between a theoretical model, simulation and measurement is obtained, but without proper de-embedding, the method is only accurate at frequencies up to 100 MHz. To extend the frequency range, a time domain (TD) technique is applied where the signals are analysed in the TD and unwanted responses are gated out, providing accurate calibration to much higher frequency. Both approaches are verified with calibration data and measurements of two commercial current probes.

To improve RC calibration accuracy, an attempt is made to reduce the main mismatch reflection between the measurement device and calibration fixture. A high permittivity dielectric is investigated which, unfortunately, produced inconclusive results. Using a larger diameter conductor with a matching profile resulted in a decrease in reflection magnitude as expected. However, the matching profile introduced sub-reflections.

To avoid uncertainty due to sub-reflections, the large RC was calibrated without the matching profile. To achieve a good calibration over all frequencies, a hybridised method is applied which uses the results from the frequency ranges where each method provides the most accurate calibration results, low frequency from the FD method and the higher frequency from the TD method

Uittreksel

Kalibrasie van Groot Rogowski coils

("Calibration of Large Rogowski coils")

S.L Combrink

Departement Elektriese en Elektroniese Ingenieurswese,
Universiteit van Stellenbosch,
Privaatsak X1, Matieland 7602, Suid Afrika.

Tesis: MEng (EE)

Februarie 2016

Die Vierkante-Kilometer Reeks (VKR) gaan die wêreld se grootse radio teleskoop wees, waarvan Suid-Afrika die middel tot hoë frekwensie afdeling van die VKR huisves. Vir die eerste fase sal die kern area bevolk word met 64 Gregorian-afset radio teleskope. Om 'n resolusie van 50 keer hoër as die Hubble ruimte teleskoop te behaal moet die radio frekwensie steurings (RFS) so laag as moontlik behou word. Dit word verseker deur vorige en voortgaande studies. 'n Spesifieke vorige studie het gekyk na RFS van weerlig (geïnduseerde) strome op KAT-7, die voorloper tot MeerKAT. Hieruit het waardevolle voorstelle gekom asook 'n Rogowski winding (RW) stroom meetinstrument. Die RW het 'n groot gemene omtrek sodat dit om groot antenna stutte kan pas. Die RW is egter nie gekalibreer nie, wat gedien het as motiveerder vir ons projek.

Die studie begin met die analise van die frekwensiedomein (FD) metode, alom gebruik deur stroom meetinstrument vervaardigers. Goeie resultate is verkry wat korreleer oor teorie, simulasie en meting. Die metode is onakkuraat bo 100 MHz omdat dit die refleksies en resonansies nie verwyder van die gemete response nie. 'n Tyddomein (TD) analise tegniek word toegepas waar die ongewenste response verwyder word. Beide metodes word geverifieer met kommersiële meetinstrumente.

Om RW kalibrasie te verbeter word impedansie aanpassing van die kalibrasie bakkie ondersoek. 'n Dielektriese medium met 'n hoë permittiwiteit word ondersoek asook 'n aanpassing profiel vir 'n vergrote diameter geleier. Die hoë permittiwiteit ondersoek het onbevredigende resultate gelewer. Die gebruik van 'n vergrote diameter geleier het gelei tot 'n verkleining van die eerste refleksie, maar as gevolg van die profiel wat gebruik is, verskyn daar sub-refleksies.

Om onsekerheid te vermy was die RW gekalibreer sonder die aanpassings profiel. Om 'n goeie kalibrasie oor die hele frekwensie band te verseker word 'n hibriede metode toegepas. In hierdie metode word die FD en TD metodes se resultate gebruik waaar dit die mees akuraatste is; laer frekwensies van die FD metode en die hoër frekwensies van die TD metode wat gekombineer word vir 'n algehele kalibrasie.

Contents

List of Figures

List of Tables

Nomenclature

Abbreviations

ATR	Air Termination Rod
CISPR	International Special Committee on Radio Interference
CM	Common Mode
CP	Current Probe
dB	Decibel
EMC	Electromagnetic Compatibility
EMRIN	EMC and Metrology Research and Innovation
FD	Frequency Domain
FFT	Fast Fourier Transform
fig	Figure
GHz	GigaHertz
KAT	Karoo Array Telescope
kHz	KiloHertz
MHz	MegaHertz
PG	Pulse Generator
RC	Rogowski Coil
RFI	Radio Frequency Interference
RFS	Radio Frekwensie Steurings
RW	Rogowski Winding
SANS	South African National Standards
SKA	Square Kilometre Array
S-parameters	Scattering parameters
TD	Time Domain
VKR	Vierkante-Kilometer Reeks
VNA	Vector Network Analyser
Z_t	Transfer Impedance

Constants

$c =$	$299792458\,\mathrm{m/s}$
$\epsilon_o =$	$8.854\text{x}10^{-12}\,\mathrm{F/m}$
$\mu_o =$	$4\pi\text{x}10^{-7}\,\mathrm{H/m}$

Variables

ϵ_r	Relative Permittivity	[ ]
μ_r	Relative Permeability	[ ]
N	Number of Windings	[ ]
d	Wire thickness	[m]
D	Height above ground plane	[m]
a	RC inner radius	[mm]
b	RC outer radius	[mm]
R	RC mean radius	[mm]
h	RC winding width	[mm]

Chapter 1

Introduction

The Square Kilometre Array (SKA) is an international endeavour to build the world's largest radio telescope. It will finally have the ability to observe the universe with a resolution 50 times higher than the Hubble Space Telescope. This feat will be achieved by populating the SKA core site near Carnarvon in the Northern Cape, South Africa with several hundred telescopes, with the first phase initiated with MeerKAT. This phase was granted after the KAT-7 project (fig. 1.1) won the bid for South Africa to host the mid to high-frequency dishes [1]. MeerKAT will consist of 64 offset Gregorian type antenna dishes.

Figure 1.1: KAT-7, the precursor for MeerKAT shown in the background. The MeerKAT main reflector dish (centre front) is shown in transit during the setup stage [1].

1.1 Background

Currently, the sensitivity of the radio telescopes is limited by the radio quietness of the area in which they are located. It is of the essence to keep the area as radio quiet as possible and also to mitigate the effects of unavoidable Radio Frequency Interference (RFI). Various studies involving RFI and Electromagnetic Compatibility (EMC) have

been done for the bidding phase (KAT-7), and some are continued for the implementation of MeerKAT. While the majority of studies are done on man-made RFI (electrical fence sparking, car ignition systems, air-conditioning noise etc.), naturally occurring RFI must be accounted for as well. Lightning is a naturally occurring RFI source. Fortunately it is not always present, which allows for normal operation of scheduled science observations to be done. However, in the event of a (direct) strike, induced currents may couple into sensitive systems and contaminate measurements, or worse, damage expensive equipment.

Figure 1.2: Lightning over SKA core site. Credit: P.G. Wiid

1.2 Problem statement

A study with a focus on RFI stemming from lightning (induced) currents, examined the lightning protection deployed on the KAT-7 radio telescopes [2]. Lightning currents can achieve magnitudes in the excess of 130 kA [3], which warrants the presence of good lightning protection. In the mentioned study, the need for current measurements was created. While easily measured with the use of commercial current probes (CP), large antenna struts were of particular interest and funding for large current probes was unavailable. This gave rise to the in-house fabrication of a large Rogowski coil (RC) that could fit around large antenna struts. However, since the mentioned study's scope was already established and progressed too far, RC calibration was not included.

Many studies have been done on RCs and its calibration, but little literature exists for large RC calibration for the use in an EMC perspective. This then gave rise to pursuing calibration of large RCs.

1.3 Methodology

Most if not all methodologies consist of having a uniquely described system in which all or most of the variables are known. The variables that can not be accounted for will result in an error. The error can be given as a tolerance factor as is the case with many commercial

CPs. Some methods rely on calibration against a probe with known characteristics. This approach is adequate for well-defined signals which are repetitive in nature.

Figure 1.3: Implementation of an RC used on-site at M63

1.4 Thesis layout

In Chapter 2 a literature review concerning lightning studies and RCs is done. Previous work on lightning is examined along with the national guidelines on lightning strike waveform and spectra. For the RC, typical theoretical models and calibration methods are investigated. Chapter 3 explores the RC's characteristics from a theoretical and computational perspective. The frequency domain (FD) calibration method is applied first, but it is found inadequate at higher frequencies. For the higher frequencies a time domain (TD) technique is applied.

Due to the physical size of the RC (25 cm in diameter), the calibration fixture needs to be enlarged, which increases transmission line mismatches. Two approaches are investigated to counter the increased mismatch; the use of high permittivity dielectric and alterations to the fixture geometries. Computational electro-magnetics is used to optimise a matching transition for a new conductor.

The results and discussions are included in Chapter 4. With the FD and TD approaches verified, they are used to calibrate the RC. To test the calibration of the RC, a bandwidth test is done. The results along with potential error in the applied approaches are discussed. As implementation, the RC is used on a measurement campaign. The results differ substantially, but can be explained by environmental influences on the RC.

The study is concluded in chapter 5. Conclusions about the RC, calibration approaches and practical measurements are made. Recommendations are given for improving the applied approaches and possible future work is discussed.

Chapter 2

Literature review

For the literature review, lightning and RCs are investigated. Previous work on lightning is briefly examined before looking at the typical waveforms and spectra of lightning strikes. Since the focus shifted towards the RC, it will receive more attention. Theoretical and computational models are examined, but are found to be generally application specific. The components that establish the working bandwidth of the RC are also investigated, with special attention given to the capacitance. Since accurate measurements are of the essence, calibration of RCs for different applications is also studied.

2.1 Lightning

The characteristics of lightning is a well-covered subject. Many studies have been done to characterise it and recommend safety measures for it. In our group for EMC and Metrology Research and Innovation (EMRIN), a comprehensive study was done on lightning protection for the KAT-7 radio telescope [2]. This study utilised standards to improve EMC and to provide suggestions on further improvements.

The International Electrotechnical Commission have set up these standards for the purposes of streamlining designs and ensuring a safe procedure is applied to projects. An adoption of these standards for South Africa is the SANS Protection against Lightning standards (62305-1 to 62305-4) [3]. These standards contain a broad description of lightning characteristics, minimum mitigation guidelines and risk management when designing structures and equipment prone to lightning strikes. Only the basic lightning description will be used since risk analysis was used in the design phase of the MeerKAT radio telescopes.

2.1.1 Previous work

Aiming to be the world's largest radio telescope, the SKA has to be a multi disciplinary endeavour, giving both professionals and academics the chance to play a vital role in its development and success. One such role was fulfilled in the study of lightning protection [2]. The KAT-7 radio telescope was analysed and suspect areas were scrutinized. A simplified computational model for FEKO [4] - a Method of Moments type code - was created from original designs and a scaled physical model was fabricated. Along with direct current injection, plane wave illumination was also used to simulate indirect strikes. Measurements and simulations compared well, from which conclusions and recommendations were formulated [5].

The simulations and scaled measurements were also compared to measurements taken on-site. During the planning and testing phase of KAT-7, tests consisted of signal injection onto the Experimental Demonstrator Model dish assembly at HartRAO. A signal generator was used to inject 10 MHz and 50 MHz signals. However, the generator was powered from the on-site 220V mains, giving rise to possible extra coupling loops. Measurements were taken with a battery operated hand-held spectrum analyser [2]. An opportunity was granted to do a similar measurement on KAT-7, shown in fig. 2.1. Of particular interest were currents flowing on large antenna struts. With restrictions imposed by the dimensions of a commercial CP (ETS 94111-1L with a 33 mm inner diameter), the measurements on the large struts could not be taken. For this reason an RC with a large mean radius of 12.5 cm was created which fits around an antenna strut with ease.

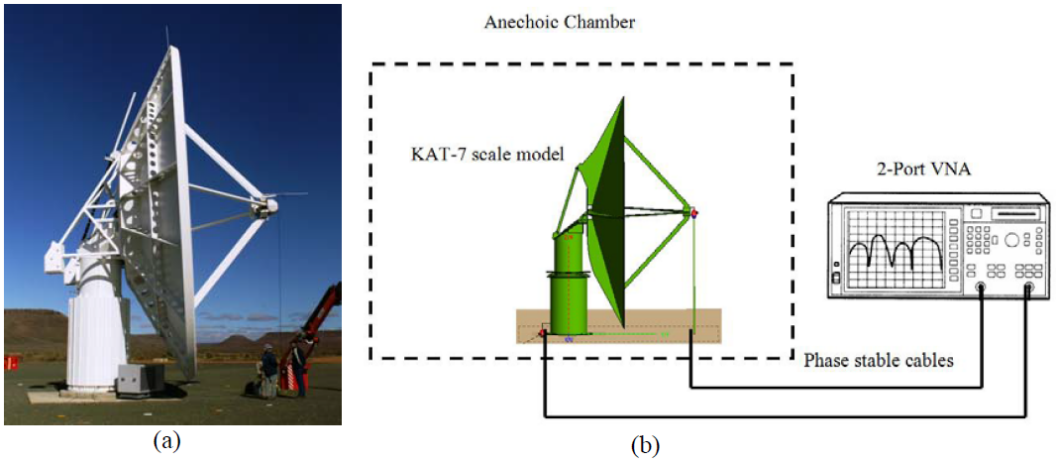

Figure 2.1: On-site measurement of current injection on KAT-7 (a) and representative schematic setup in simulation and scaled measurement (b) [6]. Plane wave illumination was included in the simulation to simulate indirect strikes.

For our first and second measurement campaign, the possibilities of small scale current injection were investigated. These campaigns did not provide opportunity for actual measurements since telescope construction took precedence. Nonetheless, the telescope was examined and possible setups discussed. Figure 2.2 shows the proposed setup. A pulse generator will be used to inject a signal onto the Air Termination Rod (ATR). A grounding point is needed to ensure a valid current return path. Since the isolation transformer uses the pedestal earth, it is proposed as the grounding point. The isolation transformer accepts a delta connection and outputs a wye connection. Should a lightning strike occur, the current will follow the lowest impedance path possible. This path might not be along the intended lightning down conductors, but rather through mechanical interconnects. For concern of damage from excessive heating due to large currents, the interconnects will be regarded as areas of interest where measurements will be made.

2.1.2 Pulse waveform and spectra

Lightning can be classified as quick events, which gives reason to model them as pulses. In the time domain (TD) a pulse waveform is governed by eq. 2.1.1 [3]. In this equation, T_1 and T_2 represent the rise and tail times, respectively. A peak current is represented by I and k is added as a correction factor. These parameters are shown in fig. 2.3. Through

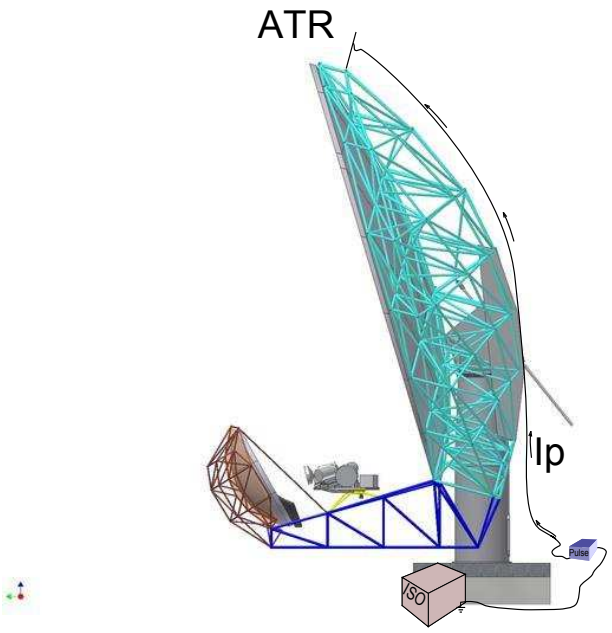

Figure 2.2: Schematic setup of first planned site visit [7]. The signal will be generated with a pulse generator and injected onto the air termination rod. The currents will distribute across the struts and lightning down conductors and flow towards the pedestal earth. The isolation transformer is connected directly to this earth and will provide the reference earth for injection and measurements.

these variables the waveform can be shaped until a desired bandwidth is achieved. While lightning strikes consists of several components, only the main strike will be considered.

$$i = \frac{I}{k} \times \frac{(\frac{t}{T_1})^{10}}{1 + (\frac{t}{T_1})^{10}} \times \exp(\frac{-t}{T_2}) \tag{2.1.1}$$

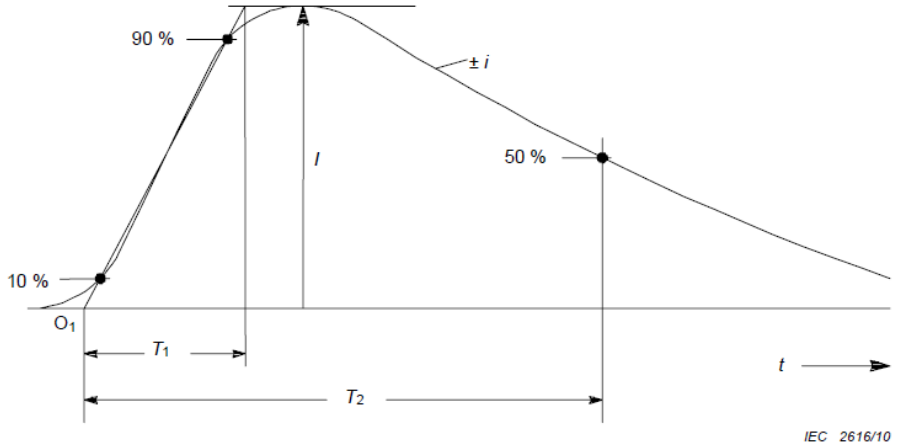

Figure 2.3: Double exponential waveform commonly used in lightning studies [3].

Displayed in fig. 2.4 are the guidelines for lightning spectra [3]. Most of the energy lies in the low kHz region, carried in the first positive stroke. High frequency energy is contained in the subsequent negative strokes, but for lightning protection only frequencies

up to 10 MHz are of concern. However, these figures are only guidelines from a protection perspective.

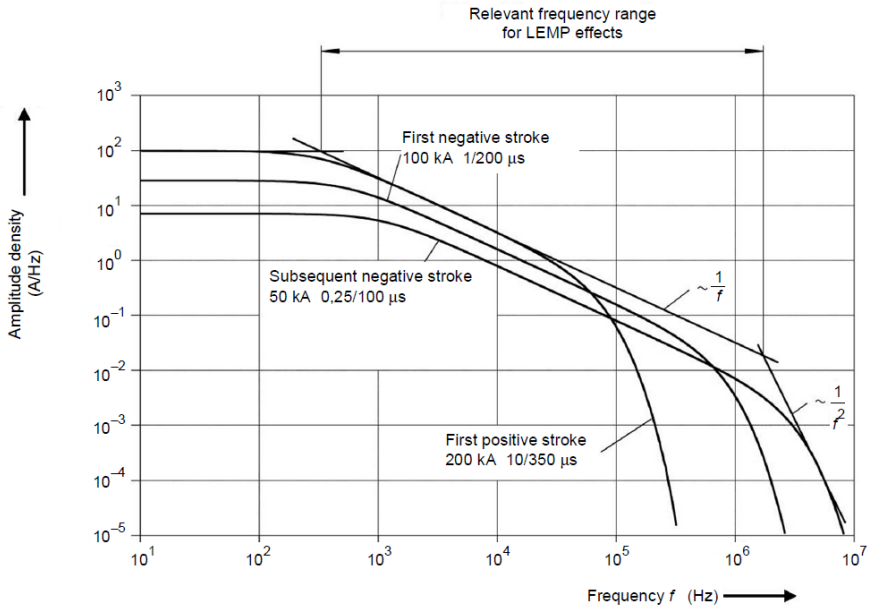

Figure 2.4: Lightning spectral content [3]. While the first positive stroke only has spectra of concern up to 300 kHz, our study will acknowledge a 50 MHz upper limit.

Multiple studies make use of current transducers with a bandwidth that covers the spectra in fig. 2.4. RCs with an approximate bandwidth of 1 kHz to 30 MHz are used in [8]. One study utilizes an impressively large (3 m) RC with 40 MHz bandwidth [9]. Use of transducers with adequate bandwidth is not always the case. One study uses RCs with bandwidths between 300 Hz and 1 MHz [10]. However, in [6] the cut-off for high frequency components in lightning (induced) currents is 50 MHz. Our study will utilise the 50 MHz upper limit for lightning studies and consider higher frequencies for complementary EMC investigations as well.

2.2 Rogowski Coils

The RC (fig. 2.5) is a common transducer in lightning studies [11]. This is partly due to the isolation characteristics it exhibits [12]. It also has the advantage of compensating for induced signals due to stray fields via its return winding [13], [14]. The RC outputs a voltage proportional to the derivative of the current being measured. In the working bandwidth of the RC, the magnitude of the output voltage is primarily determined by the mutual inductance between the current carrying wire and the RC. Equation 2.2.1 shows the relationship between the output voltage and measured current.

$$V_{out} = M\frac{dI}{dt} \tag{2.2.1}$$

Equation 2.2.1 is only valid for the working bandwidth of the RC. The bandwidth is determined by the RC's self-capacitance and self-inductance, each influenced by the materials used and the physical dimensions of the RC windings. Although variations can

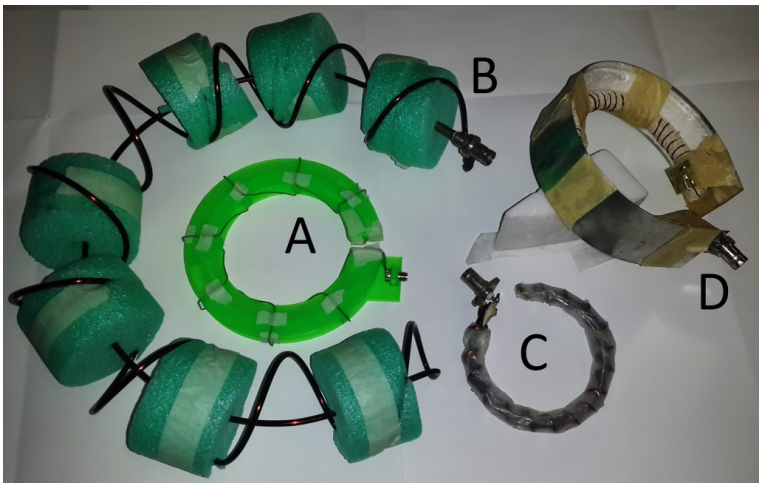

Figure 2.5: Some of the Rogowski Coils used in this project. A: a low profile RC, B: the large RC which was the main focus of this study, C: a smaller RC, D: an RC with an electrostatic shield and terminating resistance.

include a ferromagnetic core, most of the designs use an air core. Air cores allow for much higher currents to be measured since saturation is less of an issue. With typical lightning currents as high as 130 kA [3] the RC makes for a perfect current transducer for lightning current measurement.

2.2.1 Theoretical Model

Due to the low complexity, most sources consider the RC as a 2^{nd} order filter type circuit [14] [15] [16] [17] . Although their measurements correlate with the mathematical model, it is usually over a low bandwidth (less than 40 MHz). The model results in a transfer function or gain that describe the RC's behaviour [14] [16]. The transfer function has a differentiating and self-integrating region before the first resonance occurs. This correlates with the transfer impedance (Z_t) described by CISPR [18]. The Z_t is a frequency specific impedance that relates the output voltage to the measured current.

The 2^{nd} order circuit usually includes lumped element components for self-inductance, a resistor accounting for losses and a capacitance for either inter-winding, stray or other capacitances or a combination of them. Variations on this circuit include components for an integrator. A simple resistor-capacitor or active integrator can be used, though extra care should be taken with the active devices due to their own bandwidth (among other) limitations. Including an integrator allows for direct output of the current waveform induced in the RC. Figure 2.6 (taken from [16]) depicts a circuit with RC modelled components for self inductance, capacitance and resistance. Included in the circuit is an active integrator.

To achieve a model with higher accuracy over a higher bandwidth, [19] and [20] have used a transmission line analysis method to describe the RC. While their results compare well in terms of theory and actual measurements, the approach is application specific due to the well characterised constant capacitance introduced through the use of an electrostatic shield [19]. A similar objective (higher accuracy) was investigated in [21]. The approach involved modelling each pick-up loop of the RC as a circuit block with components for capacitance, resistance and inductance. The whole RC was then modelled as a cascaded system, starting with one circuit block. The number of blocks were increased

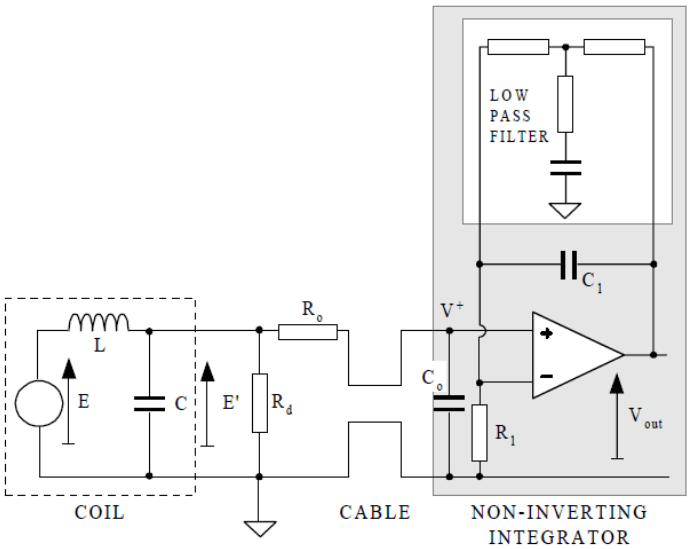

Figure 2.6: 2nd Order circuit modelling Rogowski Coil and integrator circuit [16].

until no change in Z_t was noticed. This happened after 4 iterations. The full cascaded system can also be viewed as a transmission line approach.

2.2.1.1 Inductance

The first component to evaluate is the inductance of the RC. Calculations for RC inductance (mutual and self) exist can be easily found in literature. However, some sources [15],[16] take the magnetic flux density $B(r)$ as uniform, resulting in the simple multiplication of the flux and area. Studying eq. 2.2.2 it is seen that $B(r)$ decreases radially. This is illustrated on the right of fig. 2.7 where radially decreasing flux is represented by thinning lines. This figure also displays the dimensions associated with the RC.

$$B(r) = \frac{\mu_o \mu_r N I}{2\pi r} \tag{2.2.2}$$

The assumption that the magnetic flux density is uniform can only be made as long as the radial distance ($b - a$ in fig. 2.7) of the area is small. This assumption also warrants the wavelength of the highest frequency to be adequately greater than the axial dimension (h, fig. 2.7). This will ensure negligible phase difference, i.e. a difference in $B(r)$ fields. The colour gradient along the current carrying conductor attempts to show the phase difference.

The equations for inductance rely on the physical dimensions of the RC and depending on whether a circular or square winding is used, equations 2.2.3 [19] and 2.2.4 [22] will be used, respectively.

$$M_{sqaure} = \frac{\mu_o \mu_r N h}{2\pi l_w} \ln(\frac{b}{a}) \tag{2.2.3}$$

$$M_{circ} = \frac{\mu_o \mu_r N}{2 l_w} (\sqrt{b} - \sqrt{a})^2 \tag{2.2.4}$$

Accounting for the change in radial flux, the only assumption now is that the frequency of the signal to be measured is low enough so that negligible phase difference occurs over the axial length (h, fig. 2.7) of the RC winding.

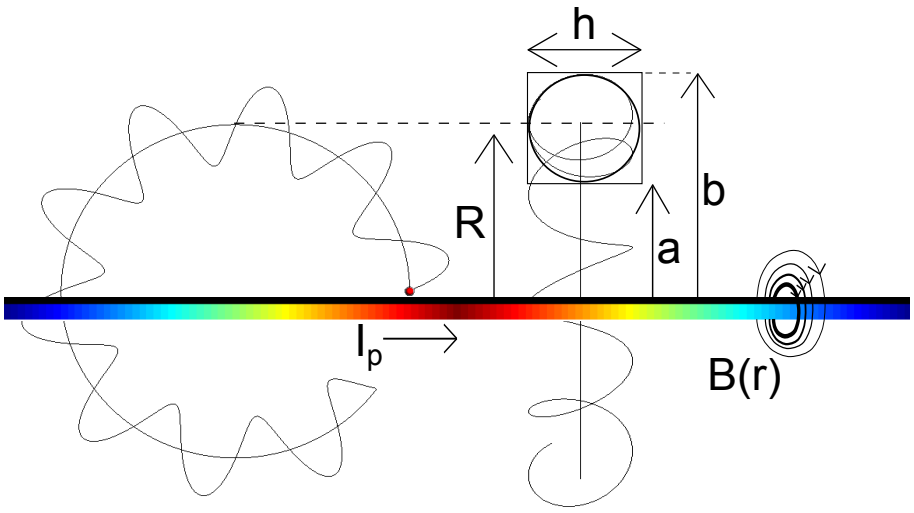

Figure 2.7: Dimensions associated with Rogowski Coils. R, a and b are all constants of the radial dimension r. The axial dimension h is only present when a rectangular winding is used.

2.2.1.2 Capacitance

For most RC models, the capacitive elements are described inadequately. This might be due to the difficult geometric descriptions for capacitances in RCs. Some sources acknowledge that there will be a capacitive element, but do not state where this capacitance originates from [20], [23]. Arguments can be made for the inclusion or exclusion of the certain capacitances but little literature exists supporting them. A more focused study [21] explores three capacitances that are always present in any given setup: the capacitance between the source conductor and windings C_{ws}, between the windings and return winding C_{wr} and the capacitance between the windings themselves C_{ww} (inter-winding capacitance). The capacitances are illustrated in fig. 2.8.

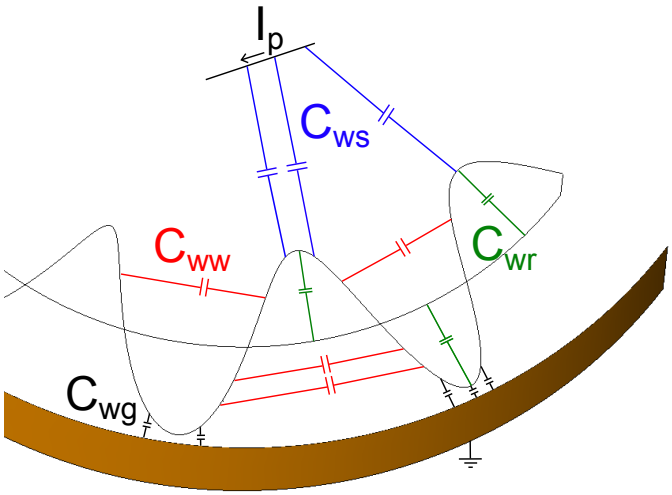

Figure 2.8: Capacitances associated with the RC. Winding to source (C_{ws}), inter-winding (C_{ww}), winding to return winding (C_{wr}), and winding to ground(C_{wg}). The curved ground plane resembles an electrostatic shield.

Another capacitance that may be present is the capacitance between the windings

and a ground plane C_{wg}. This could be introduced via an electrostatic shield as is the case for [19]. Their model include the capacitance to ground and produces very good results. This is due to the capacitance to ground being well defined. However, the use of an electrostatic shield causes diminishing bandwidth [24] which conflicts with one of the main goals for this study: finding a solution for current measurement with maximum bandwidth. For this reason, an electrostatic shield is not considered.

A capacitance that is very important and has been proven so in early measurements is the capacitance between the source conductor and windings of the RC. However, due to geometrically difficult definitions of these capacitances, analytical solutions do not exist. An attempt was made by [21] to establish a value for this capacitance through numerical methods. However, fluctuations in results could not be explained when changes were made to the simulation parameters.

In a partial discharge application [14], an RC is modelled as a 2^{nd} order circuit with the capacitance made up of winding to return winding capacitance along with an inter-winding capacitance. However, they disregard the effect the inter-winding capacitance has since it is much smaller than the winding to return winding capacitance. They also discuss the effect each element has on the gain of the RC but only from a theoretical perspective. It is interesting that they ([14]) considered the inter-winding capacitance at first since the capacitance is under dispute. It can be argued that since the capacitance is formed by a wire, which essentially ends a loop on itself, the capacitance is shorted. From a low frequency perspective this is certainly true, but at higher frequencies it might have an effect. The issue at hand now revolves around when the capacitance becomes problematic. In an informal study, the self-capacitance of solenoidal inductors were examined. The study tries to apply different theories and commonly acknowledged formulas to the self-capacitance, but some of the accepted theories available in literature do not hold true when examined against characterised commercial coil inductors [25]. The study also highlights a key insight as to when the capacitance will be valid. When the length of a single turn matches a quarter or half wavelength, then there might be maximum potential difference between the ends of the loop, giving rise to a capacitance to exist. Figure 2.9 attempts to illustrate this effect. The winding set on the right (B) of this figure shows significant difference in current magnitude between two points.

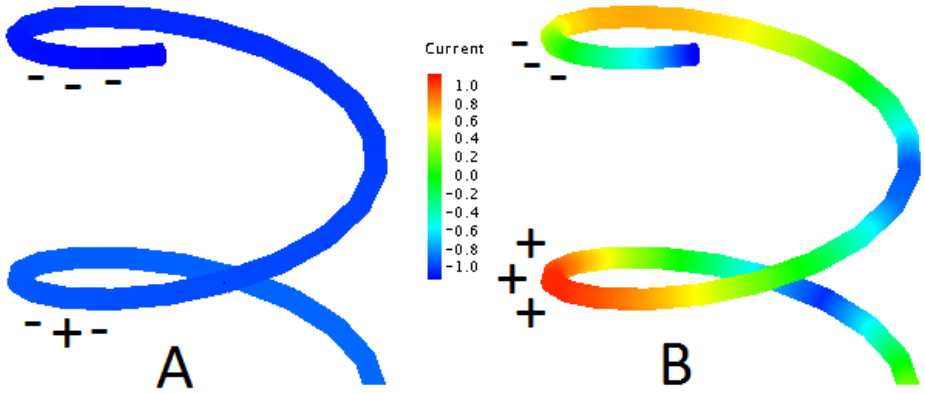

Figure 2.9: Normalised current distribution on windings at different frequencies. Winding B will have inter-winding capacitance due to the difference in charge flowing, and thus, difference in potential over two points

It is argued that for winding lengths smaller than a quarter wavelength of the suspected frequency, the potential difference induced between windings, and therefore the capaci-

tance will not be of significance. Furthermore, the suspected frequency will be higher than what the RC is intended to be used at. The focus also falls on large RCs, having few windings and therefore larger distances between the windings. For these reasons the capacitance between windings will not be considered.

2.2.2 Computational modelling

In addition to theoretical modelling, computational modelling provides insight into the working of the RC. While not a well covered subject, some literature does exist on computational modelling. In [26] a finite element method (FEM) is applied in modelling an RC and a bar conductor with the aims of observing how current distribution effects mutual coupling. However, the considered frequencies are in the low kHz range. In another study the partial element equivalent circuit method was used for the design of a printed circuit board RC [27]. This method was chosen over FEM due to its faster computational times at higher frequency ranges.

In [21] circuit modelling was done in TOUCHSTONE software. Capacitance modelling was also attempted in FEKO. Capacitances with known theoretical values correlated with simulations, but capacitances such as inter-winding capacitances differed substantially from theoretical values.

Previous large RC modelling was done within our department. The RC was modelled in FEKO. However, each winding was uniquely defined for the specific RC, making it difficult to change parameters for testing. Since computational modelling of large RCs is not extensively covered, it gives opportunity for modelling large RCs and the accompanying calibration fixture. Computational modelling can also be used for quick evaluation and optimisations such as sensitivity or bandwidth.

2.2.3 Bandwidth

From an EMC/RFI perspective, more bandwidth is usually preferred. RCs can attain bandwidths as high as 1 GHz [28], making them adequate for a wide range of applications. As with many other transducers, the bandwidth is primarily determined by the physical dimensions of the device. For the RC, low inductance and capacitance values will result in greater bandwidth [21]. Looking at eq. 2.2.3 the inductance of the RC can be decreased by having a smaller winding area i.e. a smaller ratio between b and a. This will also lower the sensitivity since it is mainly related to the mutual inductance. However, decreasing the winding area will increase the return winding capacitance, which will reduce the bandwidth. Thus there will exist an equilibrium point between the inductances and capacitances for which maximum bandwidth can be designed for.

Further design considerations include the number of windings the RC will have. Sensitivity will be increased with more windings, but bandwidth will diminish [19] [29]. A design assessment will have to be done to determine operating conditions since there exists a trade-off between sensitivity and bandwidth. With technological improvements in digitising equipment, sensitivity is less of a problem it once was. This study, then, is biased towards having less windings for increased bandwidth. Figure 2.10 (taken from [19]) shows the relationship between number of windings, Z_t (sensitivity) and bandwidth. With less windings, the distances between them becomes larger, which also gives more reason to ignore the inter-winding capacitance.

Another well-covered topic for bandwidth improvement is the effect of a terminating resistance. The idea behind the added terminating resistance is to dampen resonances.

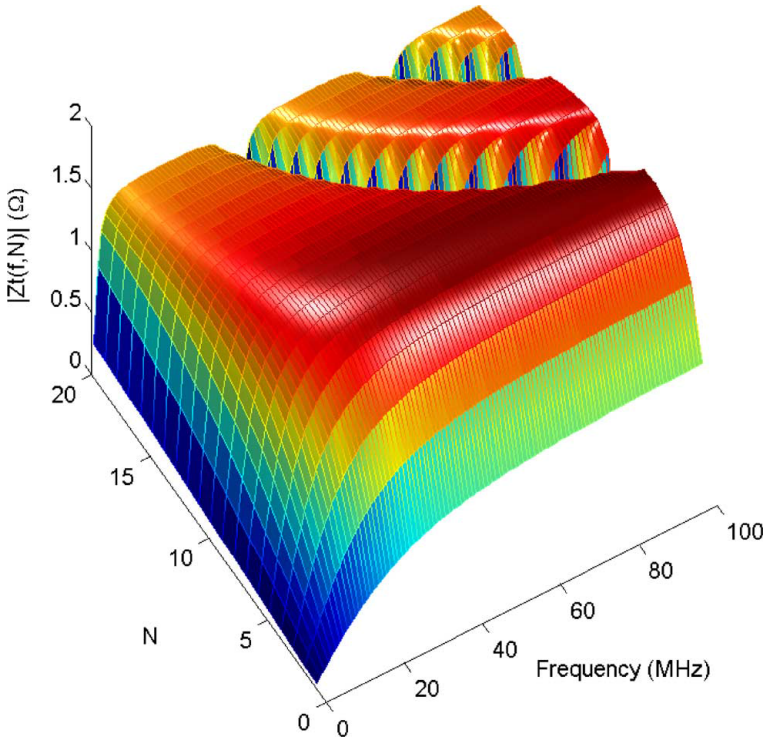

Figure 2.10: Three dimensional representation of Z_t vs. frequency with increase in number of windings (N) [19]. Observing the Frequency axis and keeping N constant, the transfer impedance has an integrating area (ascending slope) followed by a flat region (self integrating region). The first resonant dip can also be seen, and lowers in frequency as N increases.

If the RC is modelled as a low bandwidth 2^{nd} order circuit, the current originally flowing only through the capacitive element now flows through both the capacitor and resistor. A decrease in capacitor current causes faster rise and/or settling time [23]. When analysed with Laplacian theory, it is discovered that the terminating resistance should be less than the coil characteristic impedance Z_{coil} to avoid oscillation [30]. In eq. 2.2.5 self-inductance L_{self} and winding to return-winding capacitance C_{wr} is used.

$$Z_{coil} = \sqrt{\frac{L_{self}}{C_{wr}}} \tag{2.2.5}$$

Although an increase in bandwidth will be achieved by adding a terminating resistance, it is not pursued in this project. The focus falls on large RCs which relies on the wire for structural support. Adding a termination resistance will require a break in the wire, introducing a weak point unless other means of structural support is added. The resistance used will also have to be considered. Even surface mount resistors suffer from capacitive and inductive effects at sufficiently high frequencies. Although this can be accurately modelled and measured, the possibility exists that along with added resistance, the inductance and/or capacitance may be raised as well, effectively decreasing the bandwidth. This is yet to be tested.

Several RCs have been received for initial study (fig. 2.5). Among them was an RC with an electrostatic shield and termination resistance (D in fig. 2.5). This RC was only briefly studied for interest. The terminating resistance was soldered onto a small printed circuit board which made it very easy for conducting tests of including and excluding the resistance. Figure 2.11 shows the difference in the Z_t for the RC with and without a

terminating resistance. Overall the Z_t seems more smooth, which is due to the dampening of small resonances. However, the bandwidth appears the same, both having a phase zero-crossing at 185 MHz.

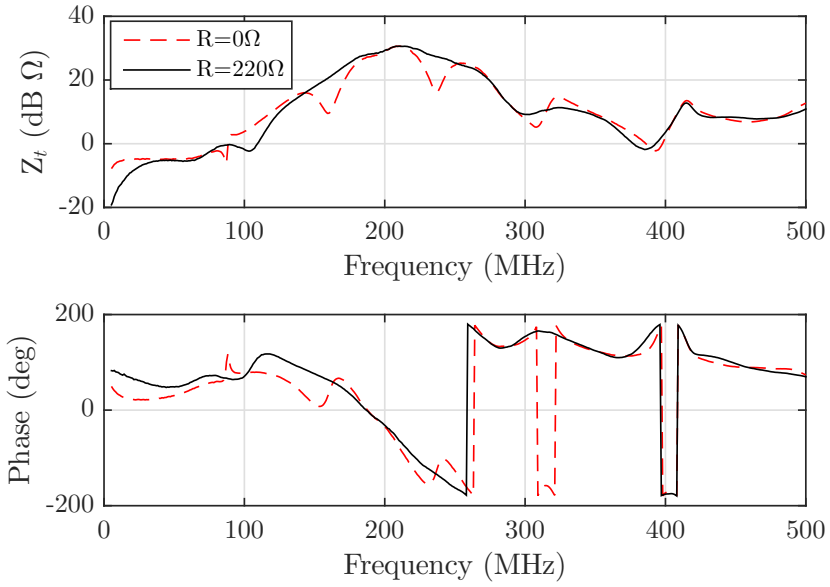

Figure 2.11: Effect of terminating resistance. The RC used in the measurement is D in fig. 2.5. A 220Ω surface mount resistor is used as the terminating resistance. It is soldered to a printed circuit board which made it possible to be shorted or included for different measurements

2.2.4 Return winding placement

The return winding serves as a negative pick up winding and compensates for induced signals from stray fields [13]. However, the inclusion of the return winding does increase inductance and capacitance, which decreases the lower resonant frequency of the RC [17]. Regarding the placement of the return winding, the mean radius of the RC is usually chosen. In fig. 2.7 the mean radius R is equal to $0.5(b-a)$. Equation 2.2.6 is given by [31] which uses the equivalent radius (R_e) for return winding placement and is a more accurate location for compensation of induced stray fields.

$$R_e = \sqrt{\frac{a^2+b^2}{2}} \tag{2.2.6}$$

2.3 Calibration

Measurement devices that operates over a defined bandwidth can usually be calibrated through various methods. For current transducers, calibration can be done by comparison against known characteristics or complete description of the system, eliminating unknowns.

A method widely used in power metering, partial discharge or fault monitoring is to calibrate an RC against another probe with known characteristics. For this calibration method, a conductor is excited with a pulse similar to what is expected in a real event

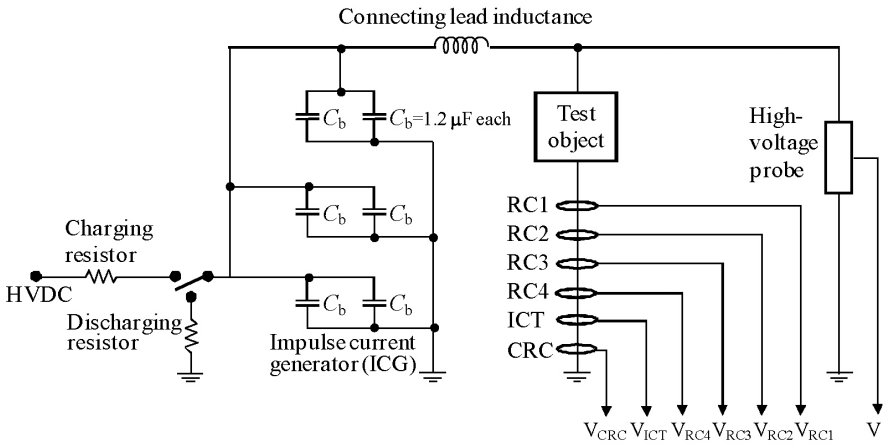

Figure 2.12: Schematic representation of partial discharge RC calibration setup used by [28]

and then measured with the different probes. Figure 2.12 taken from [28] shows a setup where the RCs are measured against a probe with known characteristics. In fig. 2.12 the real event is created by an impulse current generator. For some cases the RC is fitted with an integrator. The integrator components are calculated through theory [32] and fine tuned until a known waveform is measured. This method, although adequate for signals that either has a small bandwidth or are repetitive in nature, does not provide enough information about the RC and thus the measured signal.

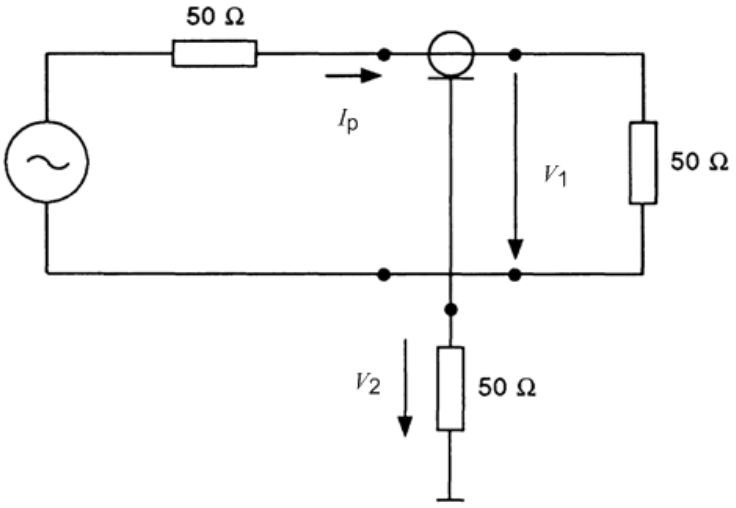

Figure 2.13: CISPR schematic representation for calibration of current probes [18]

A different approach is to calibrate RCs (and other current probes) in the frequency domain. Calibration in the FD gives detailed characteristics about the probe and a more intuitive understanding of the RC is formed. Figure 2.13 shows a schematic setup where a load is excited by a calibrated Vector Network Analyser (VNA). Reflection and transmission coefficient measurements are taken on port 1 and port 2, respectively. The measurements are then used in a transform to deliver a Z_t. The Z_t relates the current flowing in a conductor to an output voltage at the probe terminal (Ohm's law, eq. 2.3.1).

$$Z_t = \frac{V_2}{I_p} \tag{2.3.1}$$

For this calibration method, a CISPR standard (CISPR 16-1-2) is available and involves the use of a calibration fixture. The fixture's dimensions forms a matched coaxial transmission line. Illustrated in fig. 2.14 are standard Z_t curves for current probes as defined by CISPR [18]. While CISPR recommends total enclosure of the probe, the calibration fixture is more or less probe specific and can be costly to fabricate.

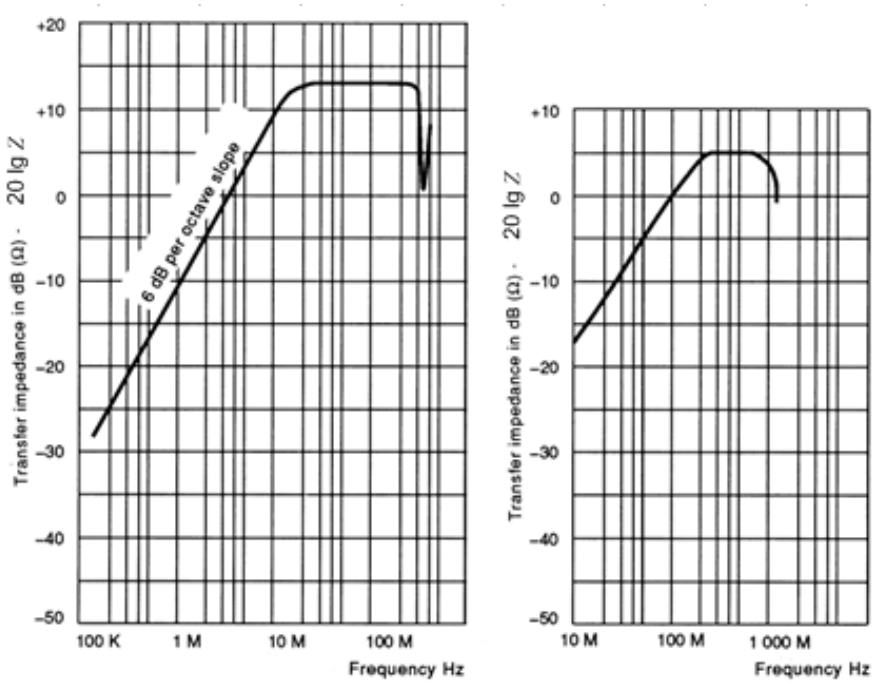

Figure 2.14: CISPR Z_t description for probes with different frequency bands[18]

An adoption of this standard is commonly used by current probe manufacturers. The adoption involves a 'U' type fixture that is constructed with two 'L' plates and a conductor connecting two ports that go through the 'L' plates. Figure 2.15 shows a calibration fixture for small current probes made by Fischer Custom Communications [33].

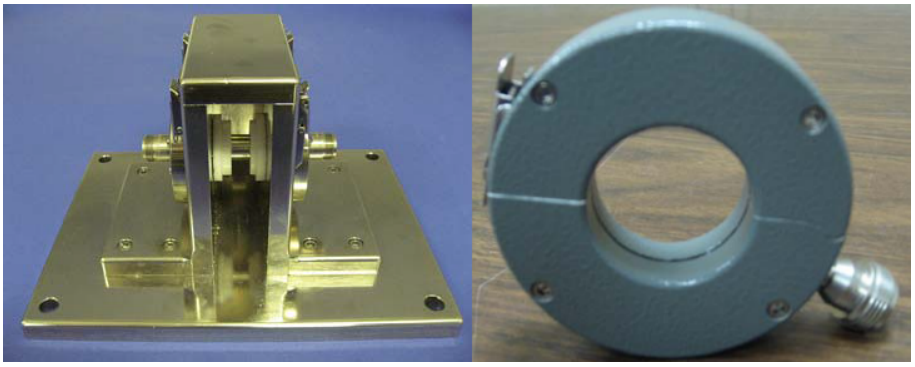

Figure 2.15: Fischer FCC-MPCF-3-32/71/1 calibration fixture and F-62 current probe with an inner diameter of 32 mm [33].

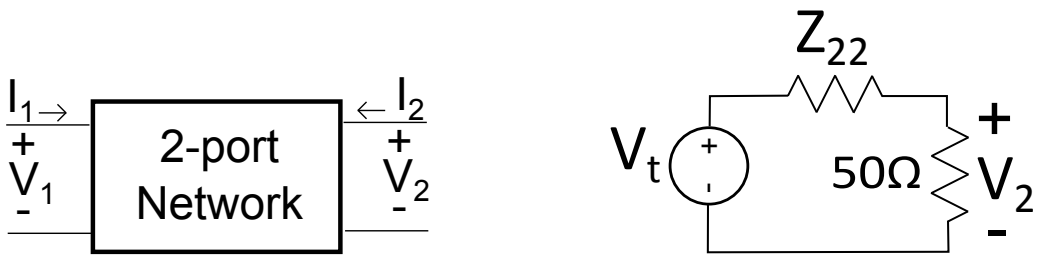

(a) Two port network. (b) Circuit with correction elements.

Figure 2.16: Two port network and correction circuit. V_t is the loaded transfer voltage. Z_{22} is the self-impedance of the probe.

The probe to be calibrated is placed around the conductor and the response of the probe along with the reflection coefficient of the fixture is measured with a VNA. The Scattering parameters (S-parameters) can be converted to impedance parameters (Z-parameters), or be measured directly if the capability is available. Observing the two port network in fig. 2.16a, the voltage V_2 can be used directly to calculate the transfer impedance in eq. 2.3.2. However, this warrants the measuring device to have an infinite input impedance (I_2=0A).

$$Z_{21} = \left.\frac{V_2}{I_1}\right|_{I_2=0} \tag{2.3.2}$$

For 50Ω systems a correction factor must be applied since a loaded 2-port network is present. The correction is a simple voltage division factor (eq. 2.3.3) which stems from the circuit in fig. 2.16b. The same correction is applied to the actual Z_t which is measured (eq. 2.3.4).

$$V_2 = 50\frac{V_t}{50 + Z_{22}} \tag{2.3.3}$$

$$Z_t = 50\frac{Z_{21}}{50 + Z_{22}} \tag{2.3.4}$$

While Z-parameters can be used, S-parameters are usually readily available from a VNA measurement. A conversion between Z-parameters and S-parameters exist which allows the Z_t to be expressed as :

$$Z_t = 50\frac{S_{21}}{1 - S_{11}} \tag{2.3.5}$$

This is useful since it requires less post-processing. For both cases the result is a Z_t over the working bandwidth of the coil that can easily be used with eq. 2.3.1.

2.3.1 Full de-embedding

While the straight FD approach is best suited for current probes with tight-fitting fixtures, there have been studies exploring the use of an enlarged fixture. The main reason for using a larger fixture is ease of use for a variety of probes. In [34] they explore the effects of a slightly enlarged fixture and found that for very low frequencies, the Z_t is only related to the characteristic impedance of the measurement system and the transmission coefficient of the excitation port and the probe port (S_{21}). At higher frequencies the mismatch becomes significant and must be accounted for. Not only do they include the effects of the mismatches, but also delve into the topic of which current to use when defining the

Variable/Meaning	
τ	Transmission coefficient
ρ	Reflection coefficient
Z_c	Measurement characteristic impedance
β	Propagation constant
y	Fixture length

Table 2.1: Variables for eq. 2.3.6

Z_t. In later work they extend the approach to accompany very large calibration fixtures [35]. In both [34] and [35] they use eq. 2.3.6 as the Z_t. The variables used in this equation are listed in table 2.1. This transform resembles eq. 2.3.5 with an added section that accounts for 'junction reflections' (reflections due to mismatch).

$$Zt = \frac{\tau Z_c}{1-\rho}\frac{1-\rho e^{-2j\beta y}}{e^{-j(\beta y/2)}+\rho e^{-2j\beta y}e^{j(\beta y/2)}} \tag{2.3.6}$$

Laying the foundation for high frequency current probe calibration, the work done by [34] was later refined in two articles. Mainly focusing on the transitional effects between characteristic impedances (from 50 Ω to Z_c in eq. 3.3.1), the articles describe the system completely in terms of S-parameters whereas the initial work focussed on the effect of junction reflections. Focussing on the S-parameters, [36] provides a detailed approach to de-embedding the influences of the calibration fixture on the current probe. This is done by defining the fixture as two 2-port systems - from the first junction to the probe plane and from the probe plane to the second junction. These two 'half' systems are symmetrical if the probe plane is in the middle of the fixture. A two port fixture measurement is made of the empty calibration fixture from which the half systems are deduced followed by a three port measurement in which the current probe is included. A new set of S-parameters for the probe are then calculated from the measured parameters and the half-system parameters. This results in a de-embedded set of S-parameters for the current probe. Unfortunately [36] does not state the Z_t transform they use, but adequate results are achieved to within ± 2 dB Ω as specified by the manufacturer.

Relying heavily on work done by [36], [37] also attempts to characterise and model current probes. They include a lumped element circuit model for the junction which consists of a vertical plate (fixture wall) and a SMA connector (port connection). The parameters of this circuit along with a half length of the fixture transmission line characteristic impedance is then solved with a genetic algorithm. A macromodelling approach is applied in characterising the current probe. The end result is good agreement between measurements and simulations, thus achieving a model of good accuracy.

Unfortunately the full de-embedding process could not be applied to the commercial CPs or RCs since time did not allow it.

2.3.2 Time domain

Achieving good results for the FD approach, [36] employed a TD approach to extend the frequency range of the calibration to cover the entire bandwidth of their CP. In this approach reflections are eliminated by gating out unwanted responses in the signal induced in the CP. The reason for employing a TD approach is to eliminate the numerical error and instability the FD has at higher frequencies. Their TD method implementation delivers good results at frequencies higher than 400 MHz. A hybrid Z_t is then formed

with the lower frequency data from the FD approach and high frequency data from the TD approach.

2.3.3 Conductor placement

A simple yet exact setup is needed for calibration and must be repeatable. An offset in conductor placement will result in an error present in the calibration. One possible offset is portrayed in fig. 2.17. Studies have been done to show the effect of having an offset in conductor placement [20] [38]. The first concern would be that since the RCs' one side might be closer to the conductor, it will pick up stronger B fields than the other side. Examining Faraday's law, we see that if we enclose a current and integrate the B field along this closed path, the total current will be calculated. Thus, the offset should not influence current measurements. The capacitance between the current carrying conductor and return windings (C_{ws}) is of more concern though. Care should be taken to eliminate all offsets, especially during the calibration process.

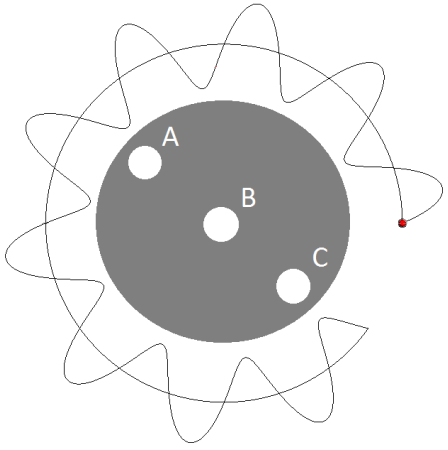

Figure 2.17: Different conductor placements. The grey area represent possible placements with position B the centre and correct placement. Positions A and C will introduce errors.

2.3.4 Higher permittivity

For an experiment to improve matching between the measurement line impedance and the fixture line impedance, the use of a high-permittivity dielectric is considered. This will cause the line impedance and signal speed to lower with the square root of the relative permittivity. For the latter, it must be ensured that the material is only used in its dispersion-free region.

Although the dispersion can be accounted for in the de-embedding process, the dielectric characteristics will have to be known. This will introduce complexity to the process, hindering repeatability for those with equipment limitations, i.e. does not have permittivity measurement/calibration equipment.

In-house permittivity measurements were made (with thanks to Dr. Andriambeloson). Fig. 2.18 shows the permittivity of the measured dielectric. Distilled water was used as the high permittivity medium. It can be seen that permittivity does change at higher frequencies, thus dispersion might occur.

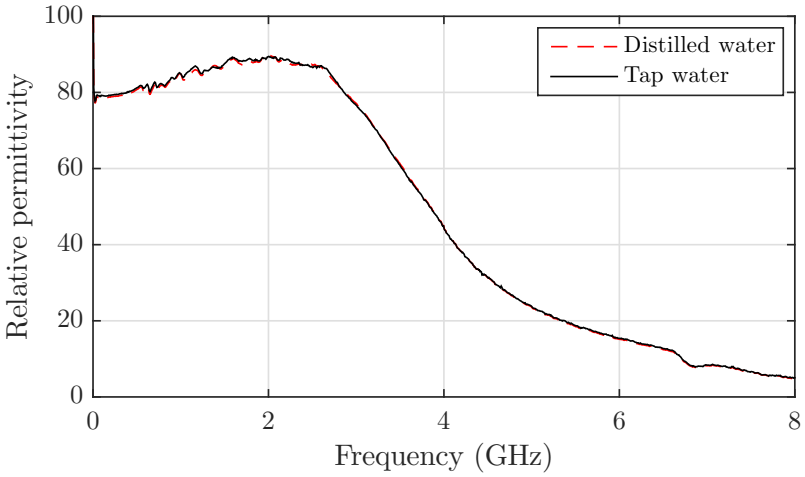

Figure 2.18: In-house relative permittivity measurement of distilled water.

The last topic that was raised concerning the higher permittivity material is the effect it has on the connectors. Since connectors are costly, they must not be contaminated with another dielectric, changing their properties.

2.4 Conclusion

With the basic knowledge of lightning spectra, RCs and calibration being acquired, we can continue in evaluating the RCs acquired for this study. It is established that lightning spectra will be considered up to 50 MHz. This low bandwidth requirement along with the RC's isolation and non-saturating characteristics make it a viable and commonly used transducer in lightning studies. Complementary EMC and coupling investigations on the SKA warranted investigation into higher frequency calibration as well

The different methods for calibration are also explored. Since we want to know specific characteristics about our signals, we will follow the method which results in a Z_t. Frequency domain calibration will be investigated first and verified with a commercial CP.

Chapter 3

Rogowski Coils

The literature review examined a broad array of aspects of the Rogowski coil and methods to characterise it. This chapter will continue, starting with a theoretical model that is an adequate representation of the RC. Computational modelling will be included and will give extra insight in resonances inherent to the RC. Characterisation in the form of calibration is examined and receives the most attention. To verify the calibration in both the time domain and frequency domain, commercial current probes are calibrated against their known transfer impedance. Two experiments are also done with the aim of improving signal transfer characteristics of the fixture.

3.1 Theoretical Model

The CISPR 16 standards describe a Z_t of a typical CP as having a non-integrating area, followed by a flat, integrating area before major resonances occur (fig. 2.14). Normal RC transfer function characteristics are not far from this description and similar results have been obtained in other studies. In [19] an RC is presented along with a theoretical model that agrees beyond its first resonance of 51 MHz. However, this RC is used in an application specific way, which allows for complete system description and produces results that correlate over theory, simulation and measurement. Since our RCs will be used with an EMC perspective in mind, it becomes difficult in deciding what elements of uncertainties to include in the model, simulations and measurements. The choice is made to calibrate in lab conditions and discover maximum bandwidths through testing.

It was decided that the transmission line approach will be used for modelling the RC. Figure. 3.1 shows the transmission line with lumped elements for mutual inductance ($L'_m dx$), self inductance ($L'_s dx$), a resistive element due to the skin effect ($Z'_{skin} dx$), and a capacitance which is present due to the coupling between the windings and return winding ($C'_{wr} dx$). The length lw is the total length of the return windings and includes the return winding.

3.1.1 Model components

While it is permissible (reasons stated earlier) to have the inductance as a function of area, the precise models for capacitance and inductance are not computationally expensive, and will be used. Since the inter-winding capacitance has been excluded from further study and the winding to source capacitance is too geometrically complex to model analytically, the only remaining capacitance, for an RC with no added shielding, is the winding to

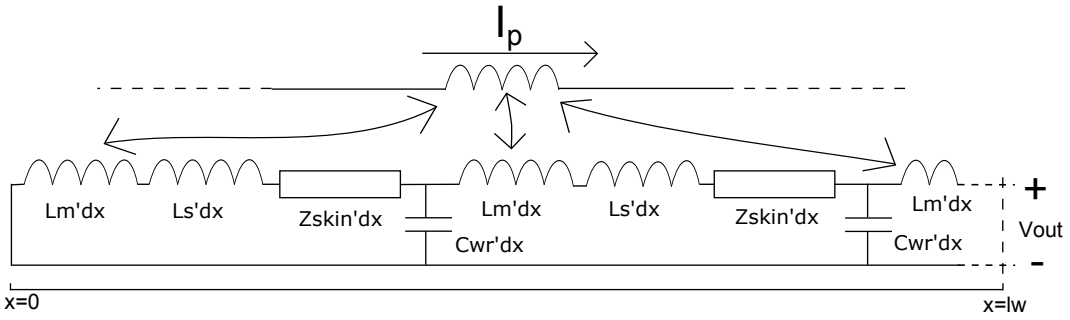

Figure 3.1: Transmission line model of RC

return winding capacitance in eq. 3.1.1 [21]. This capacitance (eq. 3.1.1) takes into account the total length (l) of the RC and also the pitch of the windings through a coverage factor (F). The coverage factor is inversely proportional to the pitch since an increase in pitch will increase the distance between windings which will cause a decrease in capacitance. For a large RC, the windings will be far apart, thus a low coverage factor is used.

$$C_{wr} = \frac{2\pi\epsilon \cdot F \cdot l}{\ln(\frac{b-a}{d_{wire}})} \tag{3.1.1}$$

When using the RC model in [19], a transfer impedance as shown in fig. 3.2 is obtained. This is shown along with simulation and measurement results. Certain similarities and differences are notable. All three calculated Z_t (theoretical, simulation and measurement) correlate relatively well up to 100 MHz. Discrepancies beyond 100 MHz can be attributed to the model not fully describing the simulated and practical setup. The theory only describes the RC, but not the surrounding environment, which includes the calibration fixture shown in fig. 3.3. A better theoretical model would include a capacitance to ground, representing the fixture walls and ground plane. Due to the geometrically difficult description of capacitance between windings and a ground plane, the capacitance is not included in the model. The model can be found in the Matlab code in Appendix B under section B.1.

3.2 Computational modelling

Most, if not all of the simulations for the FD approach were done in FEKO with a MoM approach. Figure 3.3 shows the FEKO discretised mesh setup (left) and the physical setup (right). All of the simulations were done with the low detail as shown in fig. 3.3. A simulation was done with the added detail of the fixture, but the increase in simulation time could not be justified for the small increase in accuracy (fig. 3.4).The frequency span of the simulation was limited to 300 MHz.

For the lower part (<100 MHz) of the considered frequency range, good agreement is achieved. The deviation above 100 MHz especially around the first resonances can be attributed to the model used. In the theoretical model no elements are present for a ground plane. The simulation tries to simulate the physical model adequately and does include ground planes and walls (fig. 3.3). It is expected (and observed in fig. 3.2) that the simulation and measurement show better comparison.

An open space simulation was also done to see which resonances corresponds to which physical attribute. The fixture was excluded and only a single excitation line was used,

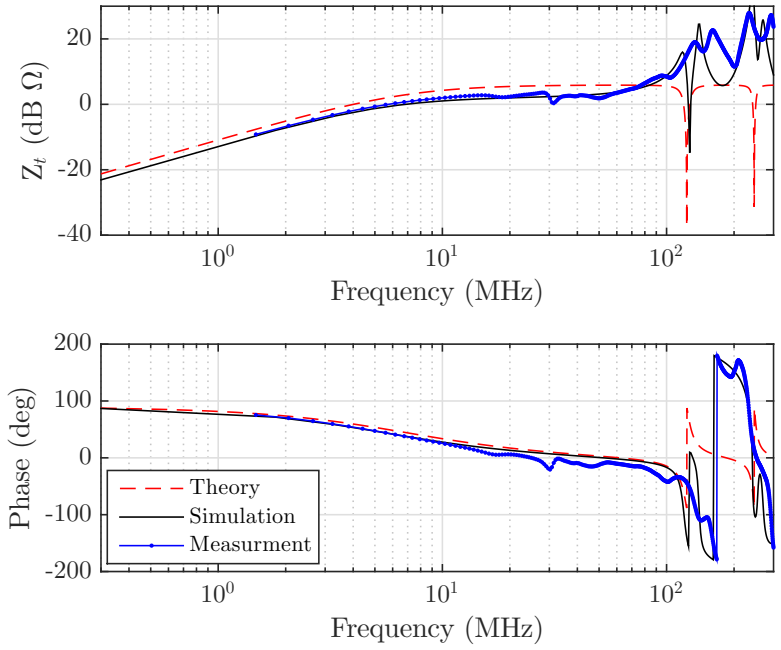

Figure 3.2: Large RC Z_t: obtained through theoretical, simulation and measurement. These results are attained with the frequency domain approach.

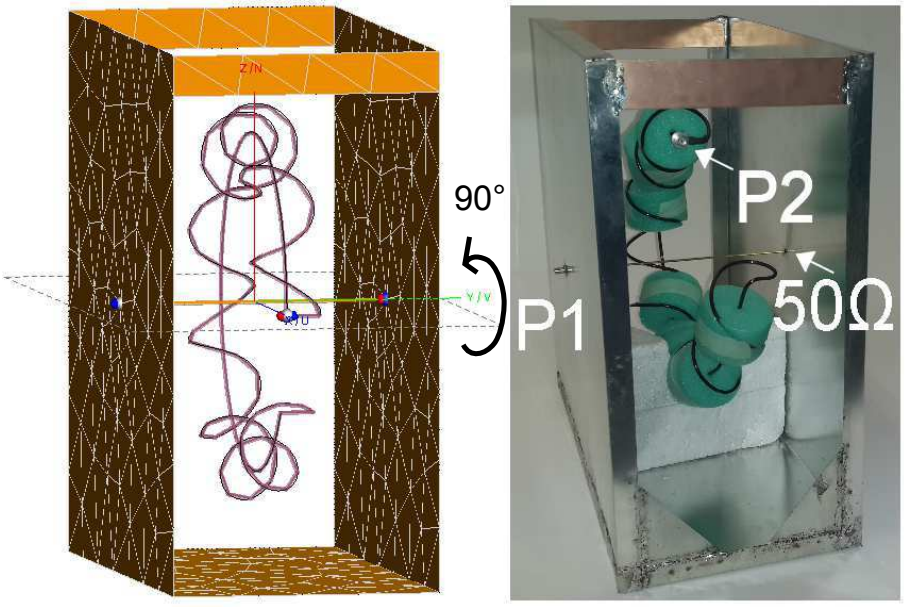

Figure 3.3: Newly fabricated fixture for initial frequency calibration. Simulation on the left, physical setup on the right. Physical RC is rotated 90° around the Y-axis as indicated.

with its length being the only variable adjusted. The results are shown in fig. 3.5 Two resonant frequencies were identified, belonging to the RC itself. A third resonance present in the Z_t is believed to stem from frequencies exciting the full-wavelength resonance of the RC. The frequency of 116 MHz has a wavelength of 2.56 m which is the total length of the RC wire.

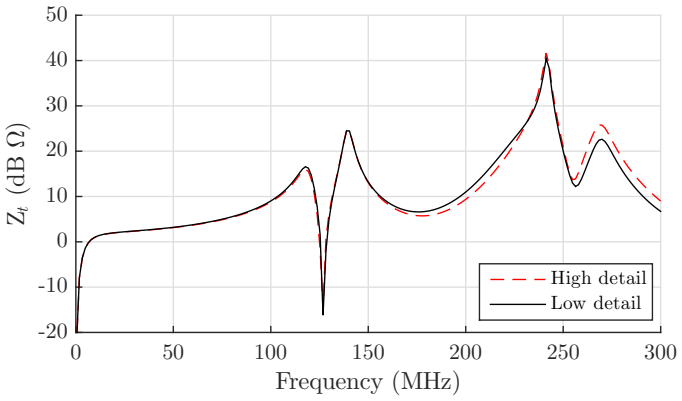

Figure 3.4: Transfer impedance comparison when more fixture detail is added. The high detail model resembles the physical model exactly, shown in fig. 3.3.

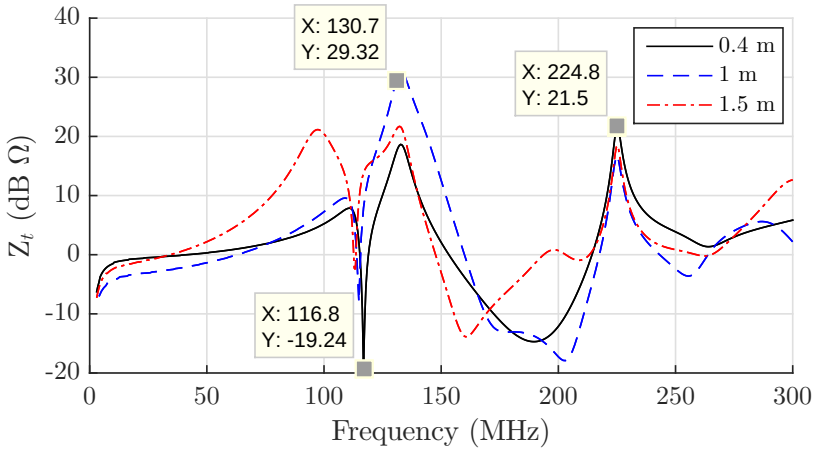

Figure 3.5: Transfer impedance of the open space simulation. Only the excitation line length was varied.

3.3 Measurement and calibration

The basic setup for the FD approach is as described in the literature study (chapter 2.3). The TD approach utilises the same setup, with the exception of a longer fixture. The VNA (in our case a Rohde &S Schwarz model ZVB 8) is calibrated with an open, short, matched load and through calibration standards for both ports 1 and 2 over the necessary frequency bands. For FD, lower frequency content is needed and the VNA is setup for 300 kHz to 300 MHz. To ensure a clear response in the time domain the pulse needs to be as narrow as possible. Narrowing the pulse is achieved by including high frequency content. The VNA has a maximum span of 8 GHz and the full span is utilised. The frequency content is set up with a starting point of 976.6 kHz and 8191 points in incremental steps of 976.6 kHz is set up. This allows for harmonically related points and after extrapolating a dc point, 8192 points are recorded. 8192 is a power of 2 which can be useful for fast Fourier transforms in base 2. A variable length fixture is used which was fabricated in a previous study (fig. 3.6). The fixture consists of two 'L'-bent metal sheets, joined on the ground plane with conductive tape. The length was set to 500 mm which allows for enough settling time with the mentioned frequency range.

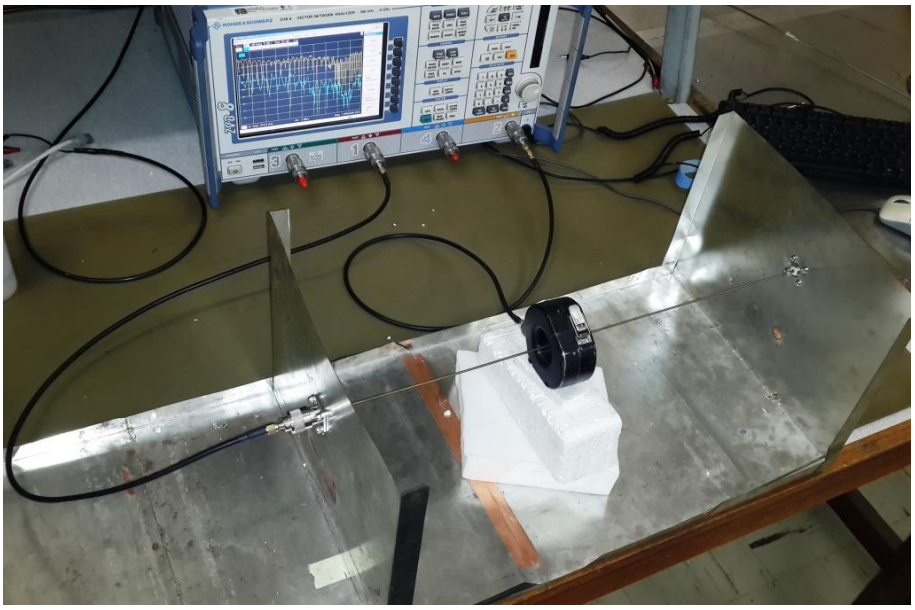

Figure 3.6: Measurement setup used for calibration. In this setup is the VNA with port 1 connected to the 500 mm calibration fixture and port 2 connected to the ETS CP. Port 3 is left open since this is a TD calibration measurement. This fixture has an extendible length.

3.3.1 Frequency domain

Initially the RCs were calibrated with an FD method explained in the literature study (chapter 2.3). For small RCs a calibration fixture existed since it was fabricated for previous work done by [21] and other final year students. However for the large RC, a new calibration fixture (shown in fig. 3.3) had to be made to accompany its physical size. This calibration method had difficulty in obtaining repeatable results at higher frequencies. The Z_t is very dependent on the position of how the RC is placed in the fixture and the first low frequency resonances may differ significantly for two measurements.

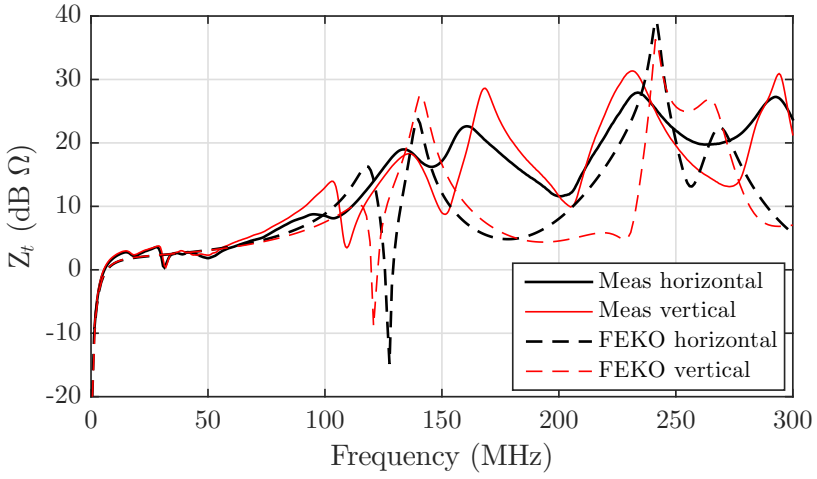

Figure 3.7: RC orientation placement. The RC was measured in the position as shown in the simulation (fig. 3.3) for the horizontal case and rotated 90° as shown in the physical setup for the vertical case.

The difficulty in deciding on RC placement is one of the reasons this calibration method is abandoned. Figure 3.7 shows the difference a 90° rotation around the y-axis (fig. 3.3) makes on Z_t. For the measurement there is a 3 dB difference before 100 MHz and in the vertical case a small resonance is present at 110 MHz. It is uncertain as to what causes these effects since no new capacitances are added and the path of flux intercept remained more or less the same. A subject of discussion was the new cable path and close proximity encounters with the fixtures. A test was devised where a second ground plane is added through which the RC port is connected. Three shorter cable lengths were tested to evaluate the effect it has on Z_t. The test could not explain the change in Z_t when the RC is rotated 90° axially.

Although good results were achieved for the lower part of the bandwidth of the RC, the large fixture had drawbacks for frequencies higher than 50 MHz. This can be seen in a measurement (fig. 3.8) of the ETS CP measured in different fixtures. The large (D) and small (C) fixtures had a difference of 3 dB compared to the calibration data at 130 MHz. The fixtures and their dimensions can be seen in fig. 3.9 and table 3.1, respectively.

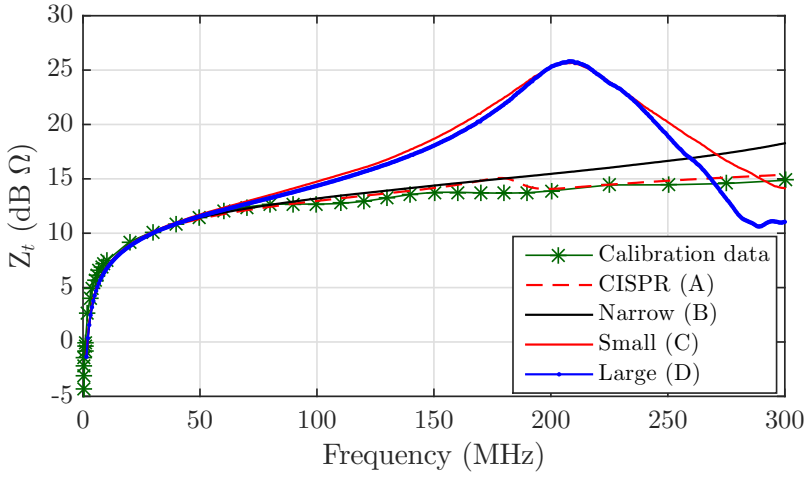

Figure 3.8: Z_t of the ETS CP in different fixtures shown in fig. 3.9. For the large fixture, the Z_t deviates 3dB from the calibration certificate at 130 MHz.

Dimensions in mm				
Fixture	Length	Width	D	d
A	-	-	117.5	14
B	60	200	60	2
C	250	200	50	2&30
D	200	400	200&240	2
TD1	500	300	50&130	2&30
TD2	1016	300	50&130	2&4

Table 3.1: Dimensions for the fixtures in fig. 3.9. Dimensions D and d are shown in fig. 3.10. For the CISPR type fixture, D and d represents the inner wall diameter and conductor diameter, respectively.

While already achieving good results with the FD approach which will provide ample bandwidth for the discussed lightning signals, having more bandwidth allows to extend

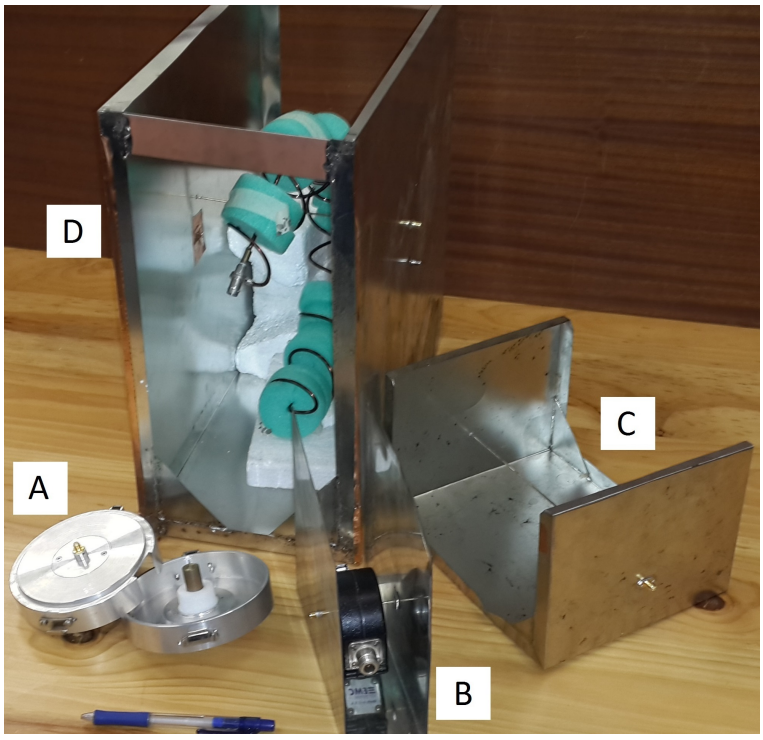

Figure 3.9: Different FD fixtures that were used in this study. A: CISPR type fixture, B: Narrow U-type fixture, C: larger fixture also used for the half-fixture (250 mm) measurement in the TD approach, D: fixture for the large RC with the RC supported by pieces of polystyrene foam

the usefulness of the probe for complementary EMC and coupling studies on SKA dish structures. Due to the larger size of the new fixture, its resonant frequency is lower, limiting our abilities to calibrate RCs with potentially higher bandwidths. Standing waves also become problematic with high frequencies and large fixtures as shown in [39]. However, they use this to their advantage and compare measurements to simulation data, resulting in known voltages and currents which can be used to derive the Z_t.

To resolve the difficulties at higher frequencies a TD approach was investigated.

3.3.2 Time domain

The TD method entails the analysis of the S-parameters in their TD format. The TD signals are obtained through the inverse fast Fourier transform of the FD S-parameters, acquired from a calibrated VNA measurement. The frequency content will form a Gaussian pulse in the TD which travels along the fixture line as time progress. Adequate high frequency content is needed to form a narrow pulse. A narrow pulse along with a fixture that is of adequate length will ensure that individual responses are distinguishable. In the TD domain we can easily identify problematic responses and correct them by applying a time gate [40]. Figure 3.10 shows how a reflection coefficient relates back to fixture characteristics. After the signals are corrected, they can be transformed back to the FD and a transform similar to eq. 2.3.5 can be applied to calculate the Z_t.

The first step is to make sure that the responses are distinguishable from each other i.e. enough settling time exists between two consecutive responses to allow gating. This can be done with some basic propagation theory. The signal will have a propagation speed, equal to (a fraction of) the speed of light c and will travel a certain length in a certain

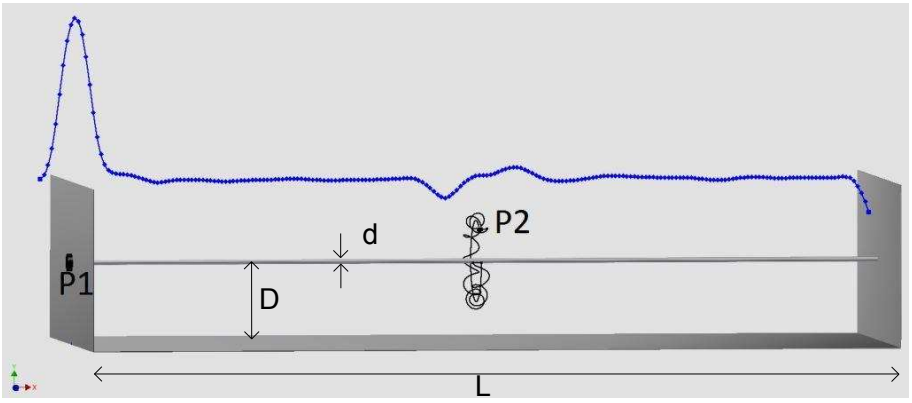

Figure 3.10: TD signal representation for a long fixture. The length of the fixture, conductor diameter and height above ground plane is L, d and D, respectively.

amount of time. This can be used to design a calibration fixture that will allow sufficient settling time. It is recommended that the settling time is equal to the pulse width. This stems from measurement observations. In the TD, the fixture length L should be 4 pulse widths long to allow the responses to be properly distinguishable from each other. It is also beneficial to have as narrow a pulse as possible. This can be achieved by adding high frequency content.

If a fixture is chosen that does not limit the approach, the signals can be recorded, transformed to the TD and then be analysed. We start with the first reflection observed in the reflection coefficient, S_{11} (t=0.1 in fig. 3.11). This reflection resembles the mismatch between the measuring device's characteristic impedance and the fixtures line impedance. Transforming the gated signal back to the FD, fig. 3.12 shows the frequency content of

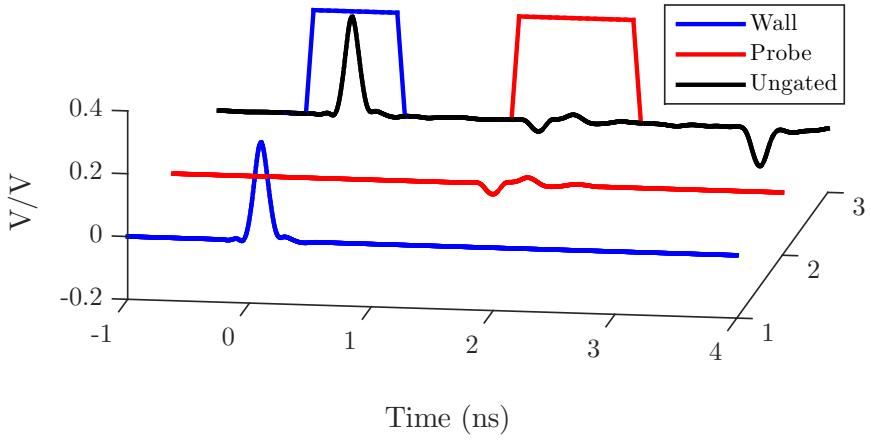

Figure 3.11: TD signal breakdown of the reflection coefficient for the ETS 94111/1L CP in a 500 mm fixture. The trapezoidal waveforms represent the gates and are the same colour as the gated signals (*Wall* and *Probe*).

the original and gated responses for the fixture wall and probe response at t=0.1 ns and 1.7 ns respectively. In figures 3.11 and 3.12 corresponding colours are used. The gated reflection coefficient of the fixture wall correlates to the having a reflection coefficient of 0.69 when eq. 3.3.1 and 3.3.2 is used to calculate a coefficient.

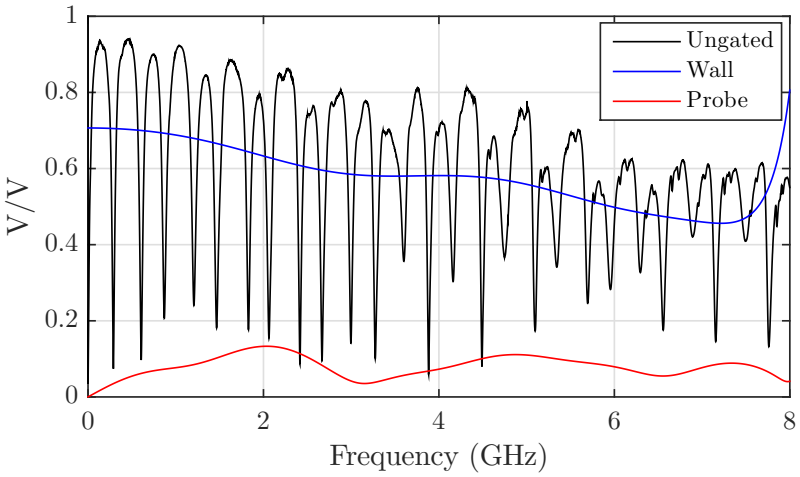

Figure 3.12: FD data with the original and gated signals. Over the frequency span of interest (0-1GHz) a reflection coefficient of 0.69 correlates with theory.

$$Z_{o1} = \frac{1}{2\pi}\sqrt{\frac{\mu_o\mu_r}{\epsilon_o\epsilon_r}}\,\text{arccosh}(\frac{D}{d}) \tag{3.3.1}$$

$$\Gamma = \frac{Z_C - Z_O}{Z_C + Z_O} \tag{3.3.2}$$

The correction factor can now be established from the gated FD response. This essentially becomes a transmission coefficient correction given by

$$A = S11_{wall} + 1 \tag{3.3.3}$$

All the other signals must be corrected for with this gated signal.

The second correction factor is derived from the signal that should have been received. This signal is acquired with the through measurement of a shortened fixture. Shown in fig. 3.13 are all the signals of interest and in frame D the shortened fixture through measurement. The shortened fixture length is half the length of the full-length fixture if the probe is placed in the middle of the full-length fixture. This signal must be corrected for the reflections at both wall ports. The correction is done in eq. 3.3.4.

Depending on the precision of fixture fabrication, the gated reflection in S_{11} can be used for both wall corrections. Ideally though, the correction of each wall port should be determined by the first reflection associated with the specific port, as was done in this project. This is shown in frame C of fig. 3.13 and results in correction factors A_1 and A_2.

$$B = \frac{S21_{through}}{-A_1A_2} \tag{3.3.4}$$

The correction factors have now been established and the gated signals of interest can now be de-embedded. Shown in frame B fig. 3.13 is the response and the gate of the signal induced in the probe - in this case the ETS CP. The gate length is determined by the amount of time it takes for the end wall reflection to reach the probe. Thus, assuming the probe is placed in the middle of the fixture of length L , the maximum gate length will be:

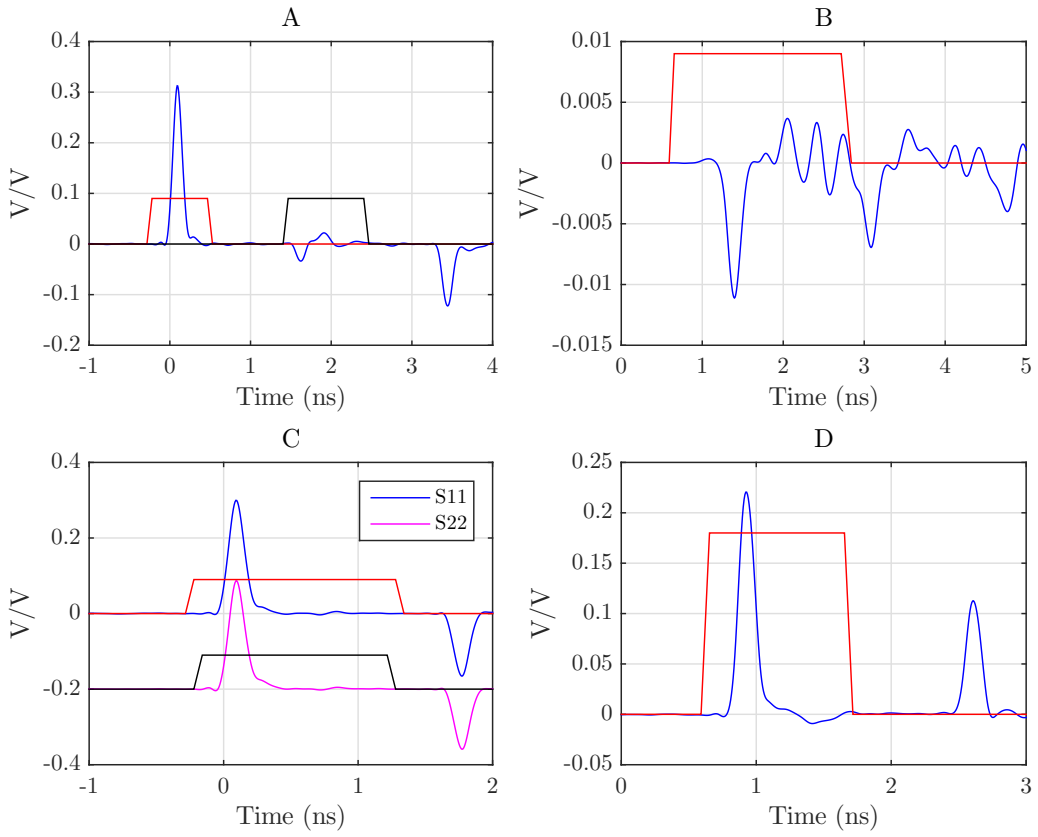

Figure 3.13: Relevant time signals and their gates; A. fixture mismatch and probe effect on line, B. induced probe response, C. half fixture mismatch and D. half fixture through measurement. The accompanying FD signals (original and gated) can be found in Appendix A.

$$T_{gate} = \frac{L}{c} \tag{3.3.5}$$

The correction factor eq. 3.3.4 is then applied to correct for the signal actually received along with the mismatch correction in eq. 3.3.3. This results in the corrected response:

$$C = \frac{S21_{probe}}{AB} \tag{3.3.6}$$

The last signal to be de-embedded is the reflection at 1.7 ns in frame A fig. 3.13. This reflection is due to the influence of the probe on the line and needs to be corrected for by eq. 3.3.3 and eq. 3.3.4. The corrected response is then

$$D = \frac{S11_{probe}B}{-A} \tag{3.3.7}$$

After the signals of interest have been de-embedded, eq. 3.3.8 can be applied to calculate the Z_t. This equation is the same as eq. 2.3.5 except for the respective embedded responses are replaced with the now de-embedded responses (eq. 3.3.6 and 3.3.7). The entire process is done in post-processing in the Matlab environment. Included in Appendix

B is the code for full de-embedding in the TD.

$$Z_t = 50\frac{C}{1-D} \tag{3.3.8}$$

Figure 3.14 shows the result of this procedure and is compared to the calibration certificate of the current probe. The lower frequencies (<100 MHz) are deviating from the calibration certificate. This is due to gating out the long time constant which is related to the lower part of the spectrum [36].

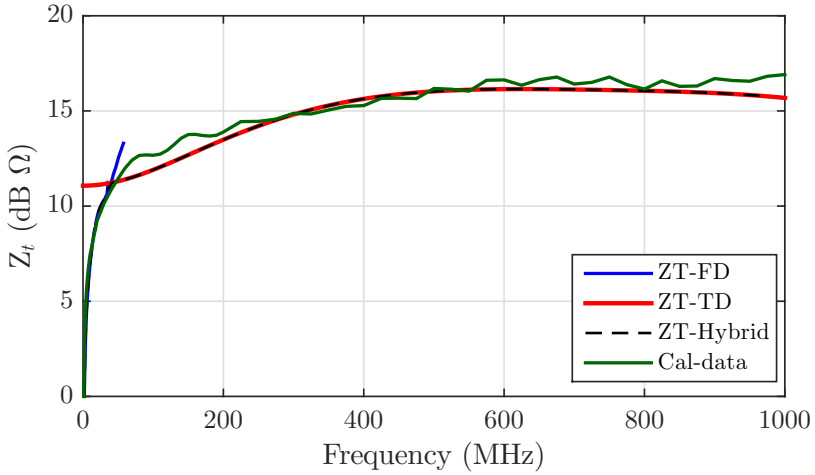

Figure 3.14: Calibration attempt of ETS 94111-1L current probe. The results relate to a measurement setup similar to what is shown in fig. 3.6. A 500 mm fixture was used with a 2 mm conductor which was placed 50 mm above ground.

A similar measurement was made with the Fischer CP and the results are shown in fig. 3.15. Marginally better low frequency performance was achieved for the calibration of the Fischer CP. Included in this figure is a measurement which utilised a 1 m fixture, allowing for more settling time. Far better low frequency performance was achieved. Initially this was thought to be the result of having a longer settling time, but if the calibration data is studied, there is a significant difference between the two probes. The ETS probe has data given down to 20 Hz where the Fischer probe only has data down to 10 MHz. The better performance of the Fischer CP can be attributed to the lack of induced low frequency content, resulting in a shorter settling time and the allowance of using a shorter fixture. To achieve the same results with the ETS CP, an impractical long fixture will be required.

This approach then is better suited for the higher frequency range of the Z_t. In [36] it is suggested that a 'hybrid' method of characterisation is applied, i.e. both the FD and TD are used. For the lower part of the spectrum the ungated signals can be used directly, followed by the TD approach data which will cover the higher frequencies. A transition region will be included which utilises linear interpolation to join the two frequency ranges. The hybrid method was applied to the ETS CP and the result is shown in fig. 3.14.

3.4 Calibration Fixture experiments

The TD approach was proven with the ETS and Fischer CPs as a precursor for RC calibration. However, early experiments exposed a weakness in this method. Due to the

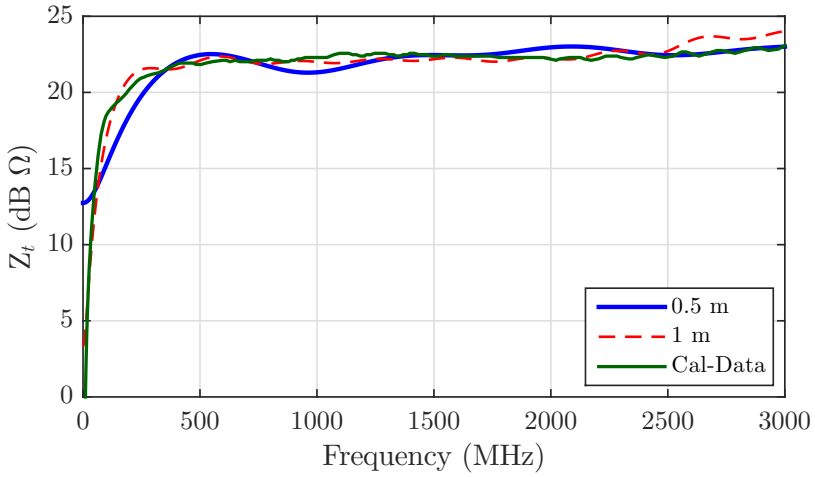

Figure 3.15: Calibration attempt of Fischer CC F-2000-12mm current probe. This probe performed better than the ETS probe due to the lower levels of induced low frequency content.

RCs' pick-up windings being relatively far from the source wire, the B-fields are smaller. This, along with a large reflection (t=0.1 in fig. 3.11) occurring due to mismatch, a smaller signal arrives at the RC and the induced signal may be indistinguishable from other artefacts stemming from noise. Two approaches were tested to decrease the mismatch between the VNA and the fixture. The first approach aims to improve matching by using a higher permittivity dielectric in the fixture whereas the second approach increases the conductor diameter. Both ideas stem from changing variables in eq. 3.3.1 as this will change the characteristic line impedance [41].

3.4.1 Higher permittivity

The first approach is rather ambitious and introduces its own limitations. By increasing the relative permittivity, the signal speed and characteristic impedance will decrease with the square root of it (eq. 3.3.1).

A liquid (distilled water) was proposed due to its ease of being a uniform medium. Using a liquid raises certain concerns. The first topic of concern is connector care. Previously used SMA connectors were salvaged from old projects, but are not naturally water proof. While leaking and a potential mess is of little concern (it can always, and was cleaned up), the addition of a lining of liquid between the Teflon and outer connector wall will change the characteristic impedance and create extra reflections, which are difficult to account for. The liquid that stays in the cable and connector after use is not as much of a problem since the liquid can be disposed of through slight heating. The validity of using a material with higher permittivity is questionable due to the calibration fixture no longer representing an ordinary measurement environment. The raised permittivity between the conductor and RC windings will increase the capacitance, resulting in a lower bandwidth [21]. Since our RCs are going to be used primarily around large conductors, the capacitance is higher. The raised permittivity/capacitance for the calibration setup may then be valid.

For the TD measurement a small fixture was used to limit the amount of water required. The fixture has a length of 250 mm and metal sheet walls were added with a height of 130 mm. A small RC was made with a mean radius of 3 cm and is shown in fig.

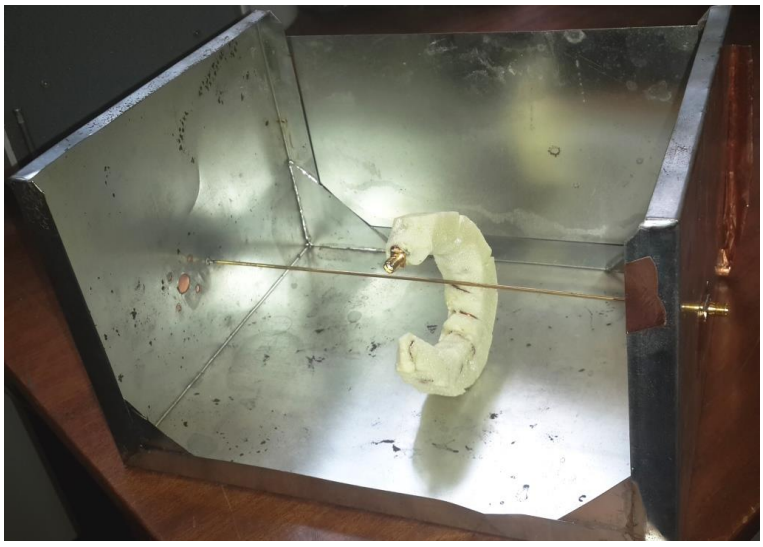

Figure 3.16: Small fixture (250 mm in length) used in the high permittivity experiment. Only one of the added walls is present. A newly fabricated RC was made with polyurethane foam to keep the permittivity of the dielectric between the windings close to 1.

3.16 in the fixture that was used. The RC is filled with polyurethane foam to keep water out between the windings and return windings. The polyurethane foam was measured in-house (with thanks to Dr. Andriambeloson) and showed a permittivity close to that of air ($\epsilon_r \approx 1$).

Shown in fig. 3.17 is the reflection coefficient of the fixture with the added higher permittivity dielectric (water). The gated mismatch response is also shown, along with the RC line effect. Since the frequency content above 1.5 GHz of the gated mismatch response is more or less the same as the original ungated signal, the conclusion is made that all the high frequency content of the pulse is reflected back at the mismatch. Since the high frequency content does not contribute meaningfully to the experiment, it can be excluded. When this is done, insight is not increased.

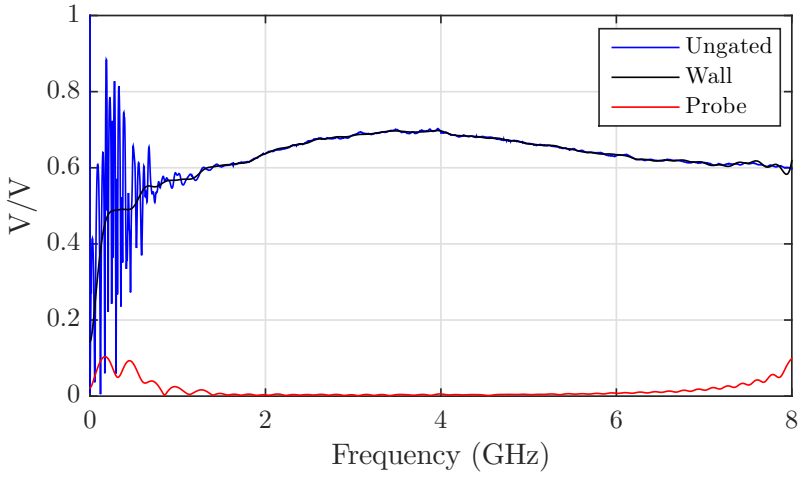

Figure 3.17: Reflection coefficient of water experiment.

The high permittivity setup was also simulated and results correlated with measure-

ments i.e. there is a capacitive step/short response at t=0.1 ns (fig. 3.18). It is believed that this capacitive step is the product of the extreme discontinuity in ground planes. Using water as a higher permittivity dielectric, the capacitance between a line and ground plane (eq. 3.4.1) is increased by a factor of 81, the relative permittivity of distilled water. It was attempted to improve the discontinuity in simulation, but was abandoned when meaningful results could not be obtained fast enough.

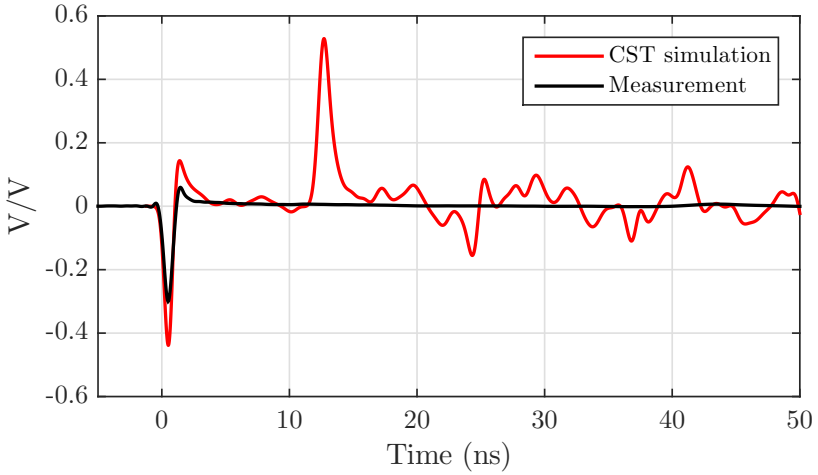

Figure 3.18: TD fixture reflection coefficient of water experiment. The secondary wall reflection is expected at 15 ns.

$$C = \frac{2\pi\epsilon_0\epsilon_r}{\operatorname{arccosh}(\frac{D}{d})} \tag{3.4.1}$$

With most if not all of the high frequency content contained within the first reflection, dispersion does not seem to explain the unexpected response. If the permittivity measurement shown in fig. 2.18 is to be trusted, content up to at least 2 GHz should be valid. However, this is not the case. We see abnormal behaviour beyond 700 MHz (fig. 3.17). A better explanation would be that the mismatch should be described as a high frequency short. The decision was made to discard any further attempt into using a higher permittivity liquid for matching purposes.

3.4.2 Physical attributes

After the permittivity experiments delivered inconclusive results, the physical attributes of the fixture were examined. Matching can be improved by altering any one (or all) of three variables, namely the conductor diameter, its height above ground and the number of ground planes for the fixture. The effects of the first two alterations can be explained using eq. 3.3.1. The variables are also present in eq. 3.4.2 [41] and table 3.2, which describes the characteristic impedance of a wire above a L or U-type ground-plane. The three different transmission lines are visualised in fig. 3.19. Figure 3.20 shows the difference in characteristic impedance for the three types of ground planes explored [41].

$$Z_O = \frac{1}{4\pi}\sqrt{\frac{\mu_o\mu_r}{\epsilon_o\epsilon_r}}\ln(1+\frac{s^2}{2}(S^2-1)) + \sqrt{(\frac{s^2}{2}(S^2-1))^2 + c(S^2-1)} \tag{3.4.2}$$

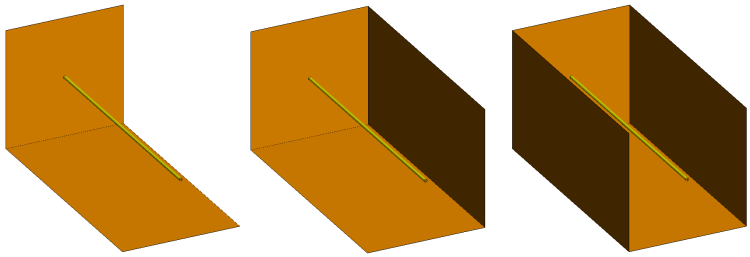

Figure 3.19: Transmission line with varying ground planes. Shown left to right is a single ground plane, two ground planes and three ground planes

Variable/fixture	L-type	U-type
S	$\frac{D}{d}$	$\frac{D}{d}$
s	$\sqrt{2}$	$\frac{4}{\pi}tanh(\frac{\pi}{2})$
c	1	$\frac{4}{9}$

Table 3.2: Variables for eq. 3.4.2

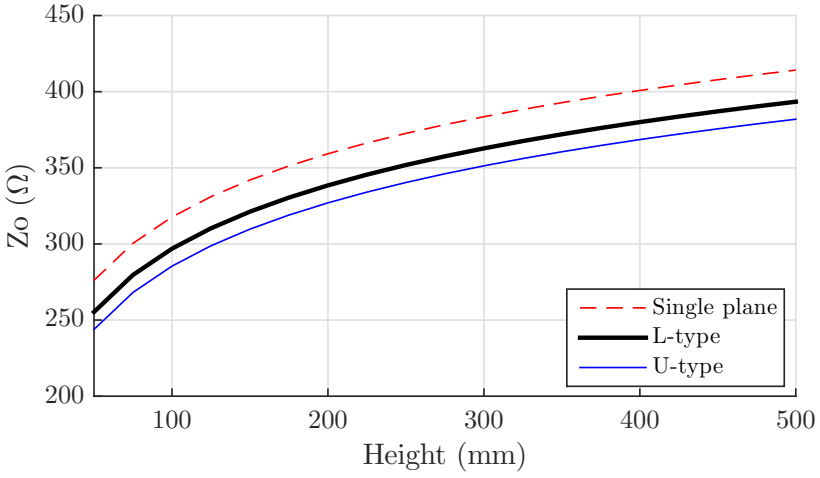

Figure 3.20: Comparison of characteristic impedance for a conductor above ground plane(s). Equations 3.3.1 and 3.4.2 were used where the height above the planes was varied.

3.4.2.1 Optimisation through simulation

Simulations were done to show that the theory holds true. During the optimisation process, only frequency content up to 1 GHz was included to ensure short simulation time. However, the low bandwidth simulation essentially hides short-wavelength detail, as was discovered in full-bandwidth measurements. Figure 3.21 shows the simulation setup along with dimensions used in eq. 3.3.1. The calibration fixture was simulated with an open end to save computation time and is valid since the reflections will be gated out in the TD. A small RC was included in the simulation and its effect on line impedance becomes more noticeable with increased fixture conductor thickness (6 ns in fig. 3.22a). Shown in this figure is the reflection coefficient from port one of the calibration fixture. As predicted by theory, the mismatch will decrease as the characteristic line impedance lowers towards the measurement impedance (50Ω).

The matching transition was also slightly optimised from the first angle of 41°. This

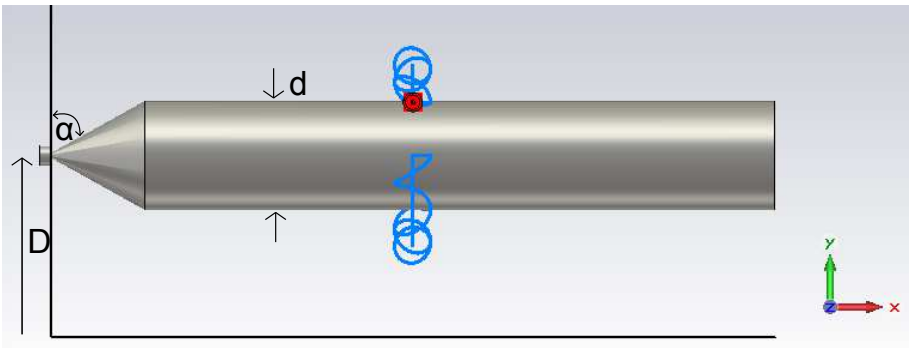

Figure 3.21: Setup in CST in which the angle α and the diameter d was varied.

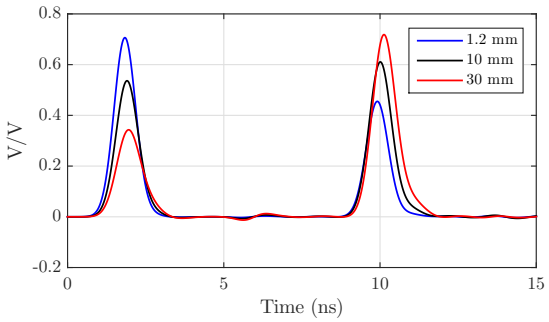

(a) Conductor diameter (D) simulations, α=60°

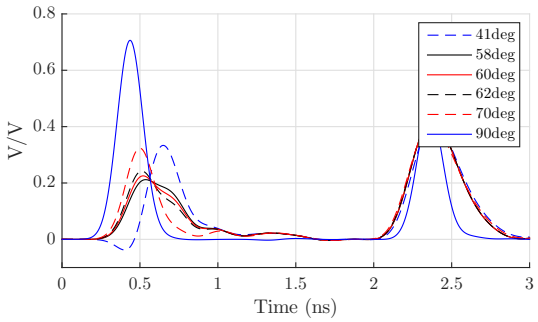

(b) Transition angle (α) simulations

Figure 3.22: Reflection coefficients of initial simulations done in CST. The best angle to use is 60° while the diameter is constrained by the current probe (30 mm)

angle stems from suggestion in [42] where 41° was the optimal angle for a conical antenna design. Other angles were tested and as seen in fig. 3.22b the best transition angle is 60°. While marginally better matching is possible, the effort required would not justify the gain in smaller reflection.

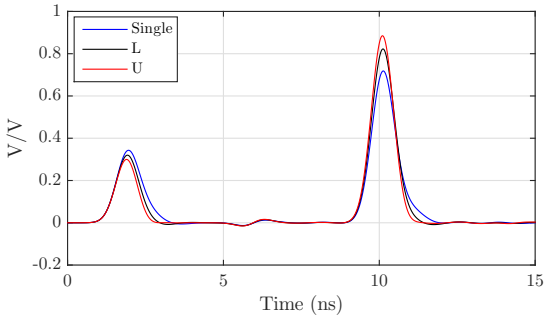

(a) Fixture reflection coefficient

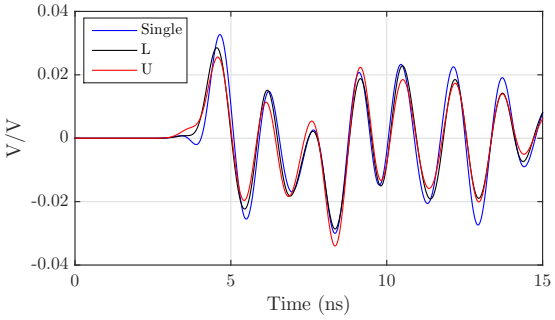

(b) Probe response

Figure 3.23: Reflection and transmission coefficients of simulations when adding additional ground planes. The first reflection is reduced, but the induced signal in the probe will be lower.

The case for added ground planes was simulated for interest. The reflection coefficient lowered as expected (fig. 3.23a), but the transmission coefficient from the fixture to probe decreased (fig. 3.23b). This might be due to the added capacitance to ground. Since the

difference in reflection coefficient was not significant enough, the addition of ground planes was not studied further.

3.4.2.2 Implementation

Two pairs of matching pieces with angles 41° and 60° were fabricated by our Centre for Electronic Services. Fig. 3.24 shows the matching pieces along with the larger conductor. The conductor consists of a perspex tube that is coated with conductive tape. Previously used SMA connectors had to be changed to N-type connectors to support the weight of the new conductor.

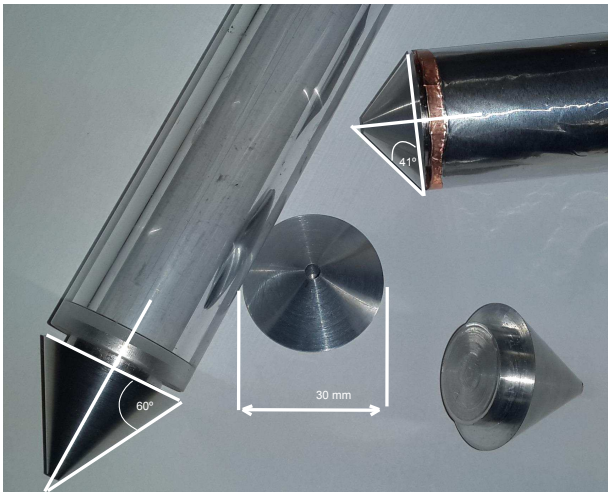

Figure 3.24: Aluminium matching pieces for new increased diameter conductor. Shown is two sets of matching pieces of profiles 41° and 60°. The new conductor diameter is 30 mm.

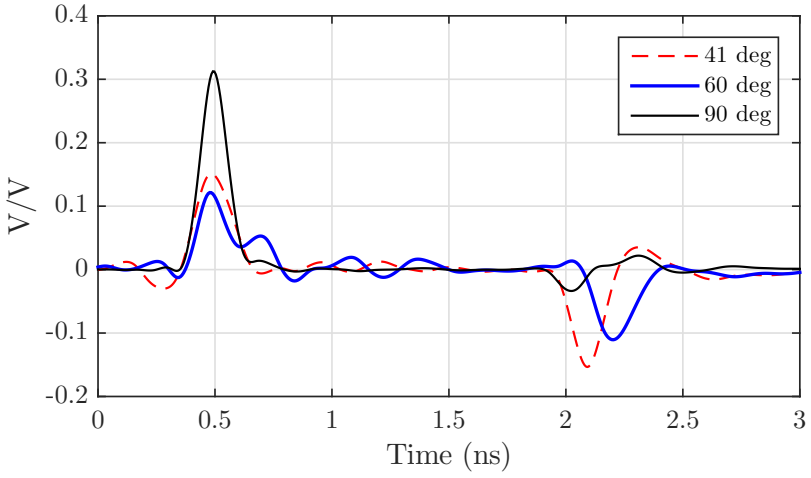

Figure 3.25: TD reflection coefficient measurements of of 90° (straight), 41° and 60° matches.

Shown in fig. 3.25 is the reflection coefficient of the different profiles. When first measured with the full-bandwidth setup (0-8GHz), the short-wavelength detail appeared. At t=0.35 ns in fig. 3.24, the first reflection is present and smaller in amplitude, but

220 ps later, a second peak is present. This is due to the created transition mismatch which stops rather abruptly and can be related back the length of the path travelled. The incline length of the matching piece is l and since the signal travels this distance twice (reflection), the time between the two observed pulses Δt will be governed by :

$$\Delta t = \frac{2l}{c} \tag{3.4.3}$$

Thus, a Δt of 188.8 ps (fig. 3.26) will correspond to an path length of 28.3 mm, which is close to the incline length of 26 mm in fig. 3.24. The difference between early simulations, optimisation results and first measurements can be ascribed to the lack of high frequency content in the simulations.

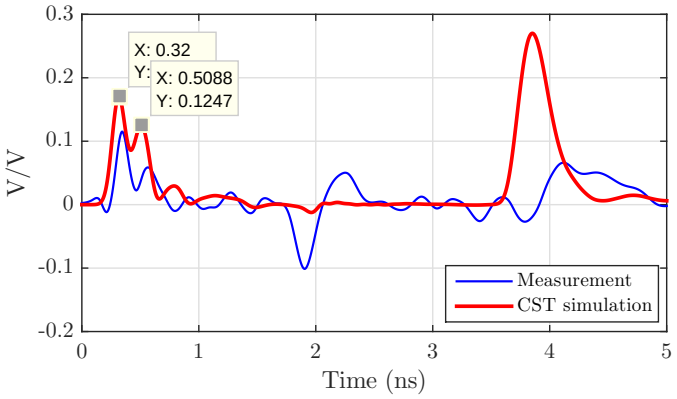

Figure 3.26: Reflection coefficient measurement of the 60° taper and 30 mm centre conductor, 50 mm above ground. A simulation is included with frequency content up to 7 GHz.

While the reflection coefficient is decreased by a considerable amount, a new issue presents itself in terms of settling time. The added discontinuity gives rise to the existence of small reflections between the wall mismatch and the transition mismatch. This can be observed in both simulation and measurement level (fig. 3.26). This will cause extra difficulty in identifying the correct response and/or effect from the probe (frame B in fig. 3.27).

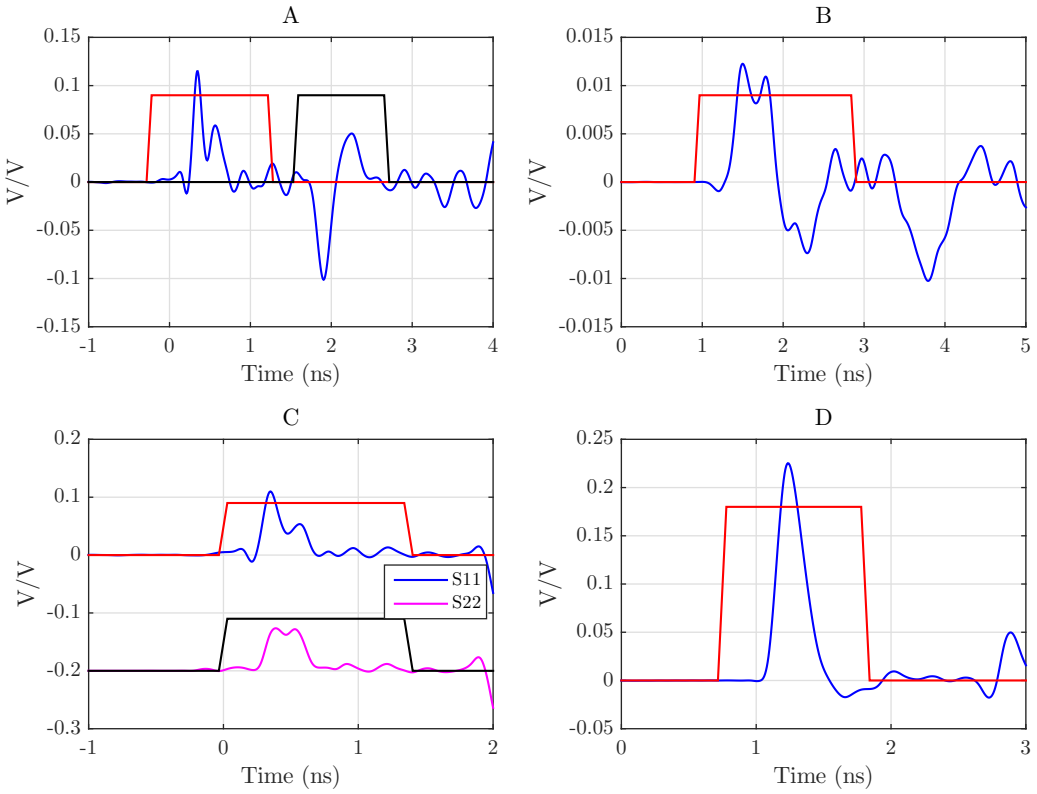

Figure 3.27: Time signals for the matching experiment; A. fixture mismatch and probe effect on line, B. induced probe response, C. half fixture mismatch and D. half fixture through measurement. A decrease in reflection coefficient is achieved, but at the cost of increased sub-reflections and settling time.

Applying the correction factors and transforms, the Z_t in fig. 3.28 is obtained. Also included is the Z_t for a raised conductor, capable of accompanying the large RC. Differences can be explained by the perturbing of the connector to conductor connections. Appendix *A* contains corresponding FD and TD figures of the ungated and gated signals for both normal (2mm) and enlarged (30 mm) conductor. Shown in fig. A.5 and A.6 is the fixture reflection coefficient and calibration of the ETS CP when the conductor height is 50 mm and 130 mm, respectively.

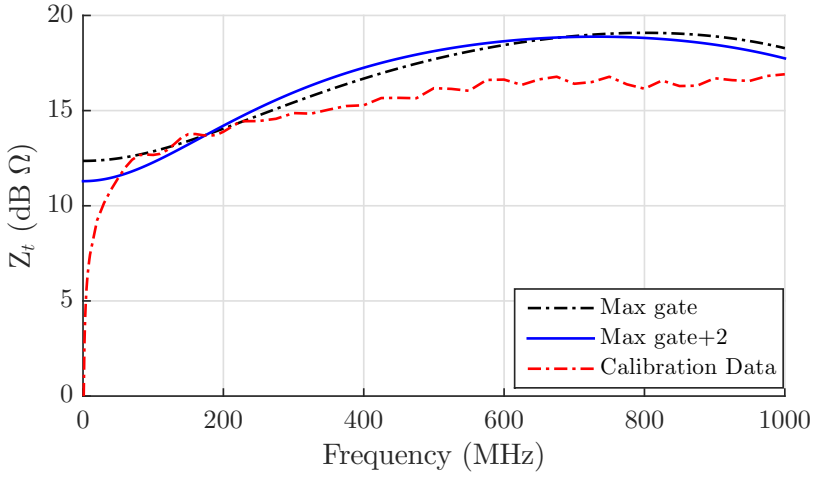

Figure 3.28: Z_t for the ETS CP with the new conductor. Different conductor heights and gate lengths results in very noticeable Z_t changes.

One possible downside to increasing the conductor diameter is that the capacitance to the closest windings of the RC will be increased as well. Depending on the application in which the RC will be used, this aspect may rather be an advantage. For current measurements around large antenna struts this tends to be the case.

3.5 Conclusion

This chapter has delivered interesting results that verified theory and served as reminder that care should be taken when planning measurements. The FD approach was verified with the ETS probe and deviation from the probe calibration data was below 3 dB up to 130 MHz. However, the RC is sensitive to placement position and care should be taken to eliminate offsets. It was found that the TD approach can adequately characterise a CP if the low cut-off frequency is high and the fixture long enough. For CPs with a very low low-frequency cut-off, the TD approach will result in inaccurate low frequency performance. Here the hybrid method successfully combines the best results from both methods.

While a smaller reflection was achieved through the use of a better matched transmission line, the presence of sub-reflections resulted in increased settling time which makes the gating process difficult. The experiment on matching through the use of a high permittivity dielectric gave inconclusive results. Better results could be achieved when using a perfectly characterised medium, but require more effort than can be justified when other methods are proven.

Chapter 4

Results and discussion

Both the FD and TD approaches could be verified with the commercial CPs. However, since no de-embedding is applied, the FD approach is inaccurate at frequencies higher than 130 MHz when calibrating in the large fixture (fig. 3.8). By contrast, full de-embedding is applied in the TD approach. The large RC was calibrated in the TD with both a small and large diameter fixture conductor. This chapter will discuss the results obtained for the large RC along with deliberating the RC and calibration methods. An application of the RC is presented at the end of the chapter and it too is discussed. A bandwidth test is also done to test the calibration of the large RC.

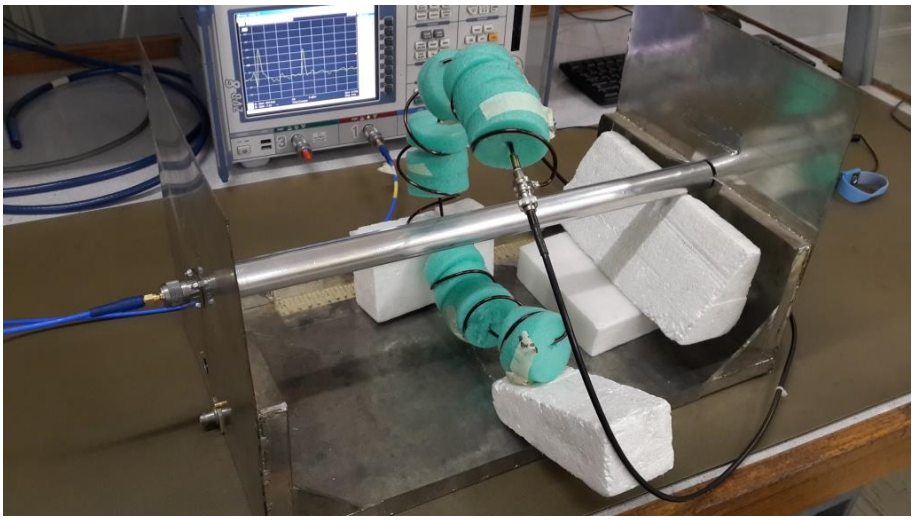

Figure 4.1: Large RC in 500 mm fixture with the conductor with increased diameter.

4.1 Large RC calibration results

Good results were obtained with the FD approach. Results correlate over the lower frequencies (<100 MHz) for theory, simulation and measurement (fig. 3.2). The large RC was then calibrated in the fixture with an enlarged conductor, shown in fig. 4.1. For the TD approach the transfer impedance differs substantially when compared to the FD approach. Figure 4.2 shows the transfer impedance for the FD and TD approach. For the TD approach three results are included; the base measurement where a 1 mm conductor

was used, the measurement where the conductors' diameter is increased from 1 mm to 30 mm (section 3.4.2), and a measurement where the fixture length is increased to 1016 mm.

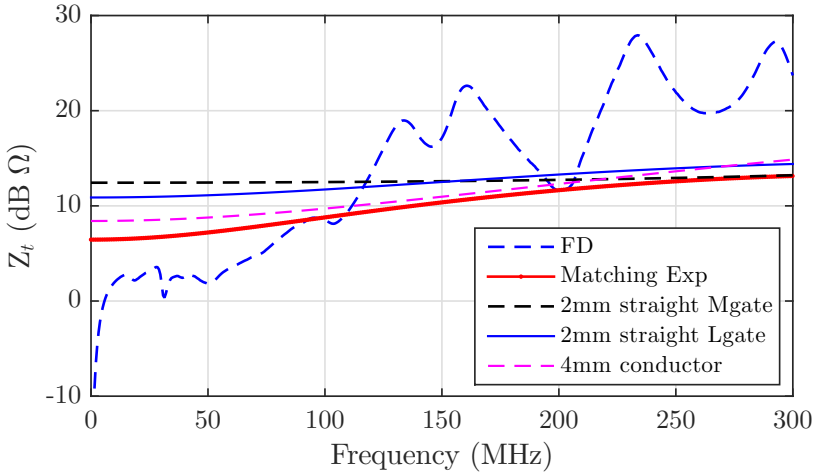

Figure 4.2: Z_t of large RC acquired through TD and FD approach. Included is the FD results along with the TD results for the matching experiment and an experiment where a 2 mm and 4 mm conductor is used. For the 2 mm conductor, the gate-length was shortened with 2 samples (2mm straight Mgate) from the maximum gate-length (2mm straight Lgate).

Since the measurements cover low frequencies (<300 MHz), the discrepancies might be due to the TD, i.e. inaccurate at low frequencies. The 1016 mm measurement should be more correct then. The gate length was also varied to evaluate the possibility of early reflections from the secondary being present. This resulted in the different results as shown in fig. 4.2. Shown in fig. 4.3 is the S_{21} TD response recorded from the probe when calibrated with the enlarged fixture conductor. It is difficult to establish where to end the gate since it might end on the start of an induced response from the second wall reflection.

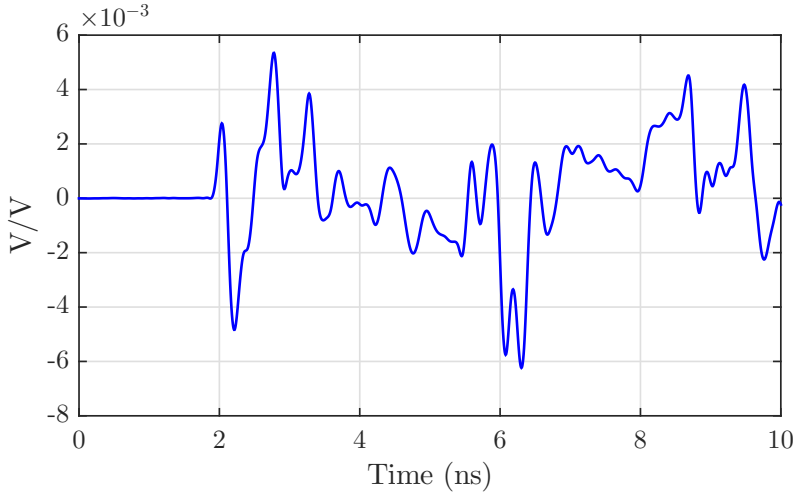

Figure 4.3: Induced signal in the large RC. The maximum allowable gate length is 3.3 ns. The difference that 2 samples make can be seen in fig. 4.2.

4.2 Rogowski coils

The Rogowski coil is a powerful, versatile transducer that has the potential to be used in a wide range of alternating current measurement applications. However, with the intended use for non stationary measurements, inaccurate measurements can be made if a calibrated device is used without care, or if used in an environment which could seemingly alter the calibration characteristics. For EMC type applications the RC should be accompanied by an electrostatic shield to promote disturbance rejection. However, a compromise will have to be made since this will decrease the bandwidth of the device. Moreover, if reasonable care is taken with the measurement setup, the large RC can be used up to 90 MHz. This conclusion can be made when looking at the bandwidth test. Should a measurement setup be present where uncertainty in placement is involved, fig. 4.4 can be used to define a cut-off frequency. In this figure the RC was moved closer to the fixture conductor to increase C_{ws}, while maintaining the same height above ground. Slight variation in Z_t can be seen in both measurement and simulation from very low frequencies. The author advises 100 MHz as the high-frequency cut-off for measurements with placement uncertainty.

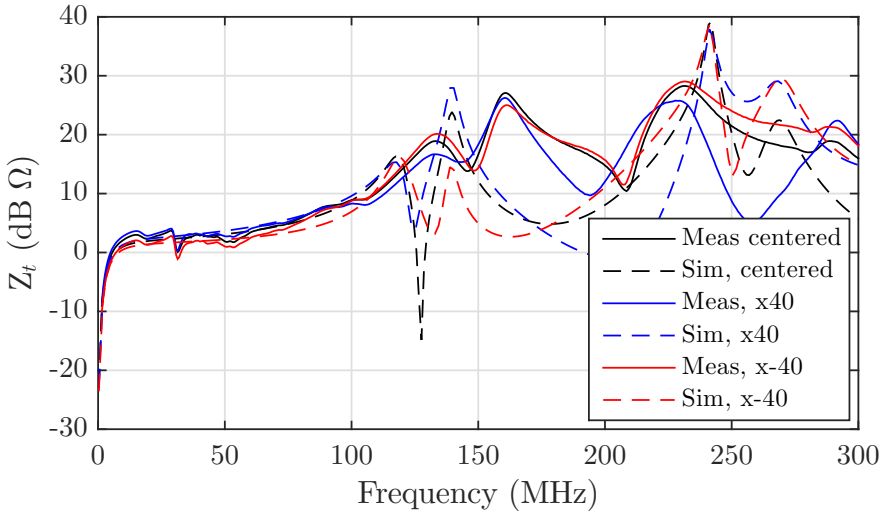

Figure 4.4: Simulation and measurement results of the effect an increase in capacitance has on the Z_t of large RCs. The RC is moved 40 mm forward (x40) and backwards (x-40) in the fixture and compared to centred position.

Experiments concerning conductor height were also conducted to test capacitance to ground. The measurements was accompanied by simulations, performed in FEKO. In fig. 4.5 the results are shown when the conductor height above ground plane and RC is increased with 40 mm. In the measurement result, only significant variation in Z_t can be observed after 100 MHz.

An application where RCs are widely used is the partial discharge measurement application. The RC is usually stationary and calibrated in its intended position of use. Thus, a very accurate and reliable measurement system can be conceived. However, this study was not focused on the particular application and the disadvantages and challenges are not investigated.

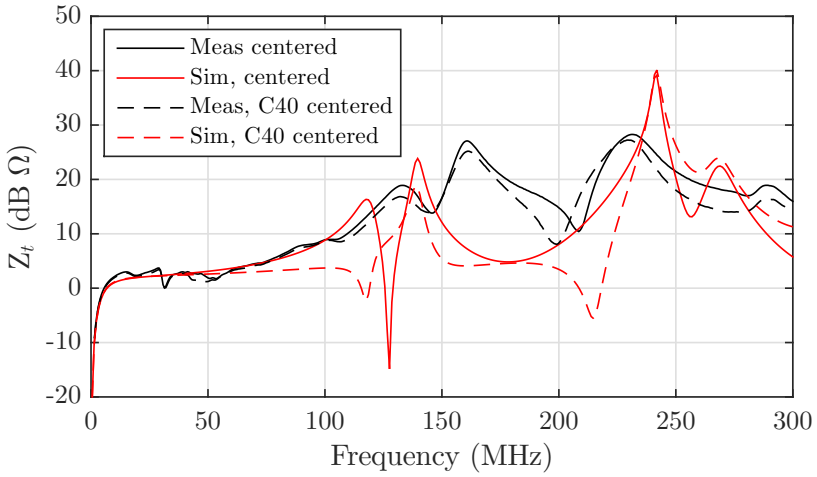

Figure 4.5: Ground effects on Z_t. In this measurement and simulation setup, the conductor height was increased 40 mm. For both cases (centered and C40) the RC is centered around the conductor i.e. the RC is moved with the conductor.

4.3 FD discussion

The FD approach was the initial method used to characterise CPs. This method delivered good results for an enlarged fixture over the lower frequency region (<100 MHz in fig. 3.2) and complies with the description of CISPR (fig. 2.14). However, literature covering FD de-embedding was only discovered towards the end of the project. Due to the lack of time, it was not implemented.

4.4 TD Discussion

The TD approach was attempted in an effort to extend the bandwidth of the calibration. On closer inspection the applied approach coincides with the full FD de-embedding employed by [36]. Their first step is to define S-parameters for the half systems. This allows them to account for junction reflections, essentially what is done in our gating process. We correct for the first reflection due to mismatch. They also use the actual current present at the measurement plane - another step that coincides with our approach. By gating out the reflections and focussing on the probe response, our measurement is void of backward travelling currents.

By gating the signals, unwanted reflections are eliminated and a matched end junction is created. In the mentioned literature the de-embedding is incorporated in defining S-parameters for the half systems. In our approach, each signal of interest is de-embedded with the appropriate reflection of similar interest. These reflections are acquired from an actual half-length fixture i.e. our approach requires two physically identical fixtures, only differing in length.

If these two approaches lead to (presumably) the same Z_t, a valid question arises : Do we need a TD approach? The usefulness of the TD method lies in its clarity. Examining the de-embedding equations (eq. 3.3.3-3.3.6), one can see that the signal of interest is corrected for reflections. This is not the case for de-embedding processes in the mentioned literature where the junction mismatches are described by a S-parameter model. Thus, our approach is more intuitive.

The TD approach also delivers highly repeatable results. Shown in fig. 4.6 are calibration results for the Fischer probe. For the case of the longest fixture (1016 mm), changes were made in the conductor diameter and the height above ground plane.

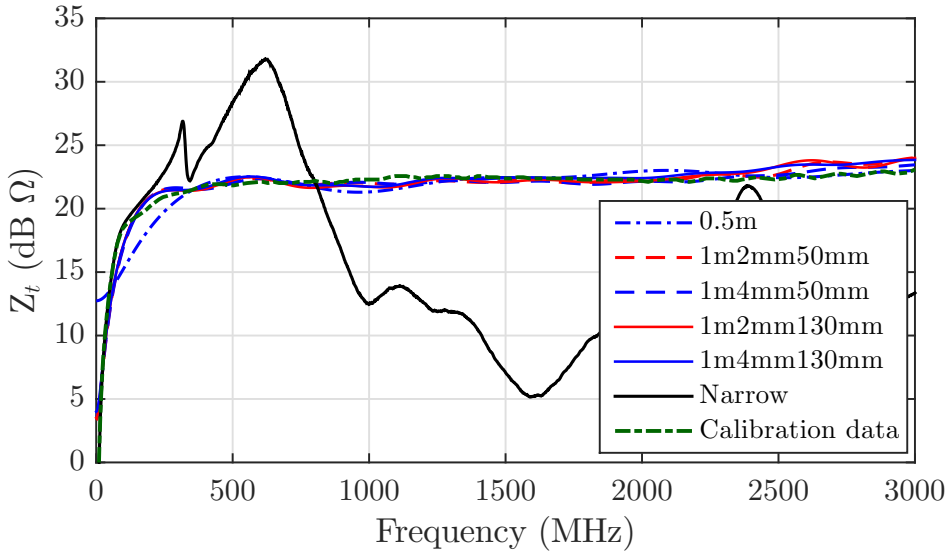

Figure 4.6: Z_t of the Fischer CP. The measurements are repeatable. For the TD measurements two conductor diameters were used (2 mm and 4 mm) and heights of 50 mm and 130 mm were also used. During these measurements the fixture was perturbed when soldering new conductors. Included is the FD measurement in a narrow fixture (B in fig. 3.9).

4.4.1 Phase information

Usually CP manufacturers do not disclose phase information. An idea about what the phase should be can be formed though. Since CPs are inductive devices, we expect positive phase at low frequencies. The phase should decrease as other frequency dependent components start to dominate. For ferrite CPs this might be the ferrite itself, having a frequency dependant μ_r which may only be defined at lower frequencies. For RCs, the capacitance however it is defined, will dominate at some point. This can be seen in our theoretical model along with the simulation and measurement - fig. 3.2. While slight variation is present, the theoretical, simulated and measured phase in fig. 3.2 agree very good up to 10 MHz. After 10 MHz, the measurement starts to deviate and differs 25° at 100 MHz.

The phase can also be recovered for the CPs. Unfortunately it can not be validated against a known value. Shown in fig. 4.7 are results for the ETS CP. The de-embedded TD calibration approach in the 1016 mm fixture is also included, but differs substantially at high and very low frequencies. The low frequency deviation can be ascribed to the inaccuracies in the TD approach.

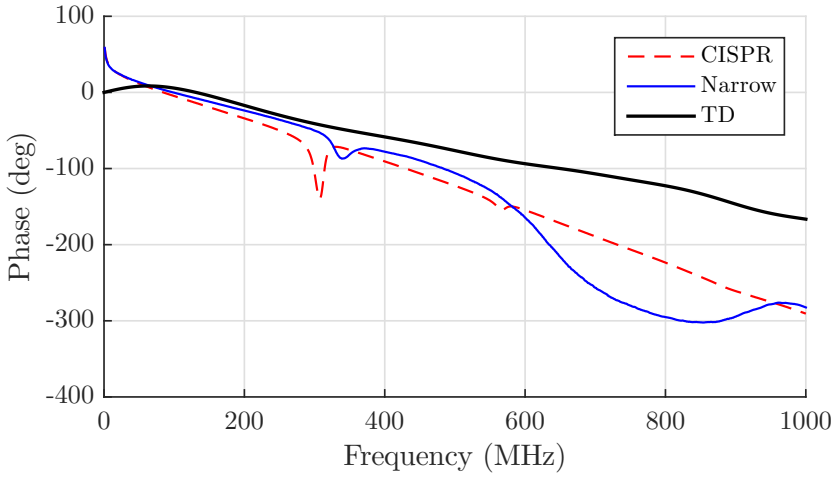

Figure 4.7: Unwrapped phase of the Z_t for the ETS probe. Measurements were made in a CISPR, narrow U-type and 1016 mm TD fixture. Except for the resonance at 320 MHz the CISPR type fixture delivered the best results.

For the Fischer probe the results of the phase are inconclusive. When complex values are used in eq. 3.3.8, unreliable phase along with a region of error (500 MHz - 2250 MHz) in the magnitude of the transfer impedance are obtained. This is shown in fig 4.8. A possible explanation for these results may be that the TD approach is a magnitude-only approach. In the analysing stage, the signals must be corrected for certain reflections, only observed from a magnitude perspective.

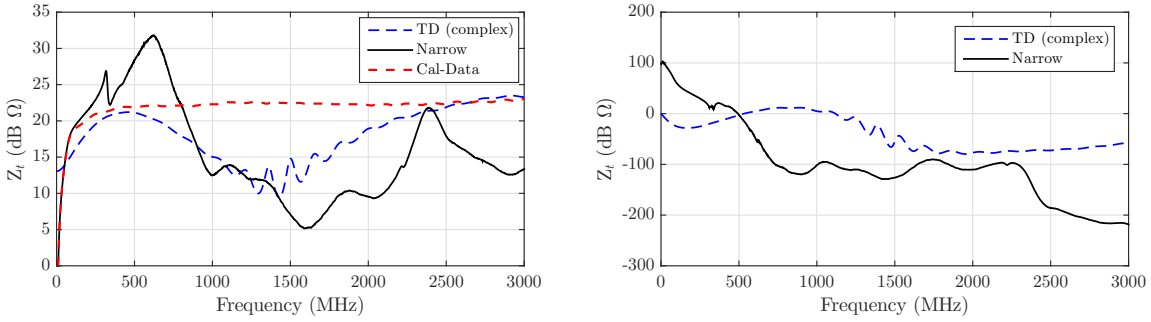

(a) Z_t (b) Phase

Figure 4.8: Z_t and phase of the Fischer CP when complex values are used in eq. 3.3.8. The FD results for the Fischer CP in the narrow fixture are also included.

4.4.2 Settling time

It is found that the TD approach is only inaccurate when using current probes that have very low frequency response. Figure 4.9 shows the difference in induced signal for the ETS CP and Fischer CP. For the Fischer probe, the signal has mostly settled before the reflected current arrives (t=5.8 ns) but for the ETS probe, ripple is still present. If a sufficiently narrow pulse is used, then only an increase in fixture length can improve the low frequency performance. Using a longer fixture will allow for more of the long time constant to be recorded.

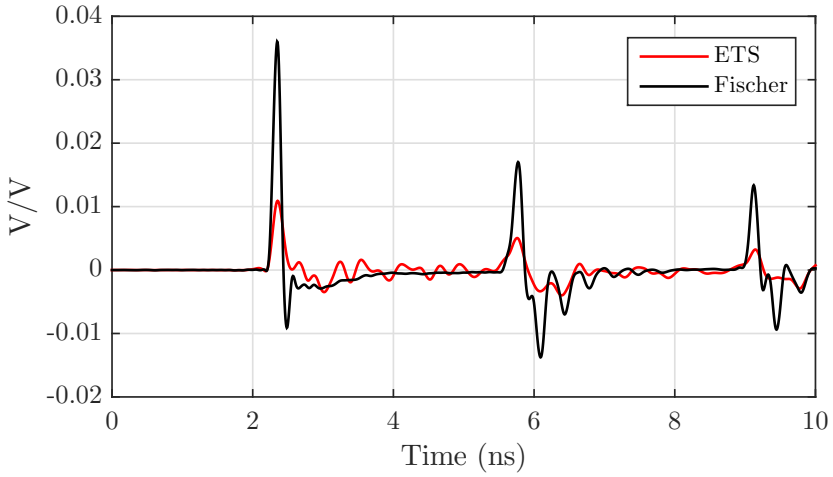

Figure 4.9: Probe response of the ETS and Fischer CPs in a 1 m fixture. The reflected current is present at 5.8 ns.

Since only one CP with a high low-frequency cut-off was present, it is difficult to provide a quantifiable figure or rule of thumb. The period of a 10 MHz signal is 0.1 us, but we see that the signal is induced and has settled before a reflection arrives 3.33 ns later. For the Fischer CP then, the fixture is adequately long at a 30th of the wavelength of the low-frequency cut-off. This number lies between a tenth of the half and quarter wavelength. Using a 20th of the wavelength (a tenth of a half wavelength) will result in a longer fixture and is recommended to ensure the long time constant is recorded properly. However, if the hybrid approach is applied and both the FD and TD calibration results are used, settling time is not an issue if the FD approach results in the correct calibration. If this is the case, calibration results must be tested to find the upper limit of the bandwidth.

4.5 Bandwidth test

To test bandwidth of the RC, a comparative measurement is done. The 500 mm calibration fixture was used, but slightly modified. A 2 mm conductor is used and its end is soldered to the fixture wall. This conductor was then excited at selected frequencies with a 0 dBm signal, generated by the R&S SMLA 03 signal generator. A current will now flow on the conductor. Current measurements were taken with the ETS, Fischer CPs and large RC. The ETS probe was used in a course measurement where only selected frequencies were measured. The results are listed in table 4.1. The calibration certificates were used for the CPs whereas the FD calibration results were used for the case of the large RC. Low frequency signals (<40 MHz) were measured correctly and, depending on application, results with acceptable deviation (6 dBuA) are achieved up to 90 MHz. However, at 40 MHz a faulty measurement is suspected.

Measurement in dBuA				
Frequency (MHz)	ETS	Fischer	RC FD	Difference
1	74.43	-	74.6	0.17
10	70.56	70.88	71.57	0.69
20	68.97	68.87	69.26	0.39
30	69.55	69.55	69.78	0.23
40	-	67.86	78.97	11.11
50	66.55	66.96	72.97	6.01
60	-	64.53	70.16	5.63
70	-	62.89	67.63	4.74
80	61.14	61.05	65.17	4.12
90	-	59.36	64.1	4.74
100	-	58.56	66.73	8.17
110	-	58.08	68.66	10.58
120	59.47	57.83	67.17	9.34
130	-	58.71	66.04	7.33
140	-	58.95	69.57	10.62
150	56.74	57.55	64.55	7

Table 4.1: Results for the bandwidth test. All values other than the frequency column are in dBuA.

Shown in fig. 4.10 is the measurements and results, which is also listed in table 4.1. The TD calibration was also applied and included. The 20 MHz and 30 MHz discrepancies can be attributed to the transitional region used in the hybrid Z_t. Linear interpolation was used and resulted in too high values being assigned. For the higher frequencies the TD approach performs better.

Concerning the Fischer probe, the 1 MHz signal can not be corrected since no data is known for this frequency. If the signal is induced correctly, it is expected that the corrected value should lie close to the ETS probes' values.

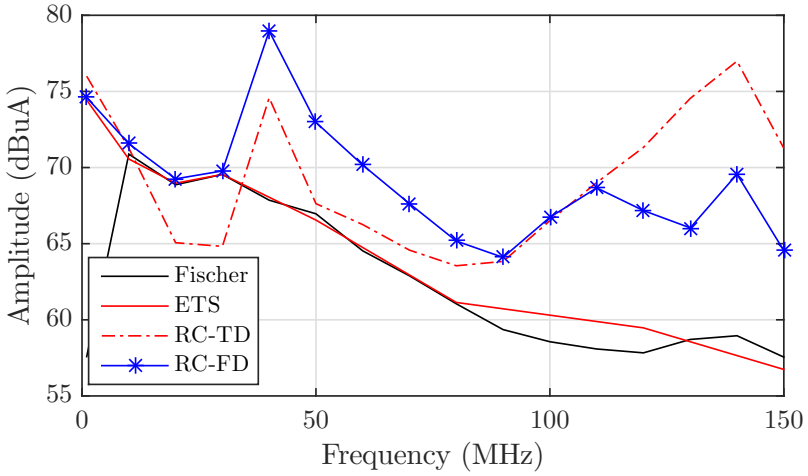

Figure 4.10: First comparative measurement between three probes. Inaccuracies below 80 MHz can be attributed to the transitional Z_t used.

4.6 On-site measurements

There is a carpenter's saying that goes 'measure twice, cut once'. In the field of metrology, we aim to only measure once, but this is not always possible. In most cases, precision measurements require time, which may not be a given. Another factor that is present is repeatability. Measurements are seldom repeated to show the methodology is correct and results are stable.

For our measurement campaigns a rigorous amount of planning was always present. Unfortunately unforeseen circumstances and the small amount of time warranted improvisations. While a controlled setup was always strived for, it quickly became evident that some sacrifices regarding accuracy would have to be made. While an antenna may be characterised in an anechoic chamber or open area test site, the user must always be conscious of the environmental influences. Thus, uncertainty will decrease maximum attainable precision. However, depending on the degree of accuracy, the new environment can be characterised and certainty over measurements can be established.

This was also experienced in the campaigns when attempting current measurements. The measurement environment changed and introduced new variables that must be accounted for. This raises the concern for validity if the measurement device can not account for the introduced unknowns. However, the calibrated device may not only be used in extreme circumstances. There may well be instances where the device will be used in suitable situations. Precision calibration then allows for a wide range of applications, extending the device's usefulness, driving down costs, which is one of the design criteria.

4.7 Simulated direct lightning measurement

For this degree we had the privilege to be able to conduct measurements on the first MeerKAT radio telescope (M63). This telescope was still partly under construction while studied but was operational at the end of February 2015. Two measurements (September 2014 and May 2015) were made with the first proving the measurement methodology was correct.

4.7.1 Methodology

The methodology followed is one suggested by [3] where a pulse is injected with adequate frequency content. A pulse generator (PG) was used to inject a current onto the structure through the ATR (fig. 4.11a). The current flows through the structure towards the earth connections. The current path was completed by connecting the PG earth to the pedestal earth via an earthing cable protruding the ground around the pedestal. This allowed for safer operation since access too the isolation transformer - which houses an earth reference point, but also high voltages - was not not required. The schematic setup is shown in fig. 4.12 and the PG setup and earthing connection is shown in fig. 4.11b. A battery and EMC-compliant battery-inverter power supply is used to avoid introducing other current paths to the measurement.

(a) Current injection onto the ATR.

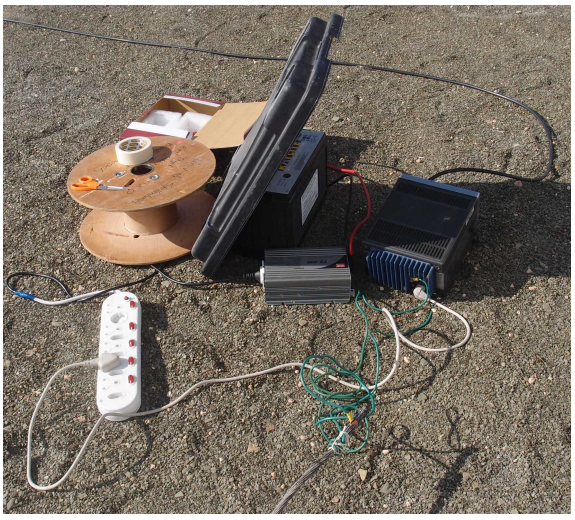

(b) The PG and power source: a 12 v battery and inverter.

Figure 4.11: Current injection point and PG setup. A battery powered setup is used to avoid the introduction of new current paths.

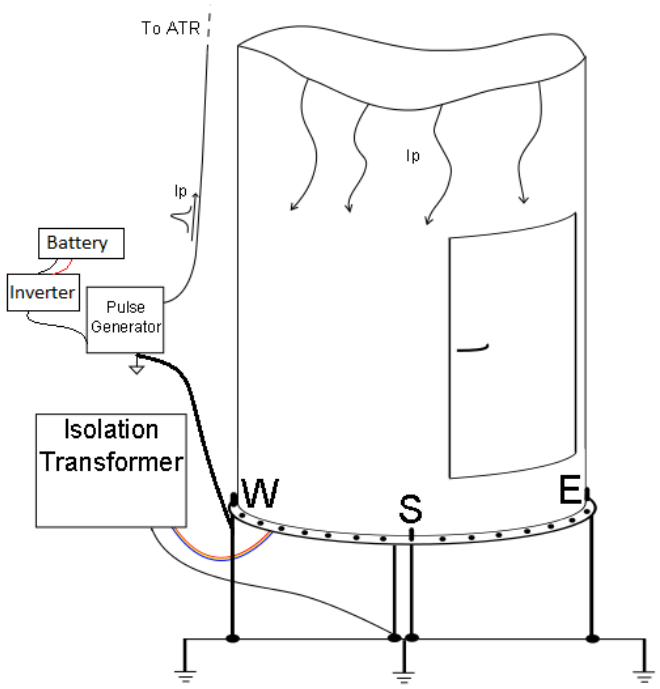

Figure 4.12: Pulse injection setup diagram. The pulse is injected onto the ATR and the return path is closed through the pedestal earth.

4.7.1.1 Safety

Before any testing equipment was switched on, safety measures were implemented. The two most notable were switching off the L-band receiver and covering it with a flexible reflective cover. Figure 4.13 shows the cover placed over the aperture of the receiver. After safety measures are implemented, the PG (fig. 4.11b) is switched on.

Figure 4.13: Safety measures to ensure that the L-band receiver is not damaged.

4.7.2 Pulse characteristics

For our tests on MeerKAT a Philips PM 5712 PG is used. The PG has a working bandwidth of 1 Hz to 50 MHz which is adequate for lightning type pulses. In fig. 4.14a the unloaded TD waveform is shown which was measured with the Yokogawa DLM 2052 oscilloscope. The frequency content was measured with a Rohde & Schwarz FSEK30 spectrum analyser and the spectra is shown in fig. 4.14b. Comparing the spectra to that of fig. 2.4, it can be seen that a similar envelope is present. The low frequency content dominates with gradual decreasing amplitude as frequency increases. Unfortunately the SANS model does not provide spectra detail beyond 10 MHz. The pulse was achieved with the settings for the PG listed in table 4.2.

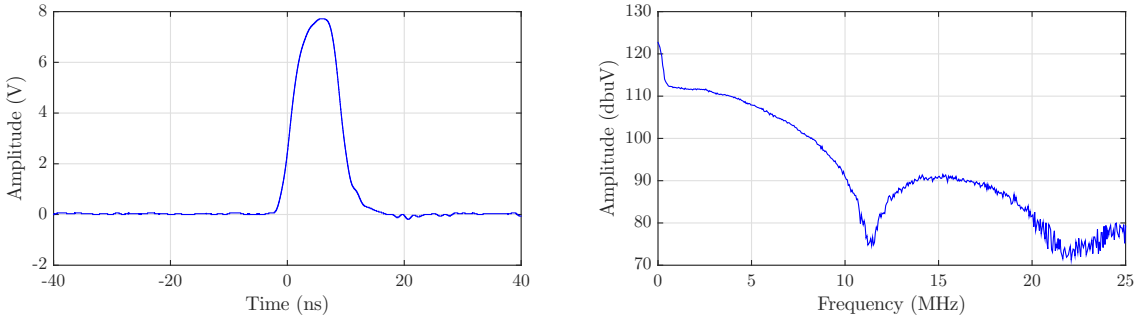

(a) Pulse waveform

(b) Pulse spectra

Figure 4.14: Waveform and spectra of the pulse injected onto M63.

4.7.3 Areas of interest

With the whole telescope being a potential conductor to ground for lightning, our interests concerned sensitive conductors such as mechanical interconnects. The entry point into the telescope system starts on an air termination rod (ATR). These rods are designed according to the equipotential sphere method ([3]). The ATRs are connected to the

Variable	Value
Amplitude	10 V
Rise time	4 ns
Duration	10 ns
Repetition time	10 us

Table 4.2: Settings for Philips PM 5712 Pulse generator

lightning down conductors (LDC) which safely guides most of the current to earth through the 1 Ω impedance to ground.

Between the entry and exit point of a supposed strike, various sensitive mechanical components are used. Figure 4.15 shows areas of interest with our main focus being the jack-screw and shoe-slip ring assembly (B and C in fig. 4.15). The jack-screw is of concern since it may provide a low impedance path for current to flow. In the event of excessive current, thermal heating may occur and damage components such as bearings. Shown in fig. 4.16a is a measurement made with the ETS probe and RC (insert) and in

Figure 4.15: M63 with circled areas of interest.

fig. 4.16b the respective measurement results are shown. Large differences can be seen between the two measurements. These differences can be ascribed to the close proximity of the windings and conductor and the surrounding metal objects which increases the

C_{ws}. The lift-basket could only carry one person. A hand-held spectrum-analyser was used and could not be operated while supporting the RC.

(a) Measurement made at jack-screw cabling.

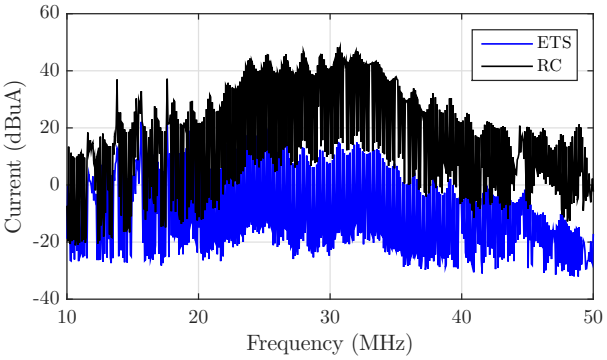

(b) Measurement comparison of ETS CP and RC.

Figure 4.16: Measurements made at the cables near the jack-screw assembly. Due to time constraints and limited ability, the RC could not be supported to reduce disturbances from the surrounding environment.

The shoe-slip ring assembly is considered since it houses earthing straps that provides a low impedance path to the lower part of the pedestal. Unfortunately the assembly was covered (fig. 4.17a), prohibiting access to the straps.

(a) Covers prohibiting access to the shoe-slip ring assembly.

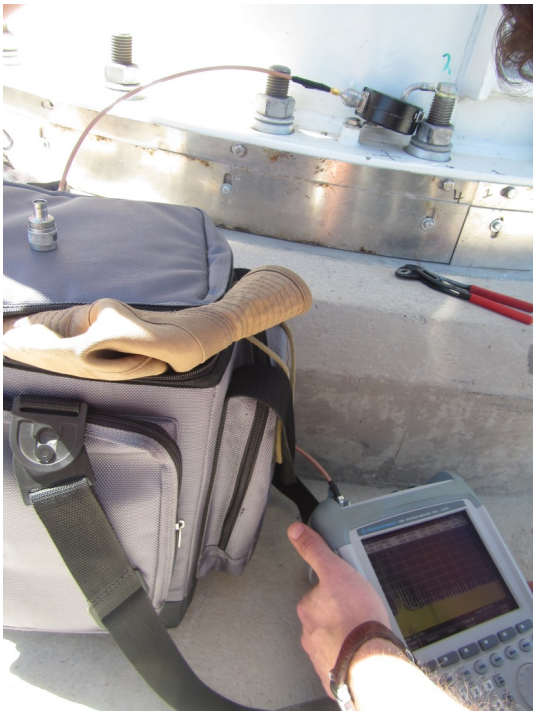

(b) Measurement at the Southern earth connection.

Figure 4.17: The covers protecting the shoe slip-ring assembly (a) and a measurement done at one of the pedestal earth connections.

The pedestal is secured to the foundation with 32 fastening bolts, of which four are directly connected to the main earthing structure embedded in the foundation. These bolts are covered by a face plate, thus prohibiting the opportunity to measure current on them directly. However, for each of the four earthing bolts, a lug-wire has been connected between the bolt-top and pedestal skirting. Figure 4.17b shows a measurement setup where a current probe is connected around the lug-wire. The figure also shows the face plate.

A possible entry point for lightning induced currents is the pedestal cable entry point called the stub-up. The stub-up provides the three-phase power needed for operation. A measurement was made of the power cable and is shown in fig. 4.18a. For this measurement a pulse was still injected onto the ATR. Figure 4.18b shows the results of the measurement. For comparison, the measurement was repeated with the ETS probe. Unfortunately the results do not show any agreement. As can be seen the in fig. 4.18b the RC is supported by the metal disc securing the stub-up. This disc influenced the measurement and could not be accounted for.

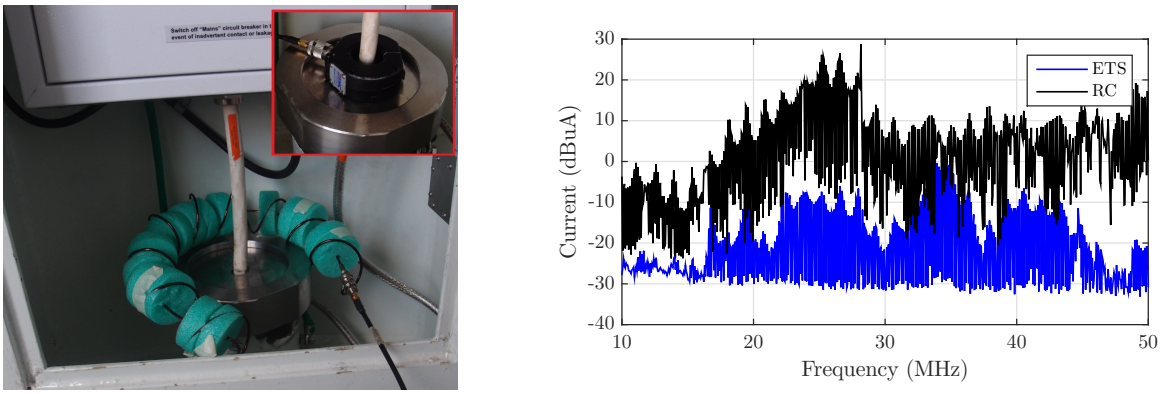

(a) Measurements at the stub-up connection. (b) Measurement comparison of ETS CP and RC

Figure 4.18: Measurements made at the stub-up. The RC was on the metal disc securing the stub-up and introduced disturbances to the RC.

4.8 Conclusion

This chapter has shown the results when the TD calibration approach is applied to large RCs. Due to the TD's inherent poor performance with very low frequencies, the calibration will have to be hybridised. However, the low frequency performance can be improved with longer fixtures. With a low-frequency cut-off of 10 MHz, the Fischer probe was sufficiently characterised and the TD approach is proven to be very repeatable. For practical on-site measurements care must be taken when taking measurements. It was seen that an unshielded RC is easily influenced by the surrounding environment which will lead to inaccurate measurements. The inclusion of an electrostatic shield will improve the rejection of disturbances, but bandwidth will be reduced. However, with a controlled setup, the bandwidth test has shown that an unshielded RC can be used up to 30 MHz.

Chapter 5

Conclusions, recommendations and future work

This project has delivered valuable insight into the fundamentals of Rogowski coils and current probe calibration. Two calibration approaches were verified with commercial CPs (Fischer CC F-2000 and ETS 94111-1L) and applied to a large RC.

It was seen that the FD calibration method is best suited for the lower frequency band. For large RCs in large fixtures, this method is currently restricted to frequencies lower than 130 MHz if a 3dB error is allowed. The restrictions are imposed by reflections which are present since de-embedding was not applied. For the larger fixture used with RC calibration, the conductor length is 200 mm which relates to a 1.5 GHz wavelength. Even if this length relates to a quarter wavelength frequency (374.7 MHz), the resonances and nulls are not explained through standing waves since these frequencies are much higher than frequencies considered for the measurements.

For higher frequencies, the TD approach is recommended. Both commercial CPs could be calibrated over their full bandwidth above 100 MHz. For this approach the Fischer probe delivered better results for low frequencies. When calibrated with a fixture twice as long, the full bandwidth (10 MHz -3 GHz) of the CP could be calibrated. This is due to lower frequencies not being induced as strongly as in the ETS probe, which results in a signal with a shorter time-constant that can be fully recorded before contaminated by the reflected current.

If the hybrid approach is applied, the transitional region must be revised. Linear interpolation resulted in too high values being assigned. To improve the transitional region, polynomial interpolation can be applied. The frequencies at which the transition region is applied may also be too low since the TD approach is inherently inaccurate at low frequencies.

The matching experiments provided results that correlated with theory. A smaller mismatch reflection was observed and an increase in signal magnitude was achieved in the probe response. However, the 60° matching profile between the 3 mm N-type pin and 30 mm conductor caused sub-reflections which contaminated the high frequency response induced in the probe.

Regarding the use of the RC for EMC related measurements, an electrostatic shield should be included. Without the shield, the RC can easily be influenced by the surrounding environment as was seen in the measurement results for the on-site measurements made on M63. Including an electrostatic shield will allow for better characterisation in theory and provide better repeatable measurements since disturbance rejection will be better. Moreover, a compromise will have to be made since the bandwidth will decrease

with the introduction of an electrostatic shield.

5.1 Recommendations and future work

While good correlation between theory, simulation and measurement were obtained for the FD approach below 100 MHz, it is recommended that this method be de-embedded according to the process in [36]. If the TD approach is preferred when calibration is done, it is suggested that the fixture length should be as long as possible. This stems from the results of the Fischer and ETS probes which showed better representation of the calibration data at lower frequencies using a 1m length fixture.

For the commercial probes both calibration methods deliver good results over their respective frequency bands. However, only the magnitude of the Z_t can be trusted. Future work should include calibration of the phase. Some phase information could be obtained from the FD approach when using the CISPR and narrow fixture. However,due to time-constraints the FD approach followed in this project was not fully de-embedded as described by [36]. The suggestion is made that the FD approach should incorporate de-embedding and evaluate if the phase from the de-embedded procedure is correct.

Concerning the TD, the approach can be refined to include phase information since it is currently only accurate when compensating for magnitudes of reflections. It might be insightful to compare the calibration methods covered in this project to those used in other applications, such as partial discharge.

To enhance the calibration method, the topic of matching should be considered again. Since the gating of reflections essentially mimics a perfectly matched system, it might be advantageous to have a matched system to begin with. This would then eliminate the need for gating the probe response as well since there is no secondary reflection to induce a response that might fall within the time span of the first induced response. However, matching might be difficult due to the fixture geometry which has a characteristic impedance of 271Ω for a 1 mm line, 5 cm above the ground plane. However, matching might be more time consuming when compared to the hybrid approach. To improve the hybrid approach, it is recommended that a) the transition frequency be higher since the TD approach is inaccurate at low frequencies and b) a better interpolation technique, e.g. polynomial interpolation, is used.

Further work on RCs could involve more rigorous bandwidth tests. The RCs are sensitive to capacitive disturbances if an electrostatic shield is not present. Tests could be devised for the presence of disturbances and accounting for possible diminishing effects it may have on the bandwidth.

Appendix A

Gating process

A.1 Straight conductor

Shown in fig. A.1 is the TD signals of interest. Observing frame *A*, the gate is applied at -0.3 to 0.4 ns. The isolated response is then transformed back to the FD, and the gated frequency response is shown in frame *A* of fig. A.2. In the TD, any responses that do not lie within the gate are excluded, resulting in the sole response of the signal in the gate. The same approach is applied to the other signals

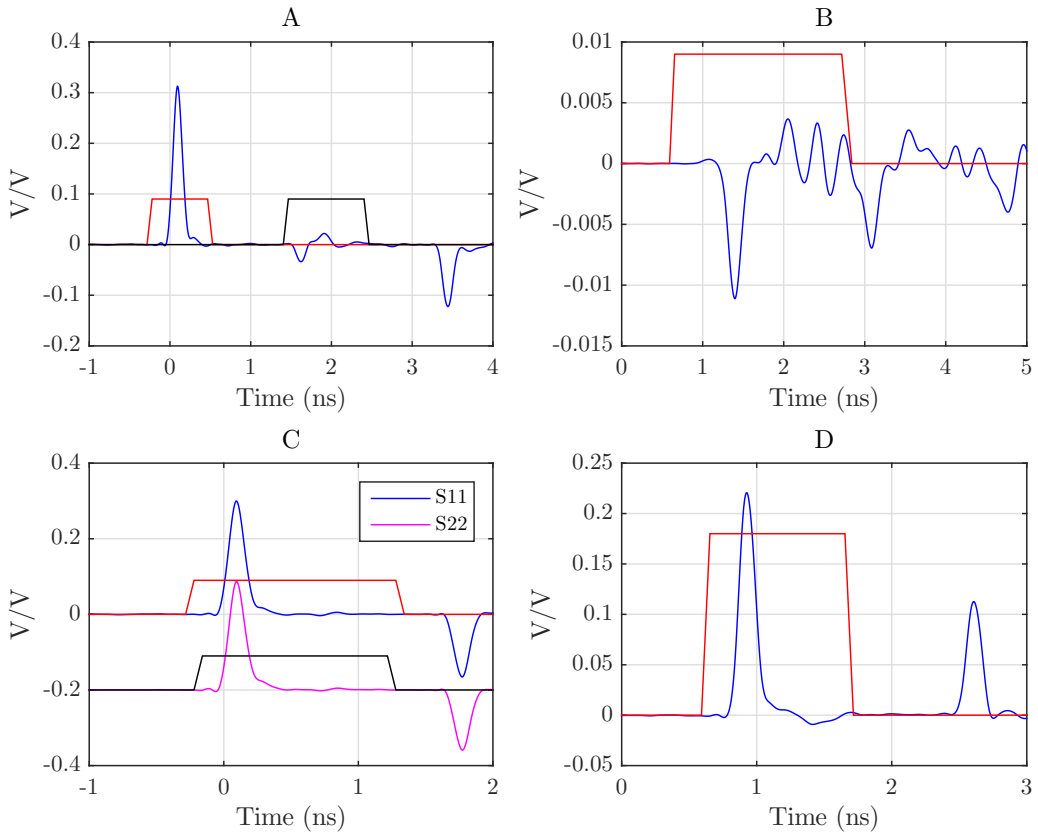

Figure A.1: Relevant time signals and their gates, used in gating process. A: Fixture reflection coefficient, B: Probe response (S_{21}), C: Half-fixture reflection coefficients, D: Half-fixture through measurement (S_{21}).

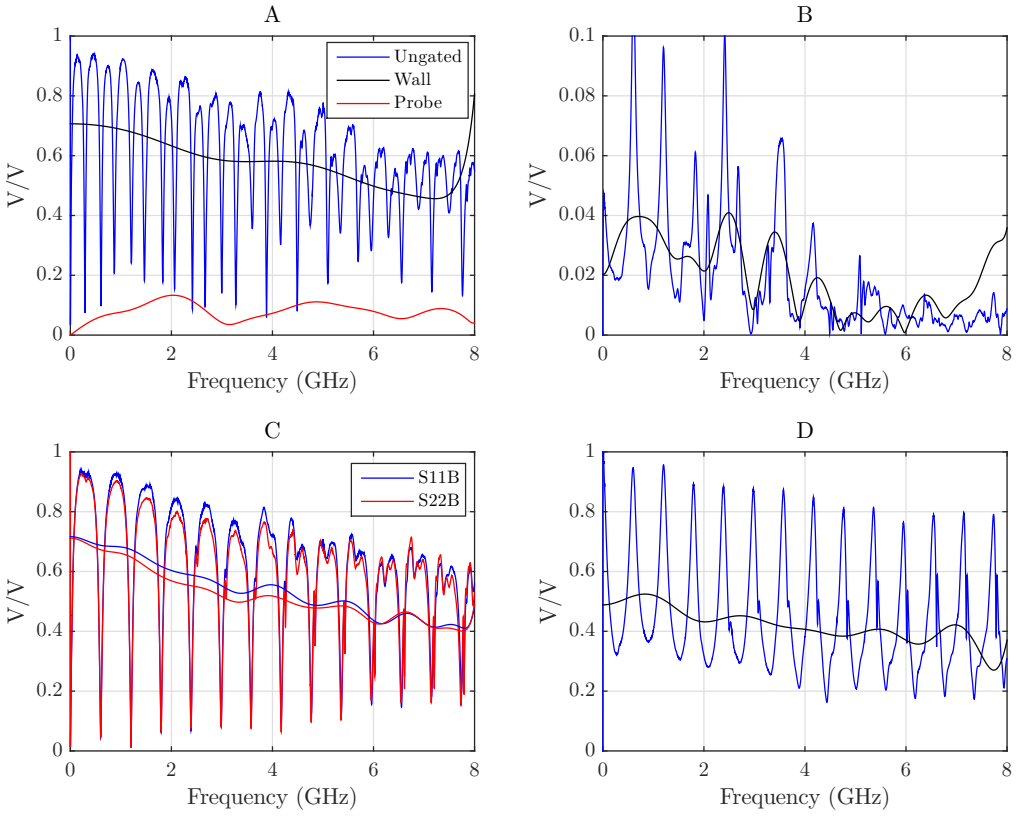

Figure A.2: FD signals, normal and gated. A: Fixture reflection coefficient, B: Probe response (S_{21}), C: Half-fixture reflection coefficients, D: Half-fixture through measurement (S_{21}).

A.2 Enlarged conductor results

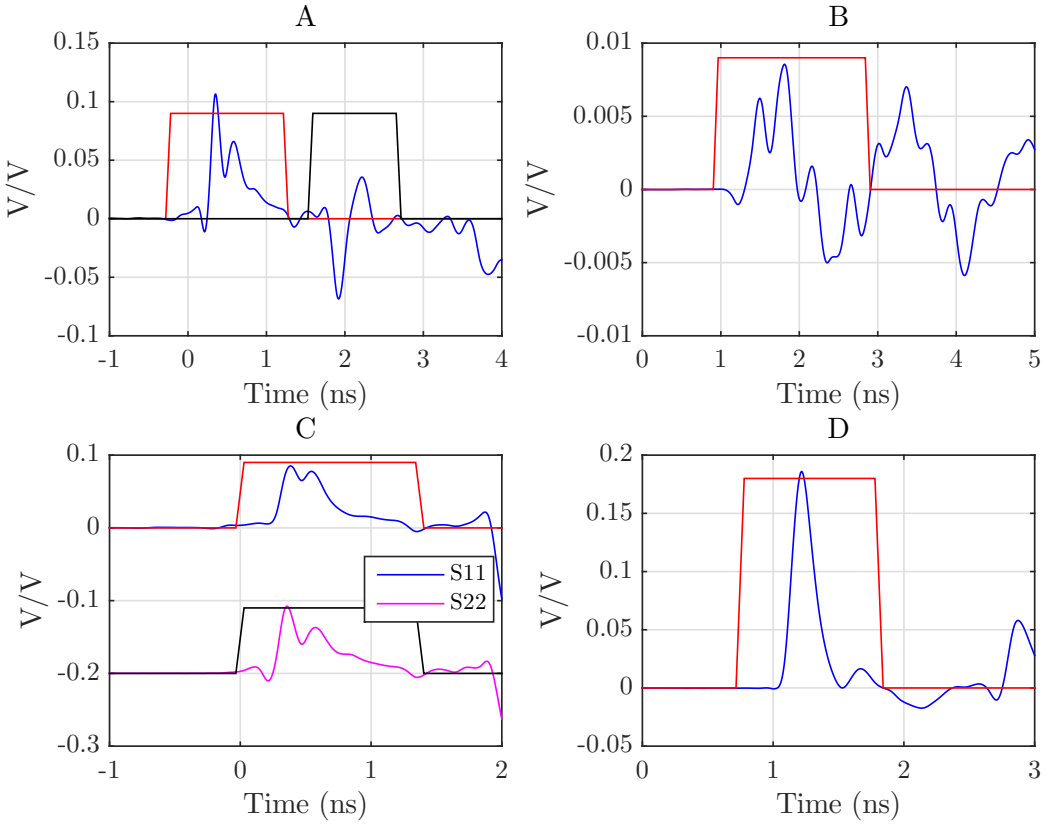

Figure A.3: TD signals for the enlarged conductor experiment. A: Fixture reflection coefficient, B: Probe response (S_{21}), C: Half-fixture reflection coefficients, D: Half-fixture through measurement (S_{21}).

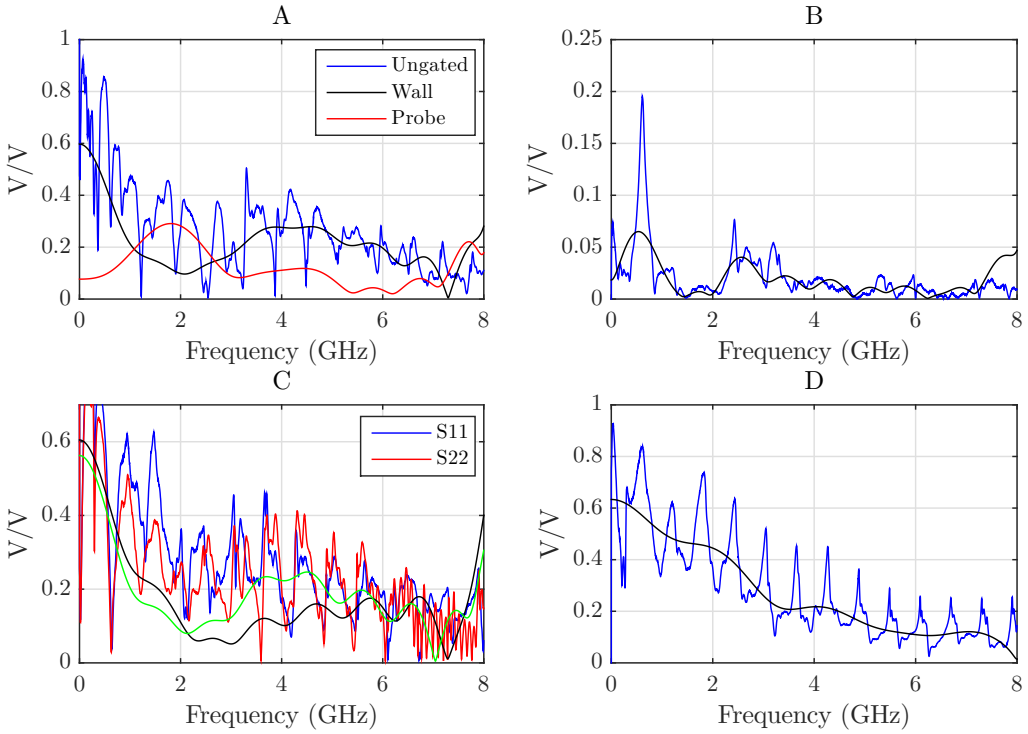

Figure A.4: FD signals for the enlarged conductor experiment. A: Fixture reflection coefficient, B: Probe response (S_{21}), C: Half-fixture reflection coefficients, D: Half-fixture through measurement (S_{21}).

A.3 Height comparison

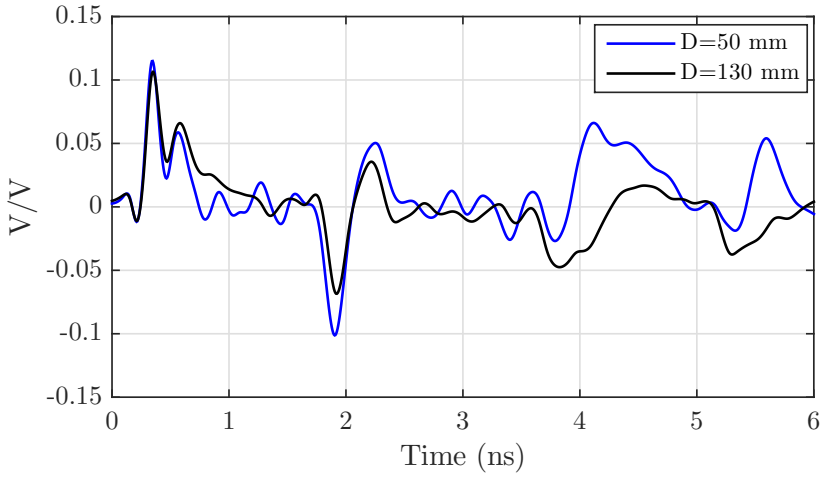

Figure A.5: Reflection coefficient of the fixture for different conductor heights. An increase in settling time is present if the connection between the connector pin and conductor matching profile is not regulated.

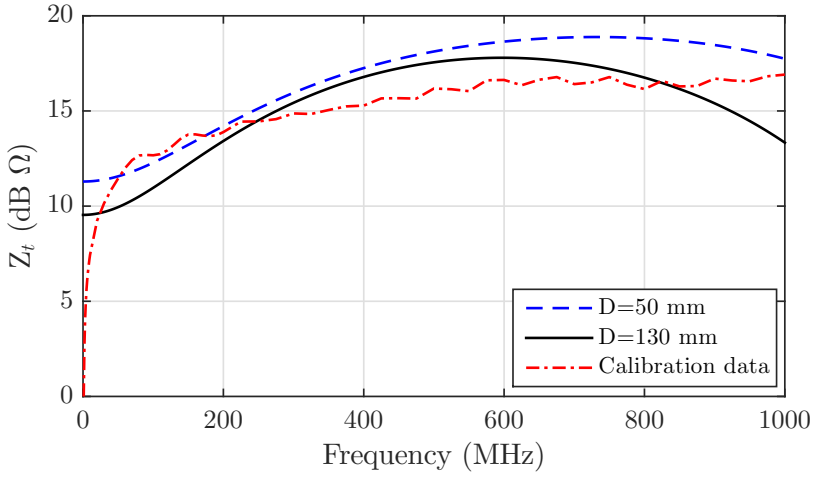

Figure A.6: Calibration of the ETS CP at different heights. The large RC will utilise a conductor at a height of 130 mm.

Appendix B

Matlab Code

B.1 Model

Model for large RC.

```
%Dimensions
R=0.125;
A=0.03;
a=R-A;
b=R+A;

rw=0.0015;
N=10;%# windings
%length of toroid + return winding
lw=toroidWLength(R,0.03,10,1);

eps0=8.854187817e-12;
muw=1.256629e-6;
mu0=4*pi*1e-7;
sigw=5.96e7;
%Frequency span in radians
w=(1e5)*(2*pi):(1e6)*(2*pi):(1000e6)*(2*pi);

Rm=50; %Zo of measurement eqiup.

Lt=mu0*N*N*0.5*(sqrt(b)-sqrt(a))^2;
L=Lt;
M=Lt/(N*lw);
F=0.2; %convergence factor
C=(2*pi*eps0/(log(2*R/rw)))*F*lw; %Winding to return winding cap.

Gams=sqrt(1i*w*muw*mu0*sigw);
Zskin=(lw*Gams/(2*pi*rw*sigw)).*(besseli(0,Gams*rw)./besseli(1,Gams*rw));

Zs=(Zskin+1i*w*L);        %eq4 equiv. Imp.
Gam= sqrt(Zs.*(1i*w*C)); %eq6 Prop. Constant
Zo= sqrt(Zs./(1i*w*C));  %eq7 Wave Impedance

%Theoretical RC Zt
Zt_theor=1i*w*M*Rm.*Zo.*sinh(Gam*lw);
Zt_theor=Zt_theor./(Zs.*(Zo.*sinh(Gam*lw)+Rm*cosh(Gam*lw)));%eq 20

```

```
%Theoretical RC Imp
Ln=1e-9;    %Inductance ass. with N-type conn
Cn=1.5e-12;%Capacitance ass. with N-type conn
Zr=1i*w*Ln+Zo.*tanh(lw*Gam)./(1+1i*w*Cn.*Zo.*tanh(lw*Gam));
```

Function for determining length of RC

```
%Numerically integrate along toroid path to determine length
%R= mean radius
%a=winding radius
%N=number of turns
function d=toroidWLength(R,a,N,Nopen)
cut=1-Nopen/N;
d=2*pi*(R*cut);
t=0:0.001:(2*pi*(cut));
x=(R+a*sin(N*t)).*cos(t);
z=(R+a*sin(N*t)).*sin(t);
y=a*cos(N*t);
plot3 (x, y, z, 'DisplayName', 'x, y, z'); figure(gcf)
for k=1:(length(x)-1)
    d=d+sqrt((x(k)-x(k+1))^2 +(y(k)-y(k+1))^2 +(z(k)-z(k+1))^2);
end
```

B.2 Time Domain de-embedding

Matlab code for:

S-parameter extraction

```
%Function for importing S1P or S2P data
%fileToRead1= filename eg. measurement.s1p
%firstline= data start,ZVB,FEKO,PNAx=5,7,10
%SL Combrink 16030826
function importS_P(fileToRead1,firstline)
%  Auto-generated by MATLAB on 01-Sep-2014 12:08:35
%rawData1 = importdata(fileToRead1);
rawData1=importdata(fileToRead1, ' ', firstline);
[unused,name] = fileparts(fileToRead1);
%modified next line to give generic filename
%newData1.(genvarname(name)) = rawData1%original
newData1.(genvarname('ImportedData')) = rawData1;%new
vars = fieldnames(newData1);
for i = 1:length(vars)
    assignin('base', vars{i}, newData1.(vars{i}));
end
```

FD-TD conversion

```
%FDTF.m
%Concept refined from inhouse internship report
%SL Combrink 1603086
clear all
%close all
% addpath ../Functions
%load EMCO_94111_1L_CalData;

%Load data straight from ZVB/FEKO/PNAX. name, start length 5/7/10
importS_P('60degLargeRaisedsmRCpgw.s2p',5);
s11=ImportedData.data(:,2).*exp(1i*pi*ImportedData.data(:,3)/180);
s21=ImportedData.data(:,4).*exp(1i*pi*ImportedData.data(:,5)/180);
f=ImportedData.data(:,1);

importS_P('60degLargeRaisedthrough.s2p',5);
s11B=ImportedData.data(:,2).*exp(1i*pi*ImportedData.data(:,3)/180);
s21B=ImportedData.data(:,4).*exp(1i*pi*ImportedData.data(:,5)/180);
s22B=ImportedData.data(:,8).*exp(1i*pi*ImportedData.data(:,9)/180);
clear ImportedData;

%Extrapolate DC- VNA/FEKO needs to give harmonically related points
f=[0 ;f];
s11=[1 ;s11];
s21=[0 ;s21];
s21B=[0 ;s21B];
s11B=[1 ;s11B];
s22B=[1 ;s22B];
N=length(s11);

%Apply filter to decrease Sinc ripple
beta=6;
Kai=kaiser(2*N,beta);
```

```
S11=s11.*Kai(N+1:end);
S21=s21.*Kai(N+1:end);
S21B=s21B.*Kai(N+1:end);
S11B=s11B.*Kai(N+1:end);
S22B=s22B.*Kai(N+1:end);

%Add Phase to see pulse around t=0
xxx=(0:N-1)';
phaseAngle=5;%in radians
phase=(pi/180)*(-phaseAngle)*xxx;%used in TimeAxis
S11=S11.*exp(1i*phase);
S21=S21.*exp(1i*phase);
S21B=S21B.*exp(1i*phase);
S11B=S11B.*exp(1i*phase);
S22B=S22B.*exp(1i*phase);

%zero padding if smoothing function is not used.
NxZeroes=1;
% S11=[S11;(zeros(1,NxZeroes*length(S11)+1))'];
% S21=[S21;(zeros(1,NxZeroes*length(S21)+1))'];
% S21B=[S21B;(zeros(1,NxZeroes*length(S21B)+1))'];
% S11B=[S11B;(zeros(1,NxZeroes*length(S11B)+1))'];
% Nzeroed=length(s11);

%Flip trace to get full spectrum
S11=[S11;flipud((S11(1:end-1)))];
S21=[S21;flipud((S21(1:end-1)))];
S21B=[S21B;flipud((S21B(1:end-1)))];
S11B=[S11B;flipud((S11B(1:end-1)))];
S22B=[S22B;flipud((S22B(1:end-1)))];

%Set up time scale
M=length(S11);
fs=M*f(2);
dt=1/fs;
t=(0:M)';
T=1/f(2);
tshift=phaseAngle*T/360;
t=t*dt-tshift;

fftAmp=2;%2 Since added flipped trace
x11=fftAmp*ifft(S11)/1;%
x21=fftAmp*ifft(S21)/1;%
x21B=fftAmp*ifft(S21B)/1;%
x11B=fftAmp*ifft(S11B)/1;%
x22B=fftAmp*ifft(S22B)/1;%

%gating process
gLen=round((1.05-(-0.2839))/(dt*1e9))+0;%general length of pulse
g21end=6;%6

%'Random' added values are fine tune values
gStart=round((-0.2839-t(1)*1e9)/(dt*1e9))+2;
gEnd=gStart+gLen+2;
gate11A=zeros(1,length(x11));
gate11A(gStart:gEnd)=1;%gate
x11gA=gate11A'.*x11;

gStart=round((1.625-t(1)*1e9)/(dt*1e9));
```

```
gEnd=gStart+gLen-4;
gate11Emco=zeros(1,length(x11));
gate11Emco(gStart:gEnd)=1;
x11gEmco=gate11Emco'.*x11;

gStart=round((1-t(1)*1e9)/(dt*1e9));
gEnd=gStart+gLen+g21end;%-3emco +2 RCpgw <- fine tune parameters
gate21=zeros(1,length(x21));
gate21(gStart:gEnd)=1;
x21gEmco=gate21'.*x21;

gStart=round((0.875-t(1)*1e9)/(dt*1e9))-1;
gEnd=gStart+gLen-5;
gate21B=zeros(1,length(x21B));
gate21B(gStart:gEnd)=1;
x21gB=gate21B'.*x21B;

Bgate=9;
gStart=round((+0.251-t(1)*1e9)/(dt*1e9))-3;
gEnd=gStart+gLen-Bgate;
gate11B=zeros(1,length(x11B));
gate11B(gStart:gEnd)=1;
x11gB=gate11B'.*x11B;

gStart=round((+0.251-t(1)*1e9)/(dt*1e9))-3;
gEnd=gStart+gLen-Bgate;
gate22B=zeros(1,length(x22B));
gate22B(gStart:gEnd)=1;
x22gB=gate22B'.*x22B;

xlimit=[-1 4];%*1e-9;

% fft and compensate for Kaiser filter and added phase
amp=1;

s11gA=fft(real(x11gA));
s11gA=amp*(s11gA(1:N)./(Kai(N+1:end))).*exp(-1i*phase);

s11gEmco=fft(real(x11gEmco));
s11gEmco=amp*(s11gEmco(1:N)./(Kai(N+1:end))).*exp(-1i*phase);

s21gEmco=fft(real(x21gEmco));
s21gEmco=amp*(s21gEmco(1:N)./(Kai(N+1:end))).*exp(-1i*phase);

s21gB=fft(real(x21gB));
s21gB=amp*(s21gB(1:N)./(Kai(N+1:end))).*exp(-1i*phase);

s11gB=fft(real(x11gB));
s11gB=amp*(s11gB(1:N)./(Kai(N+1:end))).*exp(-1i*phase);

s22gB=fft(real(x22gB));
s22gB=amp*(s22gB(1:N)./(Kai(N+1:end))).*exp(-1i*phase);

NN=1102;
A1=1+s11gB(1:NN);%Refelction for beginning half fixture
A2=1+s22gB(1:NN);%Refelction for end half fixture
B=s21gB(1:NN)./(-A1.*A2);%Transmission for half fixture
A=1+s11gA(1:NN); %Refelction for large fixture
C=s21gEmco(1:NN)./(A.*B); % Probe response
```

```
151 D=s11gEmco(1:NN).*B./(-A);% Probe effect on line
152
153 Ztf=50*s21./(1-s11);%stright frequency ZT
154 Zt=50*C./(1-D);      %gated ZT
155
156 run plotts%plot everything needed to fine tune gates
```

Kaiser filter [43]

```
1  % Copyright (C) 1995, 1996, 1997 Kurt Hornik
2  % <Kurt.Hornik@ci.tuwien.ac.at>
3  % Copyright (C) 2000 Paul Kienzle <pkienzle@users.sf.net>
4  %
5  % This program is free software; you can redistribute
6  % it and/or modify it under the terms of the GNU General
7  % Public License as published by the Free Software
8  % Foundation; either version 3 of the License, or (at your option)
9  % any later version.
10 % This program is distributed in the hope that it will be useful,
11 % but WITHOUT
12 % ANY WARRANTY; without even the implied warranty of MERCHANTABILITY or
13 % FITNESS FOR A PARTICULAR PURPOSE. See the GNU General Public License
14 % for more details.
15 % You should have received a copy of the GNU General Public License along
16 % with this program; if not, see <http://www.gnu.org/licenses/>.
17 % usage:  kaiser (L, beta)
18 % Returns the filter coefficients of the L-point Kaiser window with
19 % parameter beta.
20 % For the definition of the Kaiser window, see A. V. Oppenheim &
21 % R. W. Schafer, 'Discrete-Time Signal Processing'.
22 %
23 % The continuous version of width L centered about x=0 is:
24 %         besseli(0, beta * sqrt(1-(2*x/L).^2))
25 % k(x) =  ------------------------------------,  L/2 <= x <= L/2
26 %                 besseli(0, beta)
27 function w = kaiser (L, beta)
28 if nargin<2
29     beta = 0.5;
30 end
31 if (nargin < 1)
32     help(mfilename);
33 elseif ~(isscalar (L) && (L == round (L)) && (L > 0))
34     error ('kaiser:  L has to be a positive integer');
35 elseif ~(isscalar (beta) && (beta == real (beta)))
36     error ('kaiser:  beta has to be a real scalar');
37 end
38
39 if (L == 1)
40     w = 1;
41 else
42     m = L - 1;
43     k = (0 : m)';
44     k = 2 * beta / m * sqrt (k .* (m - k));
45     w = besseli (0, k) / besseli (0, beta);
46 end % if
47 end
```

Appendix C

Construction

C.1 Rogowski coils

The Rogowski coil is relatively easy to construct depending on the winding shape required. Shown in fig. C.1 are four RCs. The large RC (A) can be constructed with wire and a round cylinder of the required diameter. In trying to replicate fabrication of the large RC, it was found that a 50 mm PVC pipe can be used to wind RC. The most challenging part of fabrication was bending the wounded wire into the toroidal shape. Care should be taken with RCs using large diameter wire since the winded wire may act as a spring and can be dangerous if unwounded without care.

For RC B, softer, more malleable wire was used and formed over a 3D printed structure. The structure allows for enhanced rigidity and can be designed for a specific RC. Table C.1 lists the dimensions of the RCs shown in fig. C.1 and the dimensions are shown in fig.C.2.

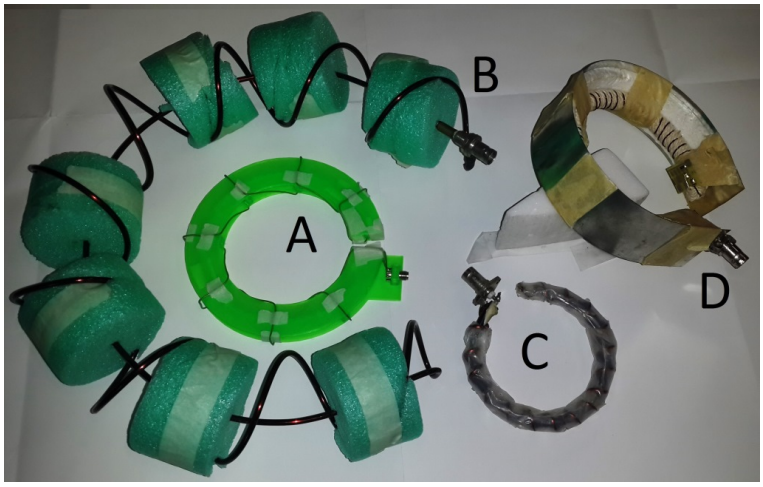

Figure C.1: A set of different Rogowski coils. A: a low profile RC, B: the large RC, C: a smaller RC, D: an RC with an electrostatic shield and terminating resistance.

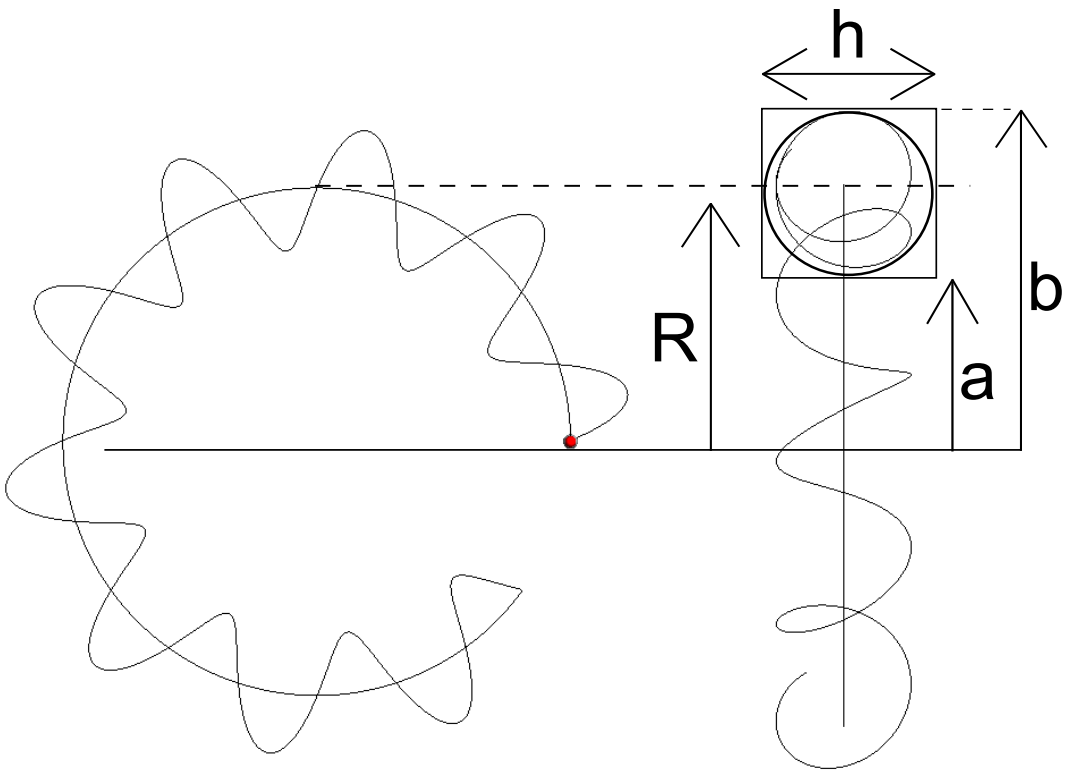

Figure C.2: Dimensions associated with Rogowski coils

Dimensions in mm						
RC	R	a	b	h	r_w	N
A	60	50	70	5	0.2	7
B	125	30	30	-	1.5	9
C	42.5	37	48	-	1	15
D	55	49.5	60.5	-	0.25	47

Table C.1: Dimensions for the RCs in fig. C.1. The dimensions are shown infig. C.2. The dimension r_w is the wire radius

C.2 Calibration fixtures

If the needed equipment is readily available, construction of the calibration fixture should not produce any difficulty. In its most basic form, the calibration fixture can be formed from a single piece of sheet metal, bent at two places, forming the required 'U' shape. Depending on the height of the transmission line wire, two holes will have to be drilled or punched to fit the appropriate connectors (eg. N-type or SMA). Listed in table C.2 are the dimensions for the fixtures shown in fig. 3.9 and 3.6. The fixture shown in fig. 3.6 has a variable wall and the dimensions for TD1 and TD2 was applied to it.

Dimensions in mm				
Fixture	Length	Width	D	d
A	-	-	117.5	14
B	60	200	60	2
C	250	200	50	2&30
D	200	400	200&240	2
TD1	500	300	50&130	2&30
TD2	1016	300	50&130	2&4

Table C.2: Dimensions for the fixtures in fig. 3.9. Dimensions D and d are shown in fig. 3.10. For the CISPR type fixture, D and d represents the inner wall diameter and conductor diameter, respectively.

Appendix D

Calibration certificates

D.1 ETS 94111-1L

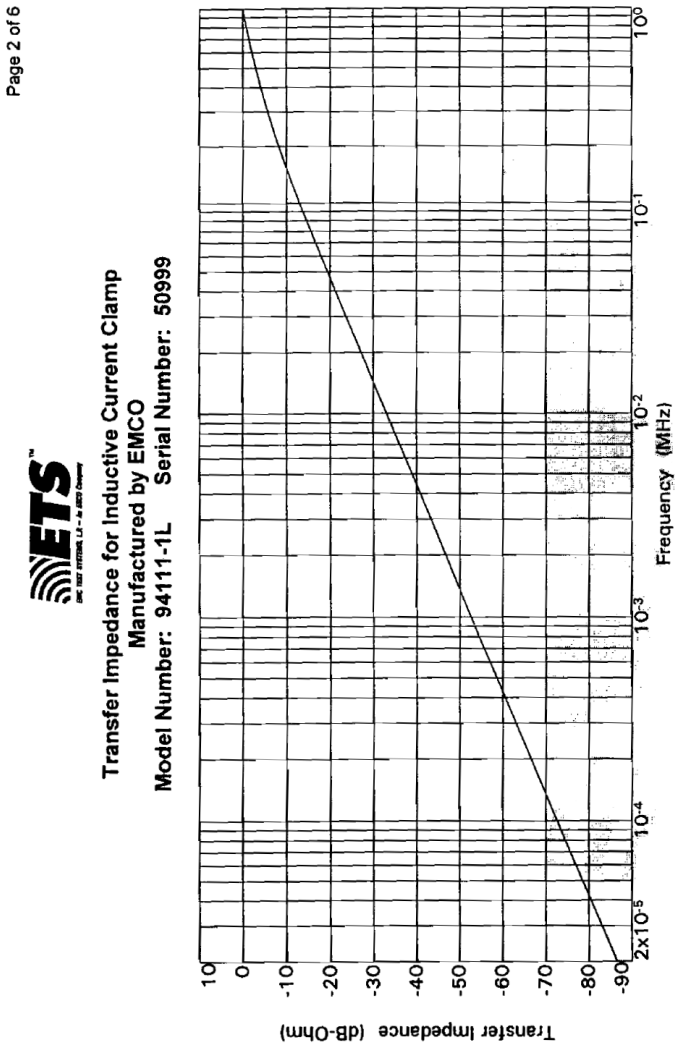

Figure D.1: Z_t calibration certificate of ETS probe (lower frequency range)

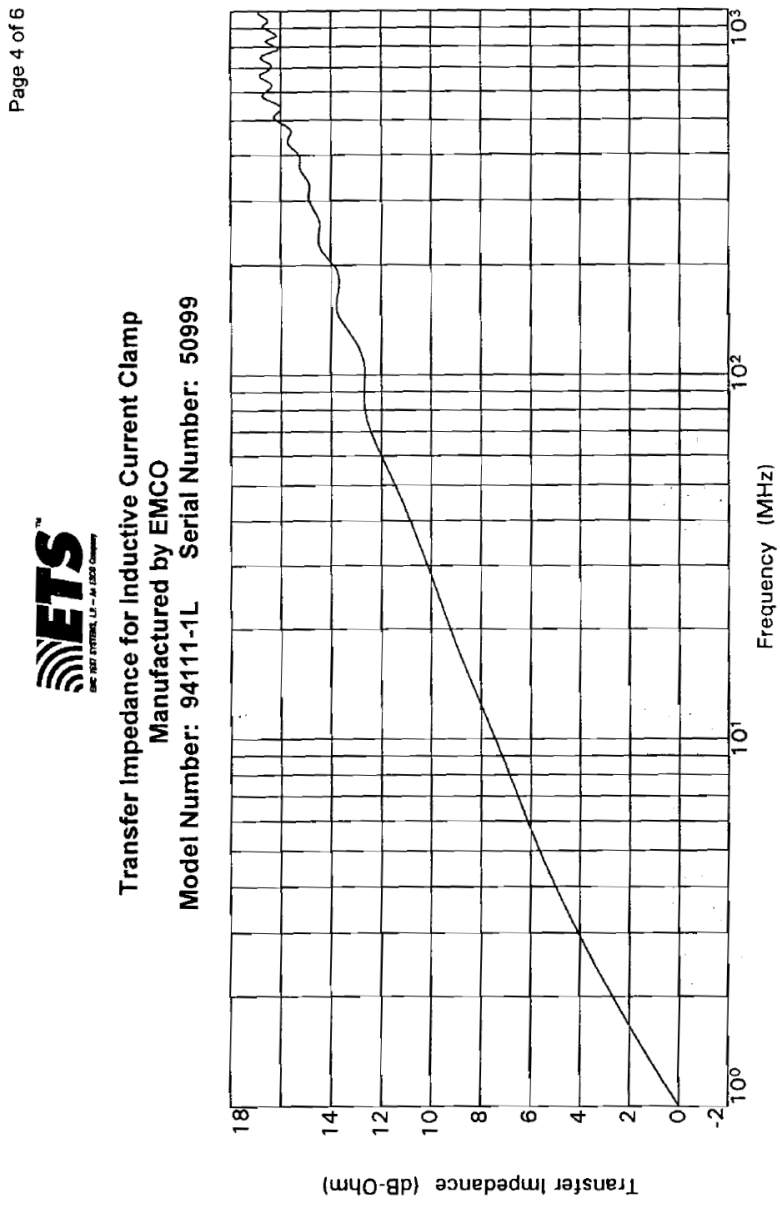

Figure D.2: Z_t calibration certificate of ETS probe (higher frequency range)

D.2 Fischer CC F-2000-12mm

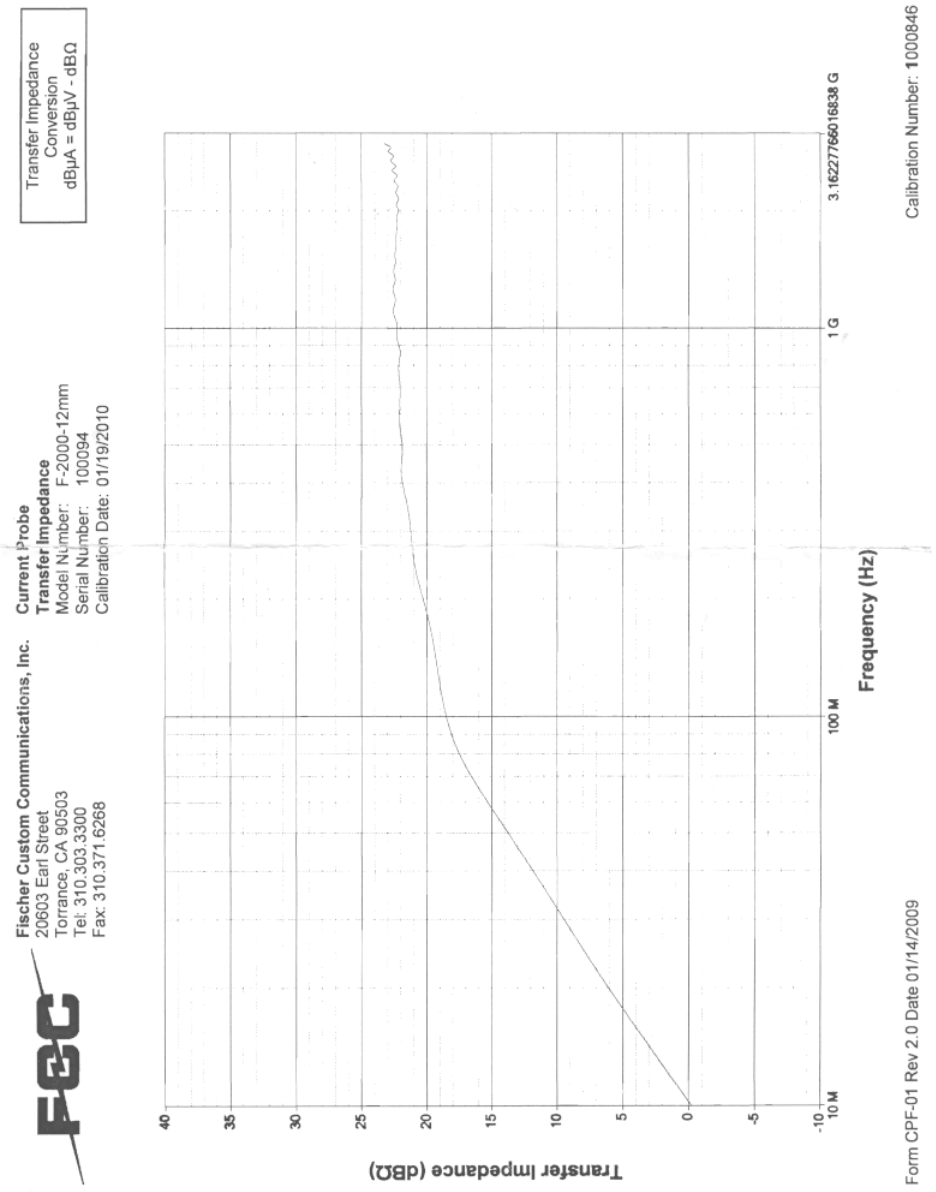

Figure D.3: Z_t calibration certificate of Fischer probe

Bibliography

[1] SKA. (2015) Square Kilometre Array. [Online]. Available: www.skatelescope.org/project/

[2] P. G. Wiid, "Lightning Protection and Radio Frequency Interference Mitigation for the Karoo Array Telescope," Ph.D Desertion, E.E. Dept., University of Stellenbosch, 2010.

[3] SABS, *Protection against lightning, Part 1: General principles.* South African National Standard, 2011, no. 62305-1:2011.

[4] FEKO. (2014) The FEKO website. [Online]. Available: www.feko.info/

[5] P. G. Wiid, H. C. Reader, and R. H. Geschke, "Radio Frequency Interference and Lightning Studies of a Square Kilometre Array Demonstrator Structure," *IEEE Transactions on Electromagnetic Compatibility*, vol. 53, no. 2, pp. 543–547, May 2011.

[6] ——, "Karoo Array Telescope: Lightning Protection Issues and RFI," in *2011 XXXth URSI General Assembly and Scientific Symposium*, August 2011, pp. 1–4.

[7] (2014) Square Kilometre Array SA public science/engineering site. [Online]. Available: public.ska.ac.za/

[8] D. Ruiz, C. Torralba, J. P. Marco, I. O. Calzada, V. Pomar, S. Polo, P. Llovera, C. Fuster, and F. Magraner, "A new concept in lightning parameters measurement," *11th International Conference on Electrostatics*, vol. 67, pp. 496–500, May 2009.

[9] A. M. Hussein, W. Janischewskyj, M. Milewski, V. Shostak, F. Rachidi, and J. S. Chang, "Comparison of current characteristics of lightning strokes measured at the cn tower and at other elevated objects," *IEEE International Symposium on Electromagnetic Compatibility*, vol. 2, pp. 495–500, August 2003.

[10] J. Yang, X. Qie, G. Zhang, and H. Wang, "Magnetic field measuring system and current retrieval in artificially triggering lightning experiment," *Radio Science*, vol. 43, April 2008.

[11] T. Tominaga, N. Kuwabara, J. Kato, A. Ramli, A. Halim., and H. Ahmed, "Characteristics of lightning surges induced in telecommunication center in tropical area," *IEEE Transactions on Electromagnetic Compatibility*, vol. 45, no. 1, pp. 82–91, February 2003.

[12] Y. Li, Y. Gua, Y. Long, C. Yao, Y. Mi, and J. Wu, "Novel lightning current sensor based on printed circuit board rogowski coil," in *2012 International Conference on High Voltage Engineering and Application*, September 2012.

[13] P. N. Murgatroyd and D. N. Woodland, "Geometrical Properties of Rogowski Sensors," in *IEEE Colloquium on Low Frequency Power Measurement and Analysis*, November 1994.

[14] G. Robles, M. Argüeso, J. Sanz, R. Giannetti, and B. Telinni, "Identification of parameters in a Rogowski Coil used for the measurement of partial discharges," in *IEEE Instrumentation and Measurement Technology Conference Proceedings*, May 2007, pp. 1–4.

[15] M. Argüeso, G. Robles, and J. Sanz, "Measurement of high frequency currents with a Rogowski Coil," *Rev. Sci. Instrum*, vol. 76, no. 6, 2005.

[16] W. F. Ray and C. R. Hewson, "High Performance Rogowski Current Transducers," in *Conference Record of the 2000 IEEE Industry Applications Conference*, vol. 5, October 2000, pp. 3083–3090.

[17] M. Shafiq, L. Kütt, M. Lehtonen, , T. Nieminen, and M. Hashmi, "Parameters Identification and Modeling of High-Frequency Current Transducer for Partial Discharge Measurements," *IEEE Sensors Journal*, vol. 13, no. 3, pp. 1081–1091, March 2013.

[18] *CISPR 16-1-2, Specification for radio disturbance and immunity measuring apparatus and methods*, 2nd ed.

[19] V. Dubickas and H. Edin, "High-Frequency Model of the Rogowski Coil With a Small Number of Turns," *IEEE Transactions On Instrumentation and Measurement*, vol. 56, no. 6, pp. 2284–2288, December 2007.

[20] W. F. Ray, C. R. Hewson, and J. M. Metcalfe, "High frequency effects in current measurement using Rogowski coils," in *2005 European Conference on Power Electronics and Applications*, 2005, p. 9.

[21] M. Rütschlin, "Aspects of Modelling and Metrology in EMC," Master's thesis, E.E. Dept., University of Stellenbosch, 1991.

[22] M. Rezaee and H. Heydari, "Mutual Inductances Comparison in Rogowski Coil with Circular and Rectangular Cross-Sections and Its Improvement," in *3rd IEEE Conference on Industrial Electronics and Applications*, June 2008, pp. 1507–1511.

[23] M. Shafiq, M. Lehtonen, L. Kütt, G. A. Hussain, and M. Hashmi, "Effect of Terminating Resistance on High Frequency Behaviour of Rogowski Coil for Transient Measurements," *Elektronika Ir Eletrotechnika*, vol. 19, no. 7, pp. 22–28, 2013.

[24] C. Hewson and W. F. Ray, "The effect of electrostatic screening of Rogowski coils designed for wide-bandwidth current measurement in power electronic applications," in *35th Annual IEEE Power Electronics Specialists Conference*, vol. MTT-27, no. 8, August 2004, pp. 717–721.

[25] D. W. Knight. (2013, July) The self-resonance and self-capacitance of solenoid coils. [Online]. Available: http://www.g3ynh.info/

[26] M. Marracci, B. Tellini, and C. Zappacosta, "Fem analysis of Rogowski coils coupled with bar conductors," *XIX IMEKO World Congress*, Sept 2009.

[27] T. Guillod, D. Gerber, J. Biela, and A. Meusing, "Design of a PCB Rogowski Coil based on the PEEC Method," in *2012 7th International Conference on Integrated Power Electronics Systems (CIPS),*, vol. 11, no. 1, March 2012, pp. 1–6.

[28] I. A. Metwally, "Design of Different Self-Integrating and Differentiating Rogowski Coils for Measuring Large-Magnitude Fast Impulse Currents," *IEEE Transactions on Instrumentation and Measurement*, vol. 62, no. 8, August 2013.

[29] L. Weibo and M. C. nad L. Jiming, "Some Considerations of Designing a High Performance Rogowski Coil for Pulsed Current Measurement," *Journal of Electrical and Electronics Engineering*, vol. 6, no. 1, pp. 7 – 12, 2006.

[30] M. Argüeso, G. Robles, and J. Sanz, "Implementation of Rogowski coil for the measurement of partial discharges," *Rev. Sci. Instrum.*, vol. 76, no. 6, pp. 065 107–1–065 107–7, May 2005.

[31] J. Ramboz, "Machinable Rogowski Coil, Design and Calibration," *IEEE Transactions On Instrumentation and Measurement*, vol. 45, no. 2, pp. 511–515, April 1995.

[32] Y. Liu, F. Lin, Q. Zhang, and H. Zhong, "Design and Construction of a Rogowski Coil for Measuring Wide Pulsed Current," *IEEE Sensors Journal*, vol. 11, no. 1, pp. 123–130, January 2011.

[33] Fischer Custom Communications, INC. [Online]. Available: www.fischercc.com/

[34] A. R. Ruddle, S. C. Pomeroy, and D. D. Ward, "Calibration of Current Transducers at High Frequencies," *IEEE Transactions on Electromagnetic Compatibly*, vol. 43, no. 1, pp. 100–104, February 2001.

[35] A. R. Ruddle, "Calibration of Current Measurement Transducers in Oversized Calibration Fixtures," *IEEE Transactions on Electromagnetic Compatibly*, vol. 47, no. 1, pp. 196–201, February 2005.

[36] G. Cerri, R. D. Leo, V. M. Primaiani, S. Pennesi, and P. Russo, "Wide-Band Characterization of Current Probes," *IEEE Transactions On Instrumentation and Measurement*, vol. 45, no. 5, pp. 616 – 625, November 2003.

[37] M. N. Iddagoda, N. V. Venkatarayalu, and Y. B. Gan, "Characterization, Calibration and Macromodeling of RF Current Probes," *APMC Microwave Conference 2009*, pp. 629–632, December 2009.

[38] L. Ferković, D. Ilić, and R. Malarić, "Mutual Inductance of a Precise Rogowski Coil in Dependence of the Position of Primary Conductor," *IEEE Transactions on Instrument and Measurement*, vol. 58, no. 1, pp. 122–128, January 2009.

[39] H. Reader, R. Geschke, J. Badenhorst, and E. Laubscher, "Issues in calibrating sensors for emi and suppression of unwanted modes," in *Saupec 2007 Conference*, 2007.

[40] B. Kruizinga, "Time domain current probe measurements," 2014, Unpublished Report.

[41] H. A. Wheeler, "Transmission-line properties of a round wire in a polygon shield," *IEEE Transactions on Microwave Theory and Techniques*, vol. MTT-27, no. 8, pp. 717–721, August 1979.

[42] P. G. Wiid, "The answer is in fact 41," in *2015 IEEE-APS Topical Conference on Antennas and Propagation in Wireless Communications (APWC),* , Torino,Italy, Sept 2015, pp. 1060 – 1063.

[43] K. Hornik. (1997) Matlab Kaiser Filter. [Online]. Available: https://searchcode.com/codesearch/view/9511636/